

L.C. Drost

THE SUBMERGED FLOATING TUNNEL

An experimental study on the hydrodynamic forces
and kinematics of a submerged rectangular cylinder in
a wave-current environment

 TU Delft

 Royal
HaskoningDHV
Enhancing Society Together

THE SUBMERGED FLOATING TUNNEL

An experimental study on the hydrodynamics and kinematics of a submerged rectangular cylinder in a wave-current environment

By

L.C. Drost

in partial fulfilment of the requirements for the degree of

Master of Science
in Civil Engineering

at the Delft University of Technology,
to be defended publicly on Thursday January 17, 2019 at 10:30 AM.

Supervisor:

Prof. dr. ir. W. Uijtewaal

Thesis committee:

Dr. ir. D.J. Peters,

Ir. K. Reinders,

Dr. ir. X. Chen,

TU Delft

TU Delft

TEC/Royal Haskoning DHV

This thesis is confidential and cannot be made public until January, 2019.
In electronic version of this thesis is available at <http://repository.tudelft.nl/>.

Acknowledgements

As my graduation date draws near, I have started to reflect on my time in Delft as a student and in particular how numerous developments in these years has brought me to this point. Reflecting on the ultimate challenge of my time as a student, writing my thesis, have made me realize that it would have been much harder without the help and support of various people. Therefore, I would like to take some time and words to give thanks to a couple of them.

First of all, I would like to thank my committee members. Every member has played its own significant role in supporting me through the thesis work. I would like to thank Prof. Uijtewaal, for leading the progress meetings. Because of your effort the meetings were a comfortable environment in which effectively the progress of my work was stressed and yet I was constructively encouraged to go deeper into other parts. This balanced method was right for me. Where at the start of my thesis I did not feel too confident about conducting a full academic research, I now feel I am worthy of receiving the engineer title. Next, I would like to thank Dirk Jan for introducing me to Royal Haskoning DHV and giving me the opportunity to see some part of the larger project scope with the Chinese partner. In addition, the separate feedback moments in which you helped me to make in depth technical decisions were very helpful. Also, I would like to give my thanks to Kristina. You were always available to help me when I needed someone to zoom out a little bit and redirect my focus on the broader scope of the thesis. It made me feel relieved and encouraged to continue my work. Last I would like to thank Xuexue. I think without your support of both encouragement and pushing me to limits, my work would have not been of the quantity and level of quality, as it is right now. I like how you have treated and approached me. It created an environment in which our contact to help one another was very efficient and pleasant. Thank you very much.

Second, I want to thank the support I have received during the time in the lab. Starting with the lab technicians, Sander, Rob, Arno, Pieter, Frank and Jaap, who helped me get to know the wave flume in no time and were always available to help me with the endless practical challenges I faced in doing lab work. Besides the lab technicians, I would like to thank the students, Hidde, Rosanne, Tom and Daan, who helped performing part of my experiments. This help offered me time to take a step back and evaluate the next steps in the process that laid ahead.

Last, I would like to thank my friends and family. Whether it was through mental support, giving me distractions or bringing me a meal in the library, I am very grateful for all types of support I received. Especially, I would like to thank Daan for being with me in the library almost every single day in the last 1.5 months of my thesis, cooking for me numerous times and guarding my phone to prevent unwanted distraction. Your presence and support gave me new insight on disciplined work and helped me through the tough times.

*L.C. Drost,
Delft, January 2019,*

Abstract

This study presents the results of small scale flume experiments on a submerged rectangular cylinder subjected to a current, regular wave and combined wave-current environment. The objective of the study is to gain more knowledge about the hydrodynamics around and the kinematics of a submerged structure, to give a contribute to the research field of the submerged floating tunnel.

For this study a rectangular cylinder with an aspect ratio (breadth-depth) of 2.5 is used. Two relative submergence depths (flume depth/model submergence) of 2.75 and 1.63 are tested. For all tests a still water depth of 0.7 m is applied. Waves resulting in very low KC numbers of <1 for regular waves and $KC \left[1 + \frac{u_c}{u_m}\right] < 2$ for combined waves-current are generated. To create a combined wave-current environment, a current is created in the flume, to which waves are added by the wave generator. The water velocity is measured in front of the model. To approximate the water velocity at the model, a time/phase shift is added to the velocity signal. Linear wave theory is applied to approximate the amplitudes of the orbital velocities at the depth of the model.

For the first part of the study, on the hydrodynamic forces, the cylinder is rigidly fixed in the flume. Due to the inertia dominance for low KC numbers, the relationship between the wave parameters and the hydrodynamic forces is well described by the relationship between the wave parameters and the water particle accelerations. The vertical hydrodynamic forces are found to be larger than the horizontal hydrodynamic forces. The force coefficients from this study are compared to coefficient found in previous studies. The drag coefficients for the only current tests agree well with the results from (Courchesne & Laneville, 1979), (Bearman & Trueman, 1972), (Nakaguchi, 1968) and (Venugopal, 2006). For the regular wave and combined wave-current conditions comparable results are found to those by Venugopal for a rectangular cylinder towed through a wave field (Venugopal, 2008). The drag coefficients in the present study show a similar trend in magnitude as in the study by Venugopal. However, the magnitudes have an opposite sign due to the velocity phase shift method applied in the present study. Nevertheless, the effect of this difference on the total force prediction is insignificant, because of inertia dominance. In general, the Morison equation predicts the measured horizontal force well for regular waves. Adding a current component to the waves results in a larger error between the computed Morison forces and the measured force. However, an increase in the magnitude of the added velocity does not lead to a significant increase of this error.

The second part of the study focuses on the same cylinder, only not fixed but held in place by 4 tethers. For these tests a buoyancy to weight ratio of 1.5 is applied. The used tested angles between the tethers and the flume bottom are 30° and 70° . The water depth, the wave types and model submergence depths are remained equal to the first part of the study. By comparing the kinematics found in three different configurations, a 30° tether angle combined with the largest submergence depth of $d_s=0.35$ m are found to gives the smallest displacements and accelerations. To reduce the kinematics more, it is recommended to add vertical tethers to limit the vertical movement. In general, dynamic features are seen in the tethered model, influencing the magnitude of the kinematics. To predict the magnitude of the tether forces it is recommended to integrated these features in a structural dynamic model.

Contents

Acknowledgements	1
Abstract	2
Contents	3
List of Figures	5
List of Tables	8
List of Symbols	9
1 Introduction	10
1.1 Research Context.....	10
1.2 Problem Statement.....	11
1.3 Research Objectives and Questions.....	11
1.4 Report Structure.....	11
2 Literature Review	12
2.1 Theoretical Background.....	12
2.1.1 Flow Around a Submerged Structure in Steady Current	12
2.1.2 Flow Around a Submerged Structure in Waves.....	15
2.1.3 Flow Around a Structure in a Wave-Current Condition	19
2.2 Physical Modelling Practice	20
3 Methodology	21
3.1 Experiment Set-up	21
3.1.1 Flume Characteristics.....	22
3.1.2 Model Design and Prototype Reference	23
3.1.3 Model Set-up	24
3.2 Data Scope.....	26
3.3 Data Acquisition.....	28
3.3.1 Fixed Model	28
3.3.2 Tether model.....	28
3.4 Processing Methodology	30
3.4.1 General Processing Procedure	30
3.4.2 Velocity Signal Computations	32
3.4.3 Computation of the Morison coefficients.....	36
3.4.4 Force Prediction Procedure.....	38
4 Results and Analysis	39
4.1 The Relationship Between Environmental Conditions and Hydrodynamic Forces	40
4.1.1 Experiment Observations.....	40
4.1.2 Wave-Current Effects	43
4.1.2 The Relationships	50

4.1.3.	The Answer to Research Question 1a.....	55
4.2.	Force Prediction by Morison.....	56
4.2.1.	Force coefficients.....	56
4.2.2.	Force prediction by the Morison Force.....	63
4.2.3.	The Answer to Research Question 1b.....	68
4.3.	The Dynamic Response to Environmental Conditions.....	69
4.3.1.	Experiment Observations.....	69
4.3.2.	Response to a Regular Wave Conditions.....	76
4.3.3.	Force prediction by Morison.....	82
4.3.4.	The Answer to Research Question 2.....	85
5	Discussion.....	86
5.	Conclusions and Recommendations.....	91
	Bibliography.....	95
	Appendices.....	96
A.	List of All Experiments Done.....	96
B.	Model Weight Distributions.....	97
C.	Prediction Coefficients for the Morison Equation.....	1
D.	Dynamic parameters.....	4
E.	Fixed Model Force Signals.....	7
F.	Tether Model Force Signals.....	9
G.	Frequency Bands.....	11
H.	Results from fixed model tests.....	15
I.	Results Tether Model in Regular Waves.....	17

List of Figures

FIGURE 1: ALTERNATIVES FOR CROSSING A WATERWAY (A), THE APPLICATION OF A FLOATING BRIDGE OVER THE DONAU (B)	10
FIGURE 2: THE TWO MAIN SUBMERGED FLOATING TUNNEL DESIGNS: THE PONTOON DESIGN (A) AND THE TETHER DESIGN (B).....	10
FIGURE 3: DIFFERENT STREAMLINE PATTERNS OF A FLOWING FLUID AROUND A CYLINDRICAL OBJECT.....	12
FIGURE 4: FLOW REGIONS (A) AND DETAILED SEPARATION OF BOUNDARY LAYER (B), (FREDSØE & SUMER, 2006).....	13
FIGURE 5: A) AND B): EXAMPLES OF FLOW AROUND A BLUFF BODY (BREUER, 2000). C) SCHEMATIZATION OF SEPARATION AND REATTACHMENT AROUND A BLUFF BODY (MICHELIS, 2017)	13
FIGURE 6: THE PRESSURE AND FRICTIONS COMPONENTS CONTRIBUTING TO THE FORCE EXERTED BY A FLOWING FLUID ON A SUBMERGED BODY. (FREDSØE & SUMER, 2006).....	14
FIGURE 7: EXAMPLE PRESSURE DISTRIBUTION AND FORCES ON A CYLINDER IN A STEADY CURRENT AT DIFFERENT TIMES (FREDSØE & SUMER, 2006)	14
FIGURE 8: EXAMPLE OF FLUCTUATING LIFT AND DRAG COEFFICIENTS (FREDSØE & SUMER, 2006)	14
FIGURE 9: WATER PARTICLES IN ORBITAL MOTION UNDER A PROPAGATING WAVE IN DEEP WATER (HOLTHUIJSEN, 2007) (LEFT). VALIDITY REGIONS OF WAVE THEORIES (MEHAUTE, 1976)	15
FIGURE 10: A SCHEMATISATION OF A UNDISTURBED PRESSURE FLOW FIELD, AND A VIRTUAL CYLINDER (OE4620, NOVEMBER 2005).	17
FIGURE 11: EXAMPLE SIGNAL OF VELOCITY RELATED DRAG FORCES AND ACCELERATION RELATED INERTIA FORCES, COMBINED TO THE TOTAL FORCE. (FREDSØE & SUMER, 2006)	18
FIGURE 12: SIGNALS OF DIFFERENT VARIABLES FOR VARYING WAVE-CURRENT CONDITIONS (FREDSØE & SUMER, 2006)	19
FIGURE 13: SCHEMATISATION OF FIXED MODEL, MODEL NO.1 (A), AND TETHER MODEL, MODEL NO. 2 (B), SIDE PLAN.....	21
FIGURE 14: PICTURES OF THE MODEL NO.1 (LEFT) AND MODEL NO.2. (RIGHT) IN THE FLUME. THE RED DASHED LINED BOXES ENCLOSE THE TETHER LINES.	21
FIGURE 15: SIDE PLAN OF FLUME SET-UP (N.T.S.) FOR WAVE EXPERIMENTS AND CURRENT FLOW EXPERIMENTS.	22
FIGURE 16: A SCHEMATISATION OF THE GENERAL DESIGN FOR MODEL NO. 1 AND VARIABLE SUBMERGENCE DEPTH, D_s , WITH THE CONNECTING STRIP.....	24
FIGURE 17: THE DIFFERENT TETHER ANGLE-DEPTH CONFIGURATIONS. THE DASHED LINE (- - -) PORTRAYS THE $\alpha=30^\circ$, THE SOLID LINE (-) THE $\alpha=70^\circ$	25
FIGURE 18: POSITION OF INSTRUMENTS USED FOR THE FIXED MODEL DESIGNS (N.T.S.).....	28
FIGURE 19: TOP VIEW AND PLAN VIEW OF THE INSTRUMENT DISTRIBUTION IN THE FLUME (N.T.S.) AND A DETAIL OF A PULLEY/WHEEL	29
FIGURE 20: SIDE VIEW OF THE TETHER MODEL WITH THE BLUE, RED AND GREEN TRACKERS ON DRAWN ON IT.	29
FIGURE 21: SCHEMATIZATION OF CALIBRATING AND PROCESSING INSTRUMENT RECORDS	30
FIGURE 22: SCHEMATIZATION OF THE PROCESSING OF VIDEO RECORDS	30
FIGURE 23: SCHEMATIZATION OF PARAMETER DEFINITIONS, USED IN RECORD PROCESSING.....	31
FIGURE 24: THE LOCATION OF THE VELOCITY MEASURED BY THE EMS AND THE LOCATION OF THE VELOCITY OF INTEREST AT THE CENTRE OF THE MODEL.	32
FIGURE 25: VELOCITY DEPTH PROFILES OF DIFFERENT INPUT CURRENT VELOCITIES. AND A SCHEMATIZATION OF THE HALF TUNNELS HEIGHTS OF 0.175 M AND 0.35 M TUNNEL SUBMERGENCE DEPTH (BLUE) AND THE EMS DEPTH DURING MOST OF THE EXPERIMENTS (RED).	32
FIGURE 26: DEPTH AND TIME SHIFT APPLIED TO A WATER VELOCITY RECORD.....	33
5. FIGURE 27: EXAMPLE OF A VELOCITY TIME SHIFT. AT T_1 THE RED WAVE ARRIVES AT THE EMS, AT T_2 THE WAVE ARRIVES AT THE MODEL CENTRE OF MASS	34
FIGURE 28: A SCHEMATISATION OF THE FORCE PREDICTION FOR THE FIXED MODEL AND TETHER MODEL.....	38
FIGURE 29: THE WATER SURFACE ELEVATION SIGNALS FROM WAVE GAUGE 4 FOR 3 DIFFERENT TEST: A LONG WAVE, A SHORT WAVE AND A SHORT WAVE COMBINED WITH A LARGE CURRENT COMPONENT.	40
FIGURE 30: THE WATER SURFACE ELEVATION (TOP), HORIZONTAL VELOCITY (MIDDLE) AND HORIZONTAL FORCE (BOTTOM) SIGNALS FOR A SHORT WAVE WITH CURRENT (FRC143C).....	41
FIGURE 31: END OF FLUME RESONANCE IN THE SIGNAL OF THE HORIZONTAL FORCE FOR A REGULAR WAVE (FR14C)	42
FIGURE 32: CLOSE UP HORIZONTAL FORCE SIGNALS FOR A SHORT (FR14C) AND LONG WAVE (FR42C)	42
FIGURE 33: THE NON-ADJUSTED EMS HORIZONTAL PARTICLE VELOCITY SIGNALS AND THE HORIZONTAL FORCE SIGNALS FOR THREE CONDITIONS: CURRENT ($U_c=0.3$ M/S, $H=0$ M, $T=0$ s), REGULAR WAVES ($U_c=0$ M/S, $H_{INPUT}=0.16$ M, $T_{INPUT}=0.92$ s), AND COMBINED WAVE-CURRENT ($U_c=0.3$ M/S, $H_{INPUT}=0.16$ M, $T_{INPUT}=0.92$ s).	43

FIGURE 34: THE INFLUENCE OF A CO-EXISTING CURRENT ON THE WAVE PARAMETERS WAVE HEIGHT (LEFT) AND WAVE PERIOD (RIGHT)	44
FIGURE 35: CWT AND FILTERED WAVE SIGNALS. SHORT WAVE FR14C FILTERED FOR 0.7-1.28 Hz AND LONG WAVE FR42C FOR 0.45-0.7 Hz. BLUE DASHED LINE INDICATES THE INPUT WAVE AMPLITUDE ($H_{INPUT}/2$)	45
FIGURE 36: CWT AND FILTERED WAVE SIGNALS. SHORT WAVE FR14C FILTERED FOR 0.7-1.28 Hz. BLUE DASHED LINE INDICATES THE INPUT WAVE AMPLITUDE ($H_{INPUT}/2$)	46
FIGURE 37: A FILTERED WATER SURFACE ELEVATION SIGNAL FOR A LONG WAVE COMBINED WITH CURRENT, FRC423C.	47
FIGURE 38: FOR 0.2 M DEPTH THE COMPUTED AND MEASURED TOTAL WATER PARTICLE VELOCITIES U_x AND U_z AND THE WAVE COMPONENT OF THE HORIZONTAL WATER PARTICLE VELOCITY $U_{WAVE,X}$. RED DASHES LINES: ERROR BANDS.	48
FIGURE 39: THE MEAN HORIZONTAL HYDRODYNAMIC FORCE FOR DIFFERENT CURRENT VELOCITIES	50
FIGURE 40: FOR BOTH FORCE DIRECTIONS: THE RELATIONSHIP BETWEEN THE HYDRODYNAMIC FORCE AND THE WAVE PERIOD (LEFT COLUMN), AND THE HYDRODYNAMIC FORCE AND THE WAVE PERIOD (RIGHT COLUMN).	51
FIGURE 41: EXAMPLE OF AN ESTIMATION OF THE WATER PARTICLE ACCELERATIONS FOR A VARYING WAVE HEIGHT FOR $T \approx 0.92$ s (LEFT COLUMN) AND WAVE PERIOD (RIGHT COLUMN). FOR $H \approx 0.08$ M AND $D_s \approx 0.35$ M. ORANGE ARE THE USED ACCELERATIONS, GREY DASHED LINE ARE DEEP WATER ACCELERATION TRENDS	52
FIGURE 42: THE RELATIONSHIP BETWEEN THE WAVE HEIGHT (FOR $T \approx 0.92$ s) AND THE HORIZONTAL HYDRODYNAMIC FORCE AND THE WAVE PERIOD (FOR $H \approx 0.08$ M), BOTH WITH $D_s = 0.35$ M	53
FIGURE 43: THE RELATIONSHIP BETWEEN THE WAVE HEIGHT (FOR $T \approx 0.92$ s) AND THE VERTICAL HYDRODYNAMIC FORCE AND THE WAVE PERIOD (FOR $H \approx 0.08$ M), BOTH WITH $D_s = 0.35$ M	54
FIGURE 44: THE DRAG COEFFICIENTS FOUND IN THE PRESENT AND PREVIOUS STUDIES FOR DIFFERENT ASPECT RATIOS	56
FIGURE 45: THE PRESENT STUDY HORIZONTAL INERTIA COEFFICIENTS (ASPECT RATIO 0.4) COMPARED TO THE COEFFICIENTS FOUND BY VENUGOPAL ET AL. (ASPECT RATIO 0.5). FOR DIFFERENT FLUME DEPTH/SUBMERGENCE DEPTH RATIOS (D/H)	57
FIGURE 46: THE PRESENT STUDY VERTICAL INERTIA COEFFICIENTS (ASPECT RATIO 2.5) COMPARED TO THE COEFFICIENTS FOUND BY VENUGOPAL ET AL. (ASPECT RATIO 2). FOR DIFFERENT FLUME DEPTH/SUBMERGENCE DEPTH RATIOS (D/H)	58
FIGURE 47: THE HORIZONTAL DRAG COEFFICIENTS FOUND IN THE PRESENT STUDY	59
FIGURE 48: THE HORIZONTAL DRAG COEFFICIENTS FOUND BY VENUGOPAL (2006) AND ARAI (1993)	59
FIGURE 49: THE VERTICAL DRAG COEFFICIENTS FOUND IN THE PRESENT STUDY	60
FIGURE 50: THE VERTICAL DRAG COEFFICIENTS FOUND BY VENUGOPAL (VENUGOPAL, 2006) AND ARAI (ARAI, 1993)	60
FIGURE 51; THE HORIZONTAL AND VERTICAL INERTIA COEFFICIENTS FOR THE SITUATION OF COMBINED WAVE AND CURRENT. THE RESULTS OF THE PRESENT STUDY ($D_s = 0.35$ M) WITH ASPECT RATIO 0.4 (D/B) AND THE RESULTS BY VENUGOPAL (2008) WITH A LARGER ASPECT RATIO = 0.5	61
FIGURE 52: HORIZONTAL AND VERTICAL DRAG COEFFICIENT FROM PRESENT STUDY COMPARED TO THE RESULTS OF VENUGOPAL STUDY	62
FIGURE 53: THE HORIZONTAL (LEFT) AND VERTICAL (RIGHT) DRAG COEFFICIENT FOR THE TWO LARGEST ADDED CURRENT CONDITIONS	62
FIGURE 54: EXAMPLE OF THE TREND LINE USED FOR DETERMINATION OF THE MORISON PREDICTION COEFFICIENTS FOR REGULAR WAVES	63
FIGURE 55: THE MEAN MEASURED HORIZONTAL AND VERTICAL HYDRODYNAMIC PEAK FORCES PLOTTED WITH THE PREDICTED HORIZONTAL AND VERTICAL HYDRODYNAMIC PEAK FORCES	64
FIGURE 56: THE HORIZONTAL MEASURED FORCE SIGNAL PLOTTED WITH THE TOTAL MORISON FORCE (TOP PANEL), THE INERTIA FORCE COMPONENT (MIDDLE PANEL) AND THE DRAG FORCE COMPONENT (BOTTOM PANEL). FOR TWO ENVIRONMENTAL CONDITIONS REGULAR WAVE AND COMBINED WAVE AND CURRENT (FR14)	66
FIGURE 57: THE MEASURED FORCE (BLACK) WITH A MORISON FORCE PREDICTION FOR THREE DIFFERENT VALUES OF C_d . FOR A REGULAR WAVE	66
FIGURE 58: THE VERTICAL MEASURED FORCE SIGNAL PLOTTED WITH THE TOTAL MORISON FORCE (TOP PANEL), THE INERTIA FORCE COMPONENT (MIDDLE PANEL) AND THE DRAG FORCE COMPONENT (BOTTOM PANEL). FOR TWO ENVIRONMENTAL CONDITIONS REGULAR WAVE AND COMBINED WAVE AND CURRENT	67
FIGURE 59: SNAP SHOTS FROM A SHORT WAVE (R14) AND A LONG WAVE (R42) RUNNING OVER THE MODEL. $D_s = 0.175$ M. $A = 30^\circ$	69
FIGURE 60: SNAP SHOTS FROM A SHORT WAVE (R14) AND A LONG WAVE (R42) RUNNING OVER THE MODEL. $D_s = 0.35$ M, $A = 70^\circ$	70
FIGURE 61: THE VERTICAL AND HORIZONTAL DISPLACEMENTS OF THE RED MARKER FOR A SHORT (R14) AND LONG WAVE (R42) FOR $D_s = 0.35$ M, $A = 70^\circ$	71
FIGURE 62: EXAMPLE OF A TOTAL TETHER FORCE SIGNALS. FOR THE CONDITION OF A SUBMERGENCE DEPTH OF 0.35 M AND A TETHER ANGLE OF 30° . (R14C_30)	72
FIGURE 63: EXAMPLE OF A TOTAL TETHER FORCE SIGNALS. FOR THE CONDITION OF A SUBMERGENCE DEPTH OF 0.35 M AND A TETHER ANGLE OF 70° (R14C_70)	73

FIGURE 64: EXAMPLE OF A TOTAL TETHER FORCE SIGNALS. FOR THE CONDITION OF A SUBMERGENCE DEPTH OF 0.175 M AND A TETHER ANGLE OF 30° (R14B_30), WHERE SLACK OCCURS.	73
FIGURE 65: SCHEMATISATION OF THE TWO ACCELERATION MEASURING METHODS. (I) THE ACCELEROMETERS SIGNAL, (II) THE DERIVATIVE OF THE VIDEO RECORD OF THE DISPLACEMENT OF THE RED MARKER.	75
FIGURE 66: THE VERTICAL ACCELERATION SIGNAL FOR THE SAME WAVE (R12) FROM BOTH METHODS: FROM THE ACCELEROMETER (METHOD I), AND DERIVED FROM THE DISPLACEMENT SIGNAL (METHOD II).	75
FIGURE 67: THE THREE MODEL CONFIGURATIONS DISCUSSED IN THIS PARAGRAPH. THE SUBMERGENCE DEPTHS AND TETHER ANGLES ARE VARIED FOR THESE CONFIGURATIONS.	76
FIGURE 68: PICTURE OF MARKERS ON THE MODEL.	76
FIGURE 69: THE WAVE PARAMETERS, H AND T, AND THE VERTICAL (X) AND HORIZONTAL (•) DISPLACEMENTS OF THE MODEL FOR THE THREE MODEL CONFIGURATIONS WITH VARYING SUBMERGENCE DEPTH (0.175 M AND 0.35 M) AND TETHER ANGLE (70° AND 30°).....	77
FIGURE 70: CWT-GRAPHS OF THE HORIZONTAL DISPLACEMENT (LEFT) AND VERTICAL DISPLACEMENT (RIGHT) FOR THE SAME WAVES (R32 AND R42) FOR CONFIGURATION $\alpha=30^\circ$ AND DS=0.175 M. ($F_{WAVE}\approx 0.71$ Hz & $F_{WAVE}\approx 0.54$ Hz)	78
FIGURE 71: THE WAVE HEIGHT AND THE VERTICAL (CROSSES) AND HORIZONTAL (DOTS) ACCELERATIONS OF THE MODEL FOR THE THREE MODEL CONFIGURATIONS WITH VARYING SUBMERGENCE DEPTH (0.175 M AND 0.35 M) AND TETHER ANGLE (70° AND 30°). 79	79
FIGURE 72: THE FLUCTUATING TETHER FORCES FOR INCREASING WAVE PERIOD FOR DIFFERENT MODEL CONFIGURATIONS (T=0.92). LEFT) TETHER ANGLE $\alpha=30^\circ$ AND DS=0.175 M, MIDDLE) $\alpha=30^\circ$ AND DS=0.35 M RIGHT) $\alpha=70^\circ$ AND DS=0.35 M.....	80
FIGURE 73: EXAMPLE OF A TETHER FORCE SIGNAL AND DEFINITIONS OF THE VARIABLES. FROM (R14C_70)	81
FIGURE 74: THE HORIZONTAL NET RESULTANT TETHER FORCE (A, LEFT) AND THE VERTICAL NET RESULTANT TETHER FORCE (B, RIGHT), PLOTTED WITH THE PREDICTED HORIZONTAL AND VERTICAL MORISON FORCE.	82
FIGURE 75: BLUE IS MEASURED TETHER FORCE RESULTANT, RED THE PREDICTION BY THE MORISON FORCE. LEFT (R22C_70 Z), RIGHT (R22C_30 X).....	84
FIGURE 76: THE HORIZONTAL VELOCITY AND WAVE GAUGE SIGNAL OF A REGULAR WAVE (FR12C)	86
FIGURE 77: THE HORIZONTAL VELOCITY AND WAVE GAUGE SIGNAL OF A COMBINED WAVE-CURRENT (FRC123C)	87
FIGURE 78: THE INFLUENCE OF THE VELOCITY TIME SHIFT ON THE MORISON FORCE COEFFICIENTS. THE USED COEFFICIENTS AS RED DOT.	88
FIGURE 79: CONCEPT DRAWING OF 90° TETHERS (ORANGE) TO THE 30° TETHER ANGLE CONFIGURATION.....	94

List of Tables

TABLE 1: AN OVERVIEW OF SOME PREVIOUS STUDIES	20
TABLE 2: OVERVIEW OF MODEL TEST DIMENSIONS IN COMPARISON TO PROTOTYPE REFERENCE DIMENSIONS.....	23
TABLE 3: VALUES OF THE SCALED ENVIRONMENTAL CONDITIONS CONSIDERED IN THE LAB EXPERIMENTS IN COMPARISON TO THE UNSCALED REFERENCE VALUE	23
TABLE 4: PARAMETERS BEING VARIED FOR THE MODEL, DURING THE TESTS:.....	26
TABLE 5: THE ENVIRONMENTAL CONDITIONS ORIGINALLY VARIED DURING THE TESTS	26
TABLE 6: THE 6 BASIC REGULAR WAVES CHOSEN TO USE FOR THE ANALYSIS STUDY	26
TABLE 7: THE 3 BASIC CURRENT VELOCITIES CHOSEN TO USE FOR THE ANALYSIS STUDY	27
TABLE 8: THE 12 COMBINED WAVE-CURRENTS CHOSEN FOR THE ANALYSIS STUDY.....	27
TABLE 9: OVERVIEW OF CASES TESTED	27
TABLE 10: FOR ONLY CURRENT CONDITION: THE MEAN AND STANDARD DEVIATION OF HORIZONTAL VELOCITIES, IN THE FIRST TWO COLUMNS, AND THE MAXIMUM AND MINIMUM RECORDED VELOCITIES IN THE LAST TWO COLUMNS	42
TABLE 11: THE VALUES FOR THE COEFFICIENTS USED IN THE FORCE PREDICTION.....	63
TABLE 12: THE VALUES FOR THE COEFFICIENTS USED IN THE FORCE PREDICTION.....	64
TABLE 13: R, THE RATIO BETWEEN THE MEASURED AND PREDICTED FORCE, AND THE STANDARD DEVIATION. FOR HORIZONTAL AND VERTICAL DIRECTIONS.	65
TABLE 14: AN OVERVIEW OF THE OCCURRENCE OF SLACK AND SNAP	74
TABLE 15: THE VERTICAL ACCELERATION SIGNAL 'WAVE' HEIGHT FROM THE ACCELEROMETERS AND FROM THE COMPUTED ACCELERATION. FOR CONFIGURATION $\alpha=70^\circ$ AND $D_s=0.35$ M.....	75
TABLE 16: THE MEAN ERROR FACTORS AND STANDARD DEVIATIONS FOR THE PREDICTION BY THE MORISON.	83
TABLE 17: THE MEAN ERROR FACTORS AND STANDARD DEVIATIONS FOR THE PREDICTION BY THE MORISON PER WAVE. FOR CONFIGURATION 3, WITH $A=70^\circ$ AND $D_s=0.35$ M	83

List of Symbols

u :	The mean current velocity [m/s]
D :	The cylinder diameter [m]
ν :	The kinematic viscosity [m ² /s]
f_v :	Vortex-shedding frequency [1/s]
U :	The flow velocity [m/s]
I_u :	Turbulence intensity [-]
u' :	Velocity fluctuations [m/s]
U_c :	Centre-line velocity [m ² /s]
ρ :	Fluid density [kg/m ²]
P :	The dynamic pressure due to kinetic energy of flowing fluid [$\frac{kg}{m^3} \frac{1}{s^2}$]
U_m :	The maximum fluid velocity [m/s]
T_ω :	The period of the oscillating flow [s]
a :	The amplitude of the oscillatory motion [m]
m' :	The hydrodynamic mass [kg/m]
V :	The volume of the cylinder [m ²]
u_x :	The particle velocity in horizontal direction [m/s]
u_z :	The particle velocity in vertical direction [m/s]
\hat{u}_x :	The amplitude of the particle velocity in horizontal direction [m/s]
\hat{u}_z :	The amplitude of the particle velocity in vertical direction [m/s]
ω :	The radial wave frequency [rad/s]
k :	The wave number [rad/m]
d :	The water depth [m]
z :	The depth of the water particle [m]
c :	Wave phase speed [m/s]
L :	The wave length [m]
T :	The wave period [s]
C_{Dx} :	The drag coefficient in horizontal direction [-]
C_{Dz} :	The drag coefficient in vertical direction [-]
C_{Mx} :	The inertia coefficient in horizontal direction [-]
C_{Mz} :	The inertia coefficient in vertical direction [-]
H_{input} :	The value for the wave height send to the wave generator to make [m]
$U_{c,x}$:	The velocity measured in front of the model, by the EMS at 0.2 m depth [m/s]
$U_{wave,x}$:	The horizontal orbital water particle velocities determined by linear wave theory using the regular wave, undisturbed wave parameter values (T and H). [m/s]
LCX :	The resulting horizontal force component off all tethers combined [N] or when divided by the model dimension [N/m]
LCZ :	The resulting vertical force component off all tethers combined [N] or when divided by the model dimension [N/m]
$LC1'$:	The fluctuating part of the tension force in tether 1 at the front side of the model [N]
$LC2'$:	The fluctuating part of the tension force in tether 2 at the front side of the model [N]
$LC3'$:	The fluctuating part of the tension force in tether 3 at the back side of the model [N]
$LC4'$:	The fluctuating part of the tension force in tether 4 at the back side of the model [N]
α :	The input tether angle [rad]

1

Introduction

1.1 Research Context

Throughout history humans have developed numerous types of infrastructural connections to improve the accessibility between different places. To cross a waterbody a commonly used structure is a bridge. For various reasons alternatives to bridge structures have been applied, like immersed tunnels, floating pontoon bridges and bored tunnels. Even though many types of water crossings already exist, certain environmental conditions might ask for the not yet existing type of crossing, the Submerged Floating Tunnel (SFT).



Figure 1: Alternatives for crossing a waterway (a), the application of a floating bridge over the Donau (b)

A submerged floating tunnel is a tunnel which is put at a certain depth below the water surface and above the bed. This way a submerged floating tunnel can be a serious alternative for environments where the water depth is too large for bridge pontoons to be built, the bed relatively rough or rocky for a tunnel to be placed on or in it, and the water and weather conditions are too wild for a floating bridge. Due to the submergence of the tunnel the direct hydrodynamic forces come mainly from the water currents and less from the waves. Additionally, depending on the design, ships can freely navigate over the tunnel and submarines can navigate past the tunnel as well.

The two main design concepts for the submerged floating tunnel are the pontoon design and the tether design. For the pontoon design the tunnel itself is submerged but connected to pontoons floating on the water surface. Alternatively the tether design is based on the concept of a net positive buoyancy which is counteracted by tensioned tethers attached to the bottom of the water body.

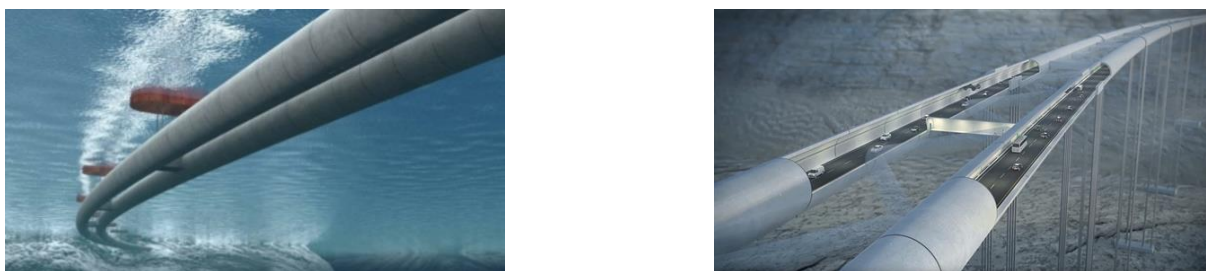


Figure 2: The Two Main Submerged Floating Tunnel Designs: The pontoon design (a) and the tether design (b)

An assessment of the boundary conditions can lead to a preference for either the pontoon or tether design. A disadvantage of the pontoon design is the vulnerability of the pontoons to waves. Whereas for the tether design the disadvantage can be that rocky bed conditions can lead to high mooring costs.

The idea of a submerged floating tunnel was already proposed in 1860 by S. Pr eault, when researching ways to cross the Bosphorus near Istanbul. Although since 1860 the submerged tunnel has been proposed for other locations as well, no design has made it into a realised construction up to this day. However, the interest is still there. For a SFT to be constructed, research must be done on the feasibility of the SFT as a safe strait crossing alternative. One of the aspects to be studied is the effect of the environmental conditions on the structural and dynamic behaviour of the SFT. The effect of the hydrodynamics on the SFT has been covered by some studies. However, increasing the knowledge of especially the behaviour of a SFT in a combined wave-current environment is of interest.

1.2 Problem Statement

In the research field of hydrodynamics around a SFT there is demand for more experimental studies. The outcomes of these studies can contribute to developing design models and to improvement of the existing and future numerical and computational models. These models can be used to accurately predict the behaviour of a real SFT.

1.3 Research Objectives and Questions

The following research objective is given for this study:

To perform small scale flume experiments to develop a better understanding of the effect of the hydrodynamics from a wave, current and combined wave-current environment on a submerged floating tunnel.

Based on this objective, two main research questions were formulated:

1. *What is the relationship found between environmental parameters and the hydrodynamic forces on a fixed small scale tunnel element and how well can these forces be predicted?*
 - I. What is the relationship between the environmental parameters; wave height, wave period, current velocity and submergence depth, and the hydrodynamic forces on a fixed rectangular cylinder in small-scale flume experiments subjected to a regular wave, current and combined wave-current conditions?
 - II. What is the hydrodynamic force prediction accuracy of the Morison equation for a fixed rectangular cylinder in small-scale flume experiments subjected to regular waves and combined wave-current conditions?
2. *What are the kinematic model response and the force tether response of a tethered rectangular cylinder subjected to a regular wave environment in small scale flume experiments? And what is the influence of the structure submergence depth and tether angles on these responses?*

1.4 Report Structure

After the introduction, in Chapter 2 a literature review is given explaining basic concepts relevant for the study and an overview is given of past studies on related subjects. In chapter 3, the outline of the experiments and processing of the study is explained. In chapter 4 the results of the study are presented and analysed. Next, chapter 5 cover a discussion of the results and the study itself. Finally, the report is ended with a reflection on the research question in chapter 6 on Conclusion and Recommendations.

2

Literature Review

In this section an overview is given of theoretical background relevant for understanding the principles of interaction between hydrodynamics and submerged structures. Further a summary is given of recent research done on topics related to the scope of this thesis.

2.1 Theoretical Background

In order to study the interaction between a submerged floating tunnel element and wave-current hydrodynamics, first a brief overview is given of the interaction between a flowing fluid and a submerged object in general. This paragraph is divided in different sections focussing first on the hydrodynamic effects of waves, current and the wave-current combination on a fixed submerged cylinder. Subsequently a closer look is taken at the interaction between hydrodynamics and a structure that will occur for a flexibly mounted submerged cylinder.

2.1.1. Flow Around a Submerged Structure in Steady Current

Flow

When a flowing fluid encounters an object, the fluid will try and flow around the object. Different flowing behaviours can be found depending on the characteristics of the fluid.

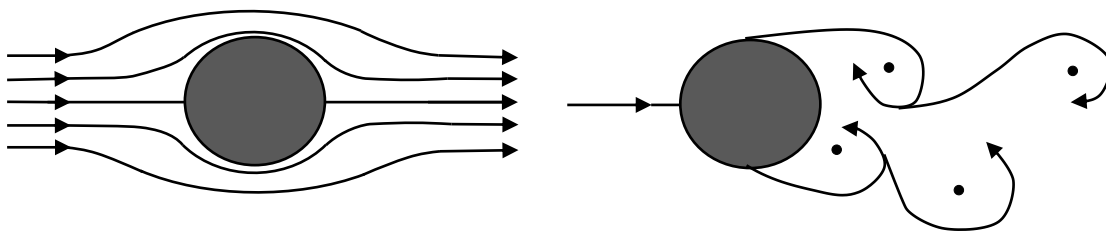


Figure 3: Different streamline patterns of a flowing fluid around a cylindrical object.

One of the quantities often used to describe the flow around an object is the Reynolds number. This dimensionless number represents the ratio between the inertia forces, related to the momentum of the flowing fluid mass, and the viscous forces, the resisting force due to cohesive forces within the fluid itself.

$$Re = \frac{\text{Inertia Forces}}{\text{Viscous Forces}} = \frac{u D}{\nu} (= \frac{\rho D L}{\mu}) \quad [2.1]$$

Where:

- u : The mean current velocity [m/s]
- D : The cylinder dimension, parallel to incoming flow [m]
- ν : The kinematic viscosity [m²/s]
- μ : The dynamic viscosity [kg/m]
- L : the characteristic length, the length along which the boundary layer develops. [m]

Low Reynolds regimes are characterized by laminar flow and high Reynolds regimes by turbulent flow. When increasing the Reynolds number, the fluid will start to separate along the body at a location. The flow along the object before the location of separation is called the boundary layer and the part after separation is called the wake region. Due to an adverse pressure gradient at the lee-side of the body the boundary layer separates and creates a shear layer in the wake region (Fredsoe & Sumer, 2006). Inside the boundary layer vorticity is present. The vorticity transported into the shear layer, causes the layer to roll up and develop a so-called vortex. This development occurs on both the top and bottom side of the body. Depending on the height of the Reynolds number the location of separation moves, the boundary layer is laminar or turbulent and the wake can have symmetric vortices or shedding vortices. The asymmetric shedding of vortices can appear when the shear layer from the top and bottom of the cylinder interact.

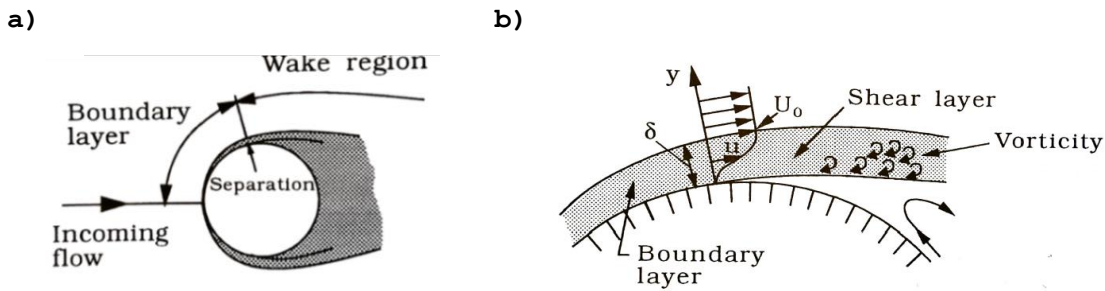


Figure 4: Flow Regions (a) and detailed separation of boundary layer (b), (Fredsoe & Sumer, 2006)

For a circular cross sectional body the separation point moves along the body in the direction of the back of the cylinder for an increasing Reynolds number. However, for bodies with a cross-section with sharp edges the separation point is predetermined at the edges, and thus less Reynolds number dependent. Yet, in specific bluff body and laminar flow cases, flow can be reattached along a body and is separated again at the back of the body (Michelis, 2017).

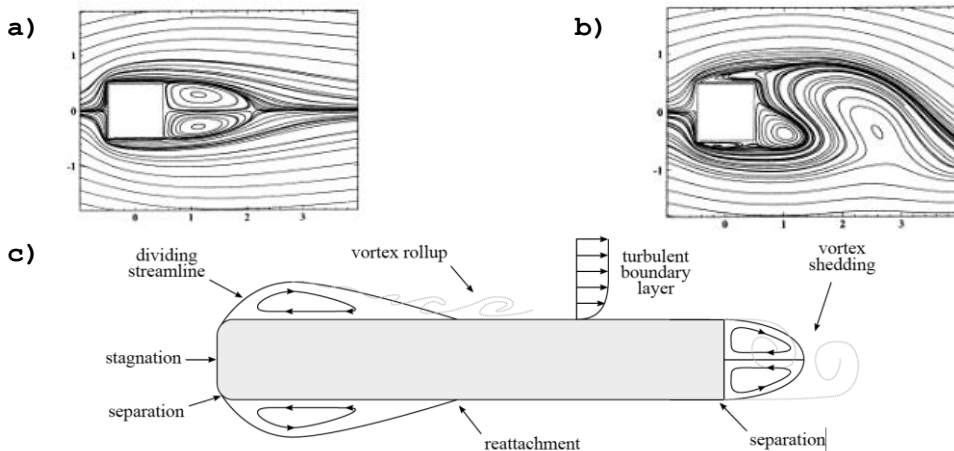


Figure 5: a) and b): Examples of flow around a bluff body (Breuer, 2000). c) Schematization of separation and reattachment around a bluff body (Michelis, 2017)

Forces

Forces are exerted on a submerged body when fluid flows around it. The exerted force is expressed through a pressure component directed perpendicularly to the body surface, and a friction component directed along the surface.

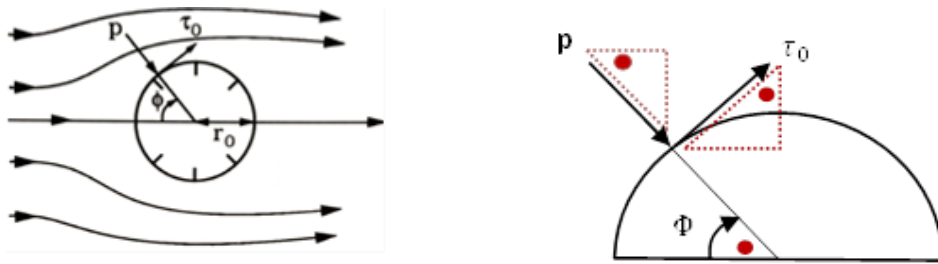


Figure 6: The pressure and frictions components contributing to the force exerted by a flowing fluid on a submerged body. (Fredsoe & Sumer, 2006)

The sum of the contribution of these components in the inline direction of the body is called the mean drag force, $\overline{F_D}$.

In-line pressure contribution:
$$\overline{F_p} = \int_0^{2\pi} \overline{p} \cos(\Phi) r_0 d\Phi$$

In-line friction contribution:
$$\overline{F_f} = \int_0^{2\pi} \overline{\tau_0} \sin(\Phi) r_0 d\Phi$$

Mean drag force:
$$\overline{F_D} = \overline{F_f} + \overline{F_p}$$

The resultant for in the cross-flow direction is called the lift force, F_L . The mean lift force is zero for idealistic cases with uniform flow, a symmetrical body and a zero-angle orientation of the body. However, even with a zero mean, the instantaneous forces are asymmetrical and thus can lead to a cross-flow directed resultant lift force.

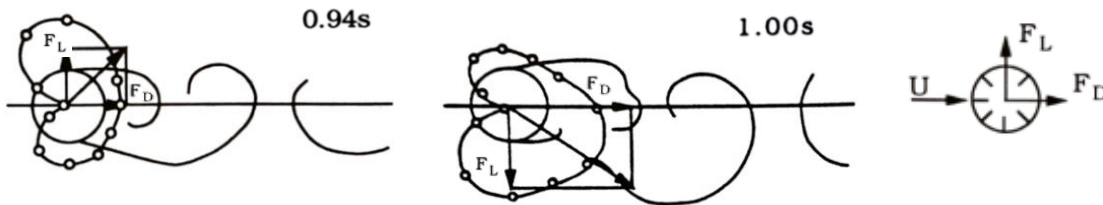


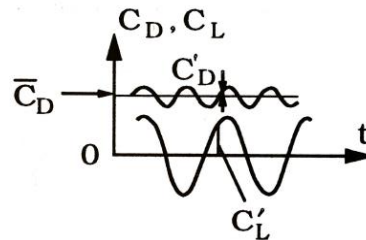
Figure 7: Example Pressure Distribution and Forces on a Cylinder in a Steady Current at Different Times (Fredsoe & Sumer, 2006)

Commonly used parameters to express the lift force and drag force, are the drag and lift coefficients, C_L and C_D .

$$F \propto P * A = \frac{1}{2} \rho D U^2$$

$$C_D = \frac{F_D}{\frac{1}{2} \rho D U^2}$$

$$C_L = \frac{F_L}{\frac{1}{2} \rho D U^2}$$



Drag coefficient [Eq. 1]

Figure 8: Example of fluctuating lift and drag coefficients (Fredsoe & Sumer, 2006)

Where:

- U : The fluid velocity [m/s]
- D : The cylinder diameter [m]
- ρ : Fluid density [kg/m³]
- P : The dynamic pressure due to kinetic energy of flowing fluid [$\frac{kg}{m^3 s^2}$]

It was described before that the flow around a sharp edged cross-sectional cylinder like a square is Reynolds number independent. For a square the mean drag has a value around 2.0, a root-mean squared value of 0.15 and the root-mean squared value of the lift force lays around 0.4.

$$\overline{C_D} = 2.0$$

$$\left(\overline{C_D'^2}\right)^{\frac{1}{2}} = 0.15$$

$$\left(\overline{C_L'^2}\right)^{\frac{1}{2}} = 0.4$$

2.1.2. Flow Around a Submerged Structure in Waves

Flow

An often-used theory to describe the motion of surface gravity waves is the Linear Wave Theory. The theory describes an ideal fluid for which the water is assumed to be: incompressible, to have a constant density, to be continuous, to have no viscosity, the water particles to no leave the water surface of penetrate though the bottom and the only external force to be gravity. (Holthuijsen, 2007). However, the theory can still give an estimation of the waves even for situations non-idealized waves.

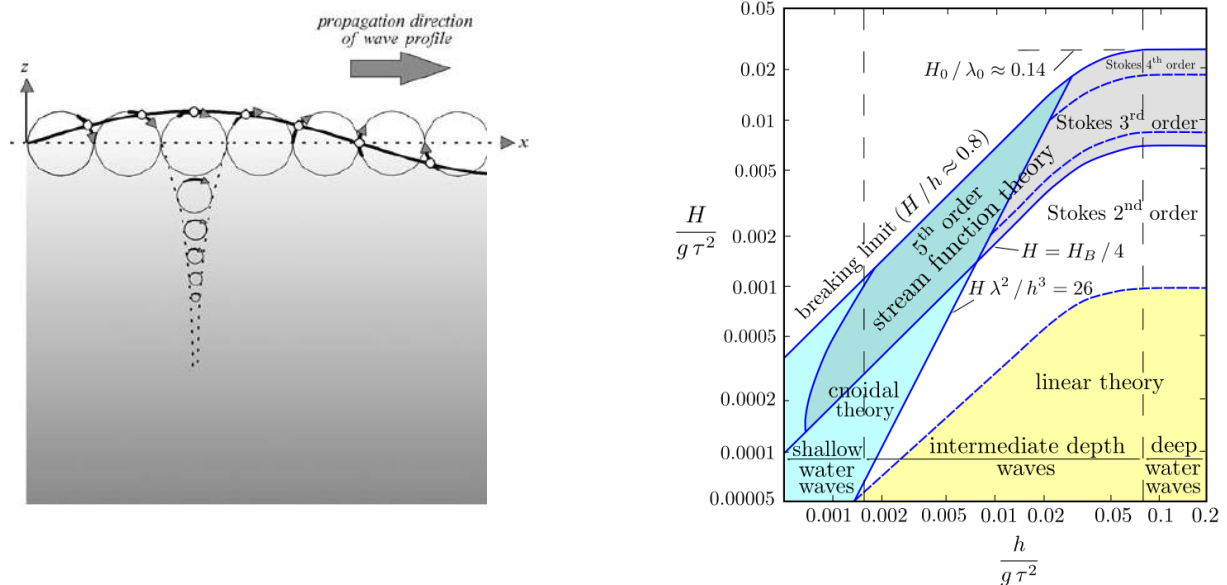


Figure 9: Water particles in orbital motion under a propagating wave in deep water (Holthuijsen, 2007) (left). Validity regions of wave theories (Mehaute, 1976)

With including the assumption of irrotationality of the fluid the velocity potential function is applied in the Linear Wave Theory. The theory results in a harmonic wave with the following kinematic and dynamic wave properties:

A description of the particle velocities (kinematic) (Holthuijsen, 2007):

$$u_x = \hat{u}_x \cos(\omega t - kx) \quad \text{with} \quad \hat{u}_x = \omega a \frac{\cosh[k(d+z)]}{\sinh(kd)}$$

$$u_z = \hat{u}_z \sin(\omega t - kx) \quad \text{with} \quad \hat{u}_z = \omega a \frac{\sinh[k(d+z)]}{\sinh(kd)}$$

$$c = \frac{\omega}{k} = \frac{L}{T}$$

Where:

- u_x : The particle velocity in horizontal direction [m/s]
- u_z : The particle velocity in vertical direction [m/s]
- \hat{u}_x : The amplitude of the particle velocity in horizontal direction [m/s]
- \hat{u}_z : The amplitude of the particle velocity in vertical direction [m/s]
- ω : The radial wave frequency [rad/s]
- k : The wave number [rad/m]
- d : The water depth [m]
- z : The depth of the water particle [m]
- a : The wave amplitude [m]
- c : Wave phase speed [m/s]
- L : The wave length [m]
- T : The wave period [s]

The dispersion relationship is an implicit formula. Through iteration of the wave number an result can be obtained.

The dispersion relationship (dynamic) (Holthuijsen, 2007):

$$\omega^2 = gk \tanh(kd) \quad \text{or} \quad L = \frac{gT^2}{2\pi} \tanh\left(\frac{2\pi d}{L}\right)$$

An expression for the phase speed (dynamic) (Holthuijsen, 2007):

$$c = \frac{g}{\omega} \tanh(kd) = \sqrt{\frac{g}{k} \tanh(kd)}$$

Forces

In the past paragraph, an expression was given for the in-line force and the cross-flow force acting on a submerged cylinder as a result of a flow around the body. In case of an oscillating flow the force expression changes.

First of all, the In-line force expression is extended with a hydrodynamic mass force expression and the Froude-Krylov force. The in-line force in case of oscillatory flows:

$$F = \frac{1}{2} \rho C_D D U |U| + \underbrace{m' \dot{U}}_{\text{Hydrodynamic mass force (Disturbed field)}} + \underbrace{\rho A \dot{U}}_{\text{Froude-Krylov force (Undisturbed field)}}$$

The variables are explained in the following paragraphs.

The Froude-Krylov force accounts for the force in the fluid caused by a horizontal pressure gradient in an undisturbed flow:

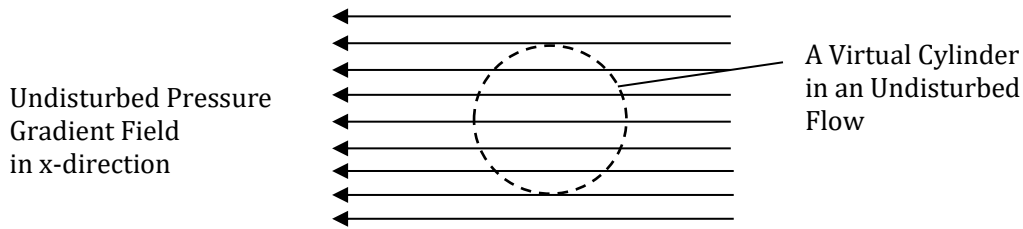


Figure 10: A schematisation of a undisturbed pressure flow field, and a virtual cylinder (OE4620, November 2005).

The pressure gradient can be expressed in terms of the acceleration of the flow.

$$\frac{\partial p}{\partial x} = \rho \frac{du}{dt} = \rho \dot{u}$$

Where:

- p : Pressure in the flow [N/m²]
- ρ : Fluid density [kg/m³]
- U : Velocity of the flow [m/s]
- \dot{U} : The acceleration of the flow [m/s²]

The undisturbed pressure field acting on the parameter of a structure leads to the following simplified expression of a force, the Froude-Krylov force:

$$F_{Krylov} = \rho \pi R^2 \dot{U} = \rho A \dot{U}$$

Where:

- R : The radius of the structure [m]
- ρ : Fluid density [kg/m³]
- A : The cross sectional area of a structure [m²]
- \dot{U} : The acceleration of the flow [m/s²]

However, the flow is disturbed by the presence of a structure. The flow is forced to move around the structure. The cylinder acting on the fluid, results in local velocities and accelerations. The force representing the mass of fluid that is accelerated because of the disturbances is accounted for by the Hydrodynamic mass force:

$$F_{hydro,mass} = m' \dot{U}$$

$$m' = \rho C_a A$$

Where:

- m' : The hydrodynamic mass per unit length cylinder [kg/m]
- A : The cross sectional area of a structure [m²]
- C_a : The coefficient of added mass [-]

In here the C_a coefficient for added mass represents the force per unit acceleration.

Together the two forces, F_{Krylov} and $F_{hydro,mass}$, lead to the expression for the inertia force. The inertia force together with the earlier presented drag force, lead to the Morison Equation by Morison (1950), for a circular cross-section:

$$F = \underbrace{\frac{1}{2}\rho C_D D U |U|}_{F_D, \text{ Drag Force}} + \underbrace{\rho C_M A \dot{U}}_{F_M, \text{ Inertia Force}}$$

with:

$$C_M = C_a + 1$$

Originally the application of the Morison equation was a vertically submerged cylinder, for which only the water particle velocity in horizontal direction was taken into account. For a horizontally submerged cylinder, the vertical water particle velocity component is also relevant. This leads to the following equations for a rectangular submerged cylinder in waves:

$$F_x = \frac{1}{2}\rho C_{Dx} D U_x \sqrt{U_x^2 + U_z^2} + \rho C_{Mx} A a_x$$

$$F_z = \frac{1}{2}\rho C_{Dz} B U_z \sqrt{U_x^2 + U_z^2} + \rho C_{Mz} A a_z$$

Where:

- ρ : The density of the fluid [kg/m³]
- A : The frontal area of the cylinder [m²]
- D : The cylinder dimension, in vertical direction [m]
- B : The cylinder dimension, in horizontal direction [m]
- C_{Dx} : The drag coefficient in horizontal direction [-]
- C_{Dz} : The drag coefficient in vertical direction [-]
- C_{Mx} : The inertia coefficient in horizontal direction [-]
- C_{Mz} : The inertia coefficient in vertical direction [-]
- a_x : The water particle acceleration in horizontal direction [-]
- a_z : The water particle acceleration in vertical direction [-]
- U_x : The water particle velocity in horizontal direction [-]
- U_z : The water particle velocity in vertical direction [-]

Here separate force coefficients have been assigned per force direction. A study by Chaplin (1985), confirmed that this leads to a good prediction of the measured force.

Since the velocity and the acceleration are 90 degrees out of phase, so are F_D , the drag force, and F_I , the inertia force.

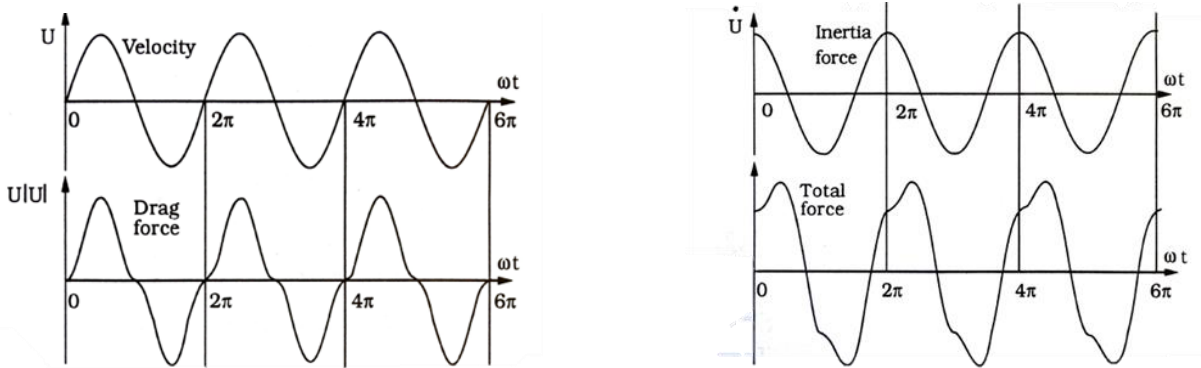


Figure 11: Example signal of velocity related drag forces and acceleration related inertia forces, combined to the total force. (Fredsoe & Sumer, 2006)

An often-used parameter to describe the influence of an oscillating flow around an object is the Keulegan-Carpenter number, KC number.

$$KC = \frac{U_m T}{B}$$

Where:

- U_m : The maximum amplitude of fluid velocity [m/s]
- T : The period of the oscillating flow [s]
- B : The model dimension normal to the wave crest [m]

The magnitude of KC number can be an indication for either drag or inertia force dominance on a structure. The equation below shows how the KC number is used to study ratio between the drag and inertia component of the force:

$$\begin{aligned} \frac{F_{drag}}{F_{inertia}} &= \frac{1}{\pi^2} \frac{C_D}{C_M} \frac{U_m T}{B} \\ &= \frac{1}{\pi^2} \frac{C_D}{C_M} KC \end{aligned}$$

2.1.3. Flow Around a Structure in a Wave-Current Condition

The interaction of combined waves and current is a separate research topic. For a simplified situation it can be assumed that the current velocity, U_c , and the oscillation velocity, U_m , are two non-interacting components of the total velocity U .

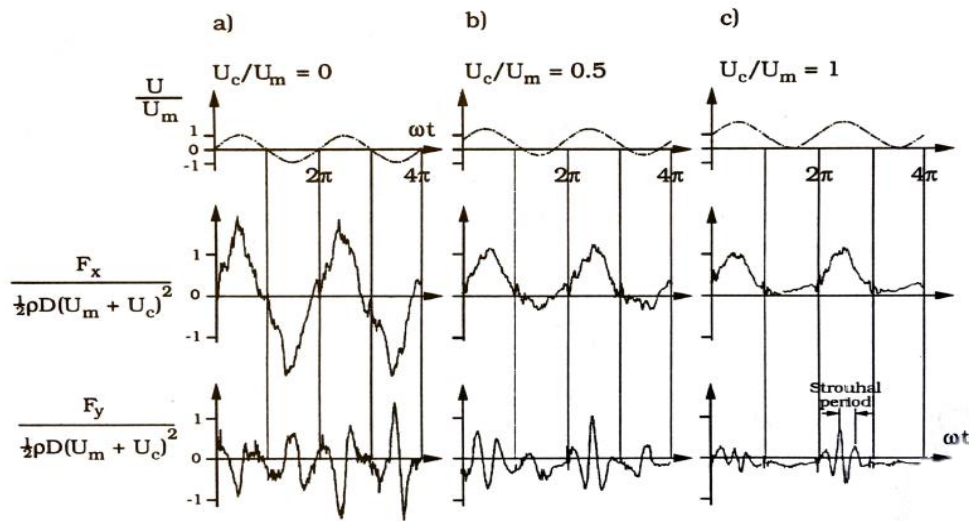


Figure 12: Signals of different variables for varying wave-current conditions (Fredsoe & Sumer, 2006)

The adjusted Morison equation for this case becomes:

$$F_x = \frac{1}{2} \rho C_{Dx} D U_x \sqrt{U_x^2 + U_z^2} + \rho C_{Mx} A a_x$$

$$F_z = \frac{1}{2} \rho C_{Dz} B U_z \sqrt{U_x^2 + U_z^2} + \rho C_{Mz} A a_z$$

Where:







$$U_x = U_c + U_m \sin(\omega t)$$

$$a_x = U_m \omega \cos(\omega t)$$

2.2 Physical Modelling Practice

Studies carried on the topic of cylinders in oscillating flow mainly focussed on circular shaped cylinder cross-sections. Research on studying the influence of shape is of value because for cylinders with a sharp edged cross-sectional shape a wider wake and vortices, resulting in larger drag coefficients, are not found only at high KC numbers, but for low KC numbers as well. Some researches done in the past on non-circular cylinder cross-sections is listed below:

Table 1: An overview of some previous studies

	Set-up type	Cross-section	Findings
Bearman et al. (1979)	U-tube: Fixed cylinder in harmonically oscillating fluid	   	<ul style="list-style-type: none"> ▪ The cross-sectional shape influences the relationship between C_M and KC ▪ In general C_D decreases for and increasing KC for
Ikeda et al. (1988b)			<ul style="list-style-type: none"> ▪ At low KC-numbers, C_M decreases fast for an increasing KC, due to the Magnus effect: circulating flow creating a lift force.
Arai (1993)			<ul style="list-style-type: none"> ▪ For $KC > 1$, C_{Mz} decreases for an KC increase.
Arai (1995)			<ul style="list-style-type: none"> ▪ Circulation of flow almost proportional to KC^2
Koterayama and Hu (1995)			<ul style="list-style-type: none"> ▪ Flow separation creates more complex force coefficients for rectangular cross sections compared to circular cross-sections. ▪ C_M and C_D are considerably larger for rectangular cylinders than for circular.
V. Venugopal et. Al. (2006)	Wave flume: Low KC-numbers Larger β 's		<ul style="list-style-type: none"> ▪ At low KC-numbers large and rapidly decreasing C_D's are found, due to flow separation and vortices starting to appear. ▪ At low KC-numbers the value of C_M is close to that in potential flow. Circulating flow around the cylinder gives a decreasing C_M for an increasing KC-number ▪ β showed to be of no significant influence on the coefficients, so no Reynolds number related effects. ▪ Lower C_M values are found for smaller submergence depths.

3

Methodology

Physical modelling tests have been performed to study the forces caused by waves and/or current acting on a submerged floating tunnel and the associated tunnel response. This chapter describes the used experiment set-up, the method for acquisition of data and the data processing methodology.

3.1 Experiment Set-up

The experiments were conducted in a flume at the Fluid Mechanics Laboratory of the Delft University of Technology. This paragraph describes the model design and prototype reference, flume characteristics, the model set-up and the instrument plan.

As described in the research questions, two basic model designs are applied: a fixed model and a tether model. A schematisation of the two basic designs is shown in Figure 13 together with pictures of the model in the flume in Figure 14.

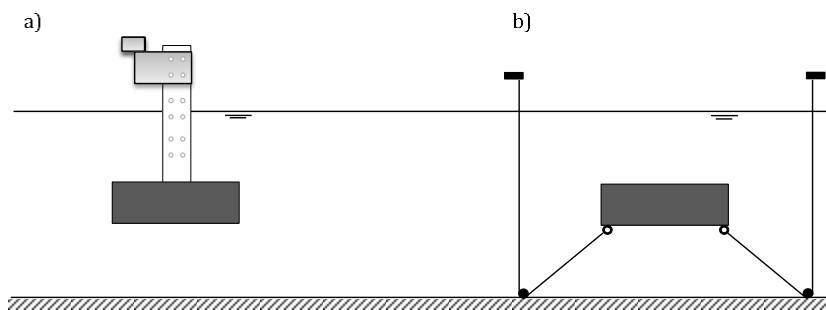


Figure 13: Schematisation of Fixed Model, model no.1 (a), and Tether Model, model no. 2 (b), side plan.

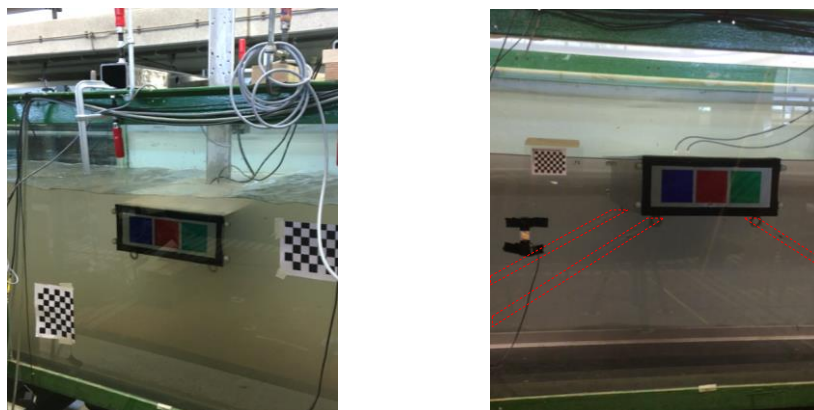


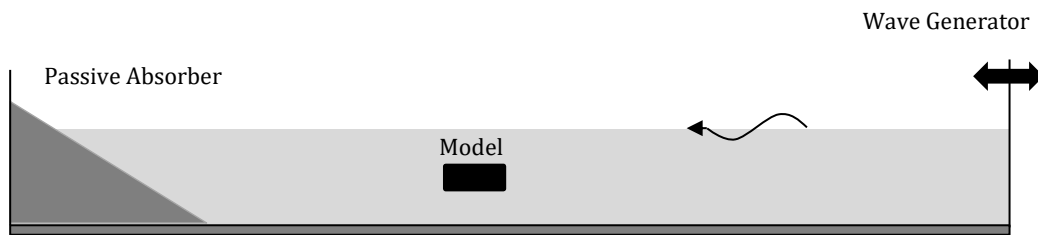
Figure 14: Pictures of the model no.1 (left) and model no.2. (right) in the flume. The red dashed lined boxes enclose the tether lines.

3.1.1. Flume Characteristics

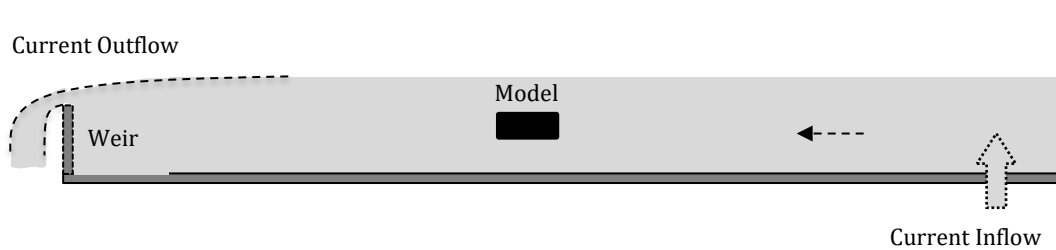
The laboratory flume used for the experiments has a length of 42 m, a width of 0.8 m and a maximum water depth of 1 m. During the tests, a constant water level of 0.70 m was applied to guarantee the water would remain at a safe distance from the top edge of flume wall. Waves were generated by a wave generator combined with an Automatic Reflection Compensation (ARC) function. At the opposite side of the flume a passive wave absorber was placed inside the flume for tests considering waves. Current was generated by water pumped from the basement water basin into the flume in front of the wave generator.

A schematisation of the flume is presented in Figure 15.

a) Regular Waves set-up



b) Current set-up



c) Combined Wave-Current set-up

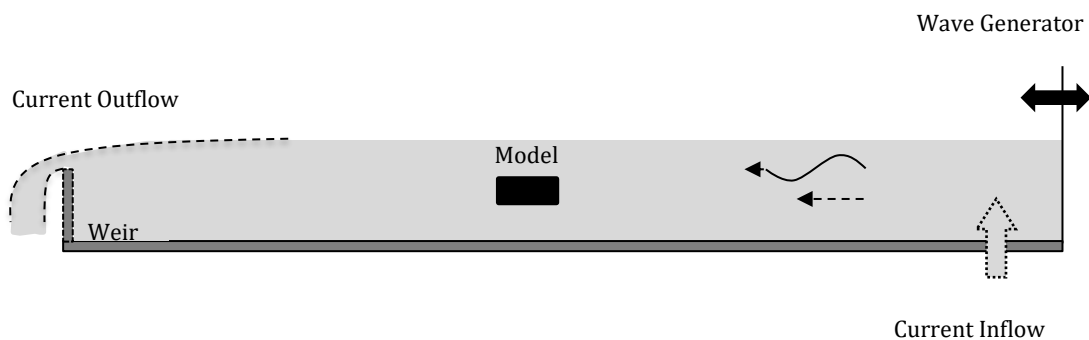


Figure 15: Side plan of Flume set-up (N.T.S.) for wave experiments and current flow experiments.

3.1.2. Model Design and Prototype Reference

The starting point for the design of the model and the environmental conditions, is a prototype reference. The model dimensions represent a typical immersed tunnel. The environmental conditions are determined by characteristic submerged floating tunnel locations such as fjords and ocean strait crossings. An estimation of wave and current conditions to be expected at such locations together with values used in past researches have been used as a starting point to select the model dimensions and conditions.

The general scaling ratio of the experiments was equal to 1:50. As a result prototype tunnel element dimensions of 40 meters length, 20 meters width and 8 meters height correspond to model dimensions of 0.792 meters length, 0.40 meters width and 0.16 meters height.

The submergence depth of the model is limited by the dimensions of the flume. Ensuring enough distance between the model and the flume bottom for wall proximity effects to be negligible, gives a maximum submergence depth of 0.35 m. A model submergence depth of 0.35 m corresponds to a reference submergence depth of 17.5 m.

Table 2: Overview of model test dimensions in comparison to prototype reference dimensions

	Model Dimensions	Typical Reference Dimensions
Width [m]	0.40	20
Height [m]	0.16	8
Length [m]	0.792	40
Maximum Submergence Depth, d_s [m]	0.35	17.5

The upper limit values of the environmental conditions: wave height, wave period and current velocity are determined from a few reference locations and scaled down with the use of Froude scaling.

$$H_{s,model} = \lambda H_{s,prototype}$$

$$T_{s,model} = \sqrt{\lambda} T_{s,prototype}$$

$$u_{model} = \sqrt{\lambda} u_{prototype}$$

Table 3 presents the upper limits of the parameters used in this study.

Table 3: Values of the scaled environmental conditions considered in the lab experiments in comparison to the unscaled reference value

Upper limits:	Model Values	Typical Reference Values
H, wave height [m]	0.16	8
T, wave period [s]	1.84	13.01
U_c , current velocity [m/s]	0.40	2.83

3.1.3. Model Set-up

An elaborate description of the two model set-ups is given in this paragraph. The set-ups were designed based on the reference situations and on practical lab restrictions., described in the previous section covers a description of how the following variables described in the research questions are accounted for:

- The Submergence Depth (d_s)
- The Tether Angle (α)

Fixed Model

The model, model no. 1, used for most of the performed fixed model tests comprises a stainless-steel box element with a connection strip attached to the lit of the box. The strip is connected to a force sensor. The strip can be connected to the force sensor at different locations, resulting in a variety of submergence depths to be applied. The force sensor is attached to a supporting beam rigidly fixed to the flume.

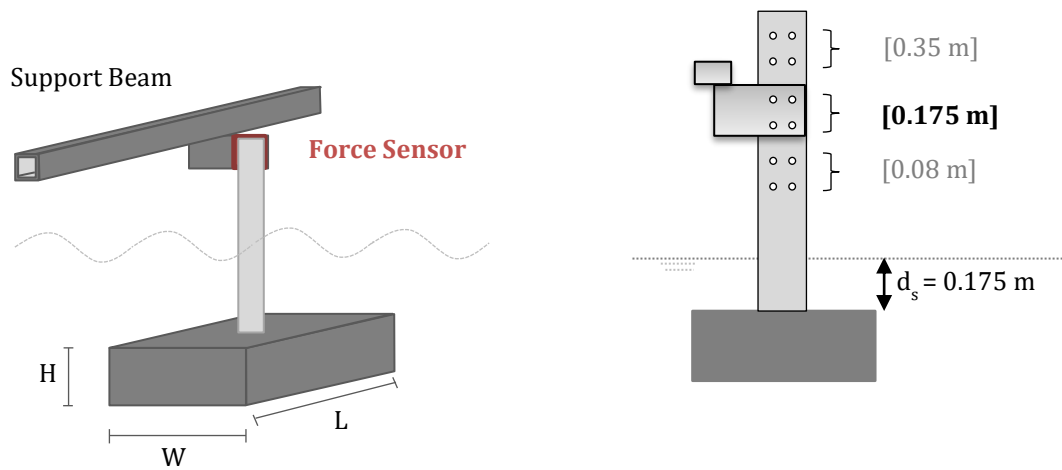


Figure 16: A schematisation of the general design for model no. 1 and variable submergence depth, d_s , with the connecting strip.

The weight of the empty model no. 1 is 15.4 kg. Additional weight was added to a total weight 74.4 kg. This weight was desired because it has the same value as some experiments done at an earlier stage of the study but which were not used for the results. A description of these experiments and the model configurations used in those tests is summarized in Appendix B.

The total static vertical force working on model is the difference between the weight of the model directing downward and the upward directed buoyant weight given with the following expression:

$$F_{buoyant} = W * H * L * \rho_{water} = 0.4 * 0.16 * 0.795 * 998 = 50.8 \text{ kg}$$

Where:

W :	The width of the model [m]
H :	The height of the model [m]
L :	The length of the model [m]
ρ_{water} :	The density of the fluid (water) [kg/m ³]

With a model weight of 74.4 kg and a buoyant weight of 50.8 kg, model no 1 has a net downward directed force.

Tether Model

The tether model, model no. 2, was designed to study the response of the submerged model due to the hydrodynamic forces found in the fixed model test. The same box was used as for the forced model, except that the connecting strip was removed, and the added weight was changed to create a net upward force working on the model. For most tests, a Buoyance to Weight Ratio (BWR) of 1.5 was used. For a BWR 1.5 a model weight of approximately 33.7 kg was applied. A specification of the weight distribution can be found in Appendix B.

The model experiences the following buoyant force:

$$BWR = \frac{F_{buoyant}}{F_{model}}$$

$$\text{For a 1.5 BWR: } \frac{F_{buoyant}}{33.7} = 1.51$$

In all cases light weighted foam was used to fix and elevate the added weights to locate the centre of mass at half height of the model.

For the tether model an additional variable to study, is the influence of the tether angle, α . Two different angles are executed during the tests, $\alpha=30^\circ$ and $\alpha=70^\circ$. The tethers are attached to the bottom of the model through rings. The tether run downward from the ring to the flume bottom, where it runs over a pulley before going straight up with a right-angle to the top of the flume. The pulley system can be seen *Figure 19* in the next section.

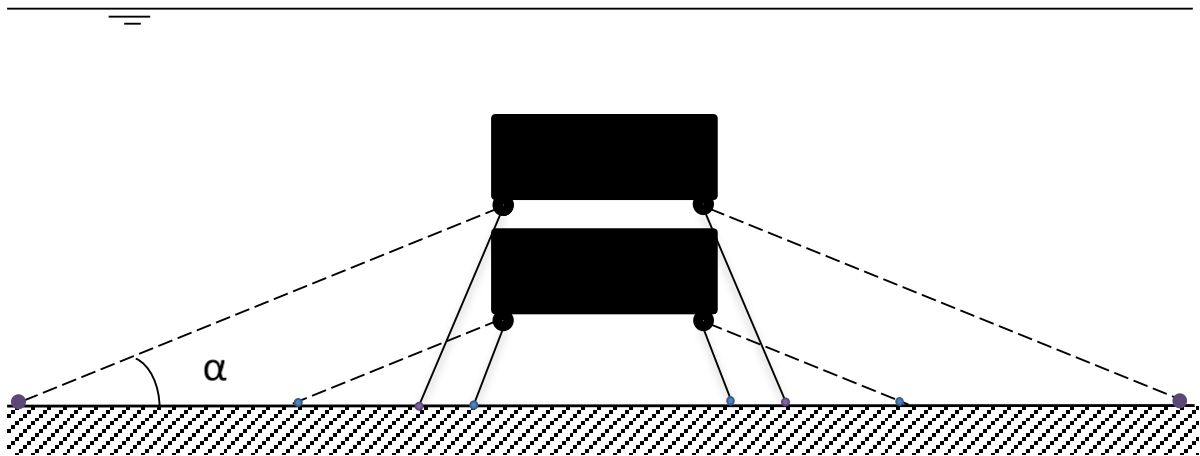


Figure 17: The different tether angle-depth configurations. The dashed line (- -) portrays the $\alpha=30^\circ$, the solid line (-) the $\alpha=70^\circ$.

3.2 Data Scope

As described in the research questions and the previous paragraph, several parameters are varied during the tests:

Model Variables:

Table 4: Parameters being varied for the model, during the tests:

Parameters	Unit	Values Tested	Tested for Model Type:
Tether angle, α	°	30 and 70	Tether Model
Submergence Depth, d_s	m	0.08, 0.175 and 0.35	Tether Model and Fixed Model

Environmental Conditions:

Table 5: The environmental conditions originally varied during the tests

Parameters	Unit	Values Tested	Tested for Model Type:
H, wave height	m	0.02 0.08, 0.12 and 0.16	Tether Model and Fixed Model
T, wave period	s	0.92, 1.13, 1.41, 1.84	Tether Model and Fixed Model
U_c , current velocity	m/s	0.10, 0.20, 0.30 and 0.40	Tether Model and Fixed Model

Combining all model variables to all environmental conditions leads to almost 1100 unique tests. Most of the combinations have been tested, an overview is given in Appendix A. Because the processing of all the data would takes too long, a cut was made in the data. Tests to be processed were chosen such that enough data points are available to distinguish a trend for the environmental parameters of interest. The following data scope, regarding the environmental conditions was chosen.

6 Basic Regular Waves:

Table 6: The 6 basic regular waves chosen to use for the analysis study

	Basic Test ID					
	R12	R13	R14	R22	R32	R42
Wave Period [s]	0.92	0.92	0.92	1.13	1.41	1.84
Wave Height [m]	0.08	0.12	0.16	0.08	0.08	0.08

3 Basic Current Velocities:

Table 7: The 3 basic current velocities chosen to use for the analysis study

	Aimed velocity
Current 1	0.1 m/s
Current 2	0.2 m/s
Current 2	0.3 m/s

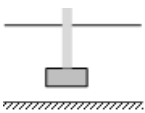
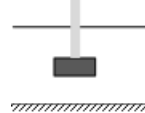
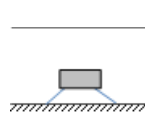
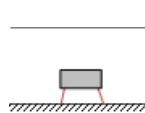
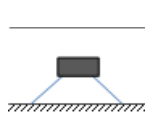
12 Basic combined waves-currents:

Table 8: The 12 combined wave-currents chosen for the analysis study

Current		Wave	Wave-Current		
Current II	(0.2 m/s)	X	6 Basic Waves	=	6 tests
Current III	(0.3 m/s)	X	6 Basic Waves	=	6 tests

To test the influence of all model variables and hydrodynamic conditions 5 cases are studied in the analysis. The 5 cases are presented below in Table 9.

Table 9: Overview of cases tested

	Case 1	Case 2	Case 3	Case 4	Case 5
	Fixed	Fixed	Tether	Tether	Tether
Tested Variables					
Regular Wave	6 Basic	6 Basic	6 Basic	6 Basic	6 Basic
Current	3 Basic	3 Basic			
Wave-Current	12 Basic				
Aim to study	C_M & C_D	d_s	Motions	α	d_s

the influence of

3.3 Data Acquisition

This paragraph describes how raw data is gathered during the experiments. It explains which instruments were used during the experiments in the lab and how the instruments were positioned. The output of all instruments was in Voltage. The instrument plans are described separately for the Fixed Model and the Tether Model.

3.3.1 Fixed Model

The following instruments have been used to perform the fixed model tests:

- 7 Wave gauges
- 1 EMS (Electromagnetic liquid velocity meter)
- 1 Force Sensor
- 1 Moment Sensor

The position of the wave gauges was determined by the required relative distance between the gauges to detect reflection. This distance is $1/3$ of the wave period. Four wave gauges were positioned in front of the model and two wave gauges were positioned at the back of the model to detect the reflection from the back of the flume. One additional wave gauge was positioned closer to the wave paddle.

The EMS was placed in front of the model, at a fixed depth. However, some extra tests were executed with a varying EMS depth to study the depth influence on the velocity signal. As for the force sensor, it was located in top the model above the water surface, attached to the support beam as in Figure 16.

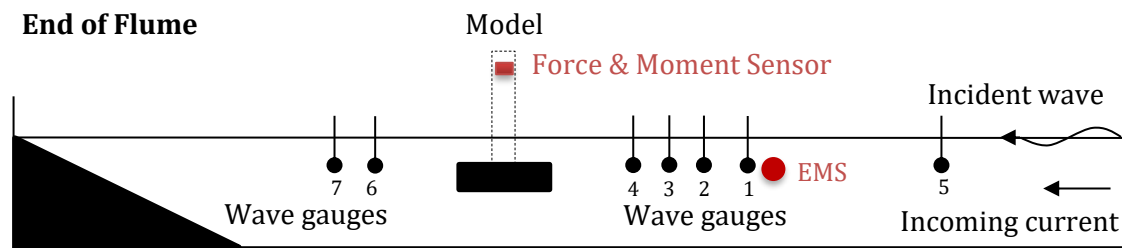


Figure 18: Position of instruments used for the fixed model designs (N.T.S)

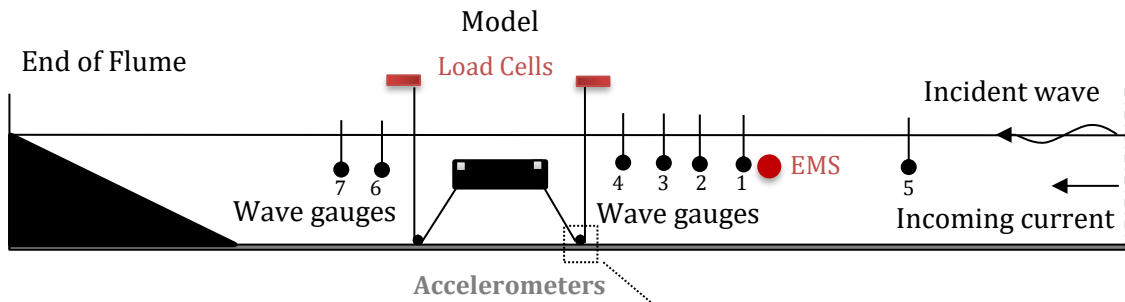
3.3.2 Tether model

The following instruments have been used to perform the Tether model tests:

- 7 Wave Gauges
- 1 EMS (Electromagnetic liquid velocity meter)
- 2 Accelerometers
- 4 Load cells
- 1 Video Camera (4k)

The location of the EMS and wave gauges is equal to the positions for the Fixed model experiments. Four accelerometers were attached to each corner of the lit inside the model. These were placed inside the model to prevent contact with water. In addition, four load cells we placed outside the flume fixed to support beams. Each load cell is connected to a wire reaching to the bottom of the flume perpendicularly. From there the wire is laid around a 'frictionless' wheel guiding the wire to the corners of the bottom of the model under an angle.

Side View



Plan View

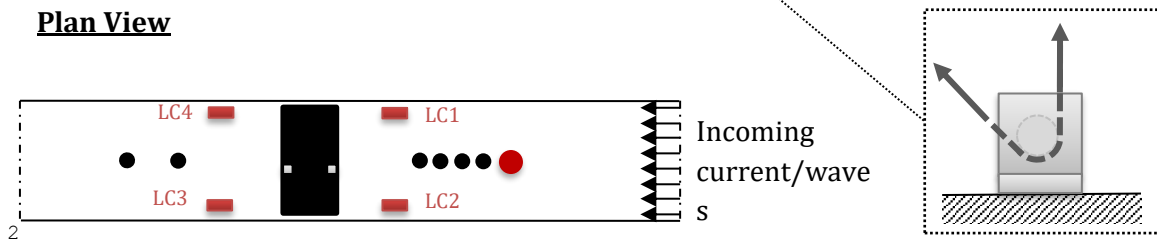


Figure 19: Top view and Plan view of the instrument distribution in the flume (N.T.S.) and a detail of a pulley/wheel

On the side of the model facing the glass window, three coloured markers were drawn, see Figure 20. By tracking these markers with the video camera, the displacements of the model was computed.

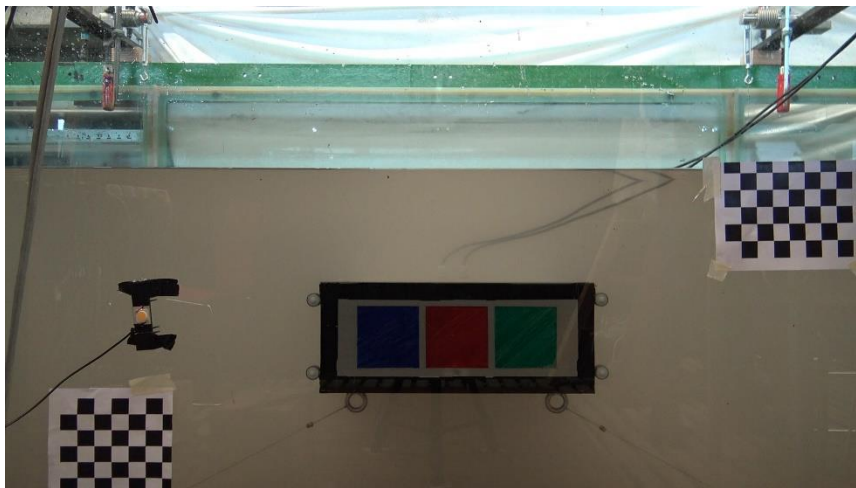


Figure 20: Side view of the tether model with the blue, red and green trackers on drawn on it.

3.4 Processing Methodology

3.4.1 General Processing Procedure

Every test performed in the lab flume was recorded with multiple instruments. A voltage record was written for every instrument during a test and written in a data file combining the records of all instruments, creating a ASC-file. For the tether model tests additional video records were made as well. Both the instrument data files and possible video files were processed in Matlab. A calibration factor and offset values were applied with the use of Matlab. Through this process raw data records were transformed into calibrated data records.

After calibrating the records, a Matlab processing script was written to extract points of interest from the records. The script recognizes the increase of the record amplitude, reaching a 'maximum', given the red dot. The value of this maximum is registered as well as the time it takes for the next peak to occur, the 'period'. This next peak is taken as the starting point of a section of multiple peaks, the green part of the signal. The mean peak value of the green section is registered as well as the mean period

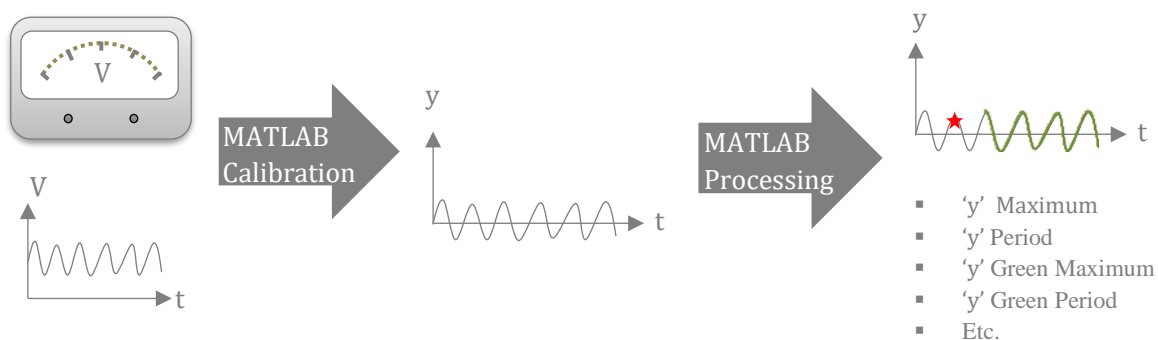


Figure 21: Schematization of Calibrating and Processing Instrument Records

For processing the video records a similar processing procedure was applied. A MATLAB script was used to track the blue, red and green square markers on the side of the model and translate it into displacement signals plotted against the same time axis as the other instrument records. This time synchronization was established with the use tracking a LED signal which was both visible in the videos and in the instrument ASC-file.

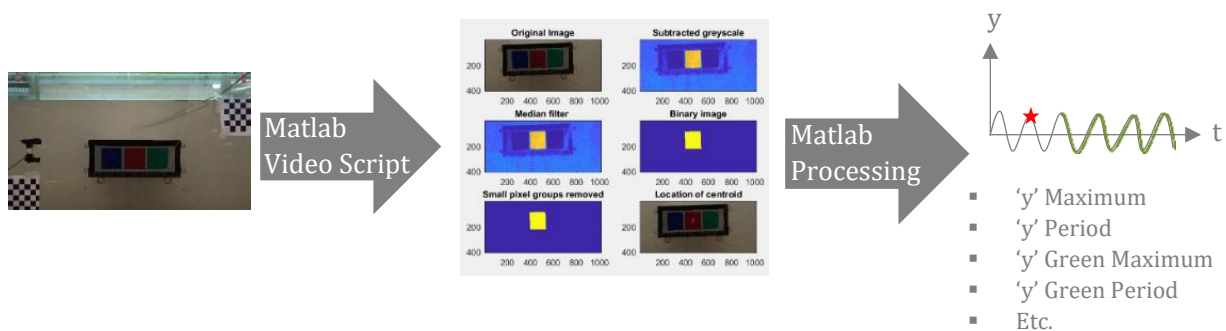


Figure 22: Schematization of the Processing of Video Records

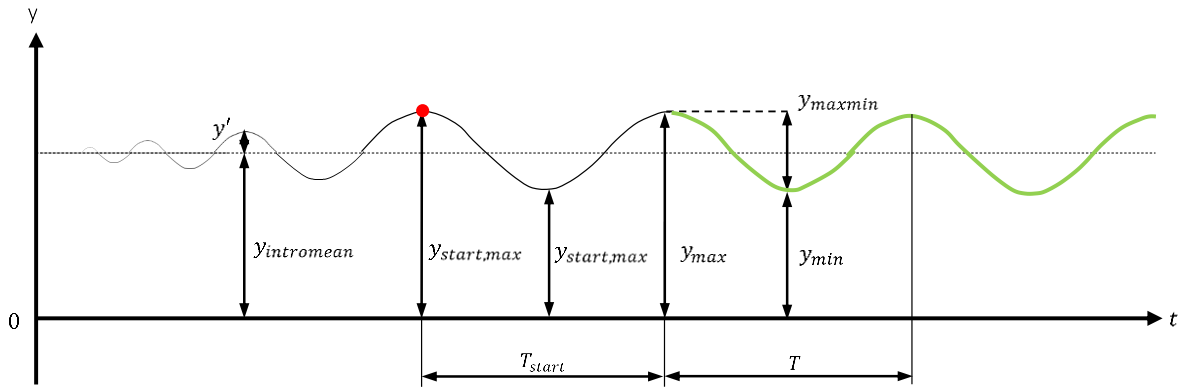


Figure 23: Schematization of parameter definitions, used in record processing

After the processing by MATLAB the following typical parameters, illustrated in Figure 23, would have been collected, in which y can be replaced by any variable:

- $y_{intromean}$: The mean value of the first part of the record, where no wave is present yet
- y' : The relative value of a peak to the intro mean value
- $y_{start,max}$: The absolute value of the red peak
- $y_{start,min}$: The absolute value of the first trough after the red peak
- y_{max} : The absolute value of a peak
- y_{min} : The absolute value of a trough
- y_{maxmin} : The value of $(y_{max} - y_{min})$

3.4.2. Velocity Signal Computations

For the present study the velocity need of the analyses is, the velocity at location of the centre of the model. Since it is physically impossible to do this with an EMS, the measurement device was installed at 0.2 m depth a few meters in front of the model. The 0.2 m depth was kept unchanged during the tests, to limit adjustment errors. The depth was changed only for a few separate tests in which the velocity at different depths was studied. The EMS was placed several meters in front of the model at a location where it was assumed no disturbances due to the model itself would be present.

End of Flume

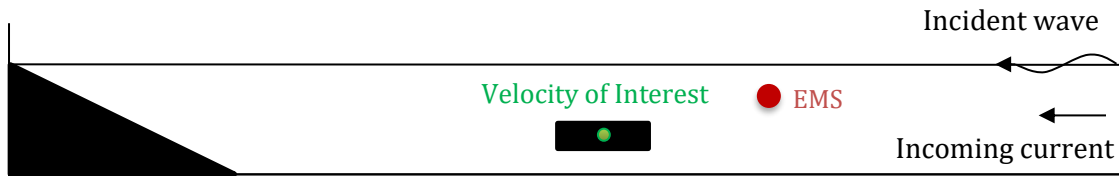


Figure 24: The location of the velocity measured by the EMS and the location of the velocity of interest at the centre of the model.

Since the velocity was not measured at the location of interest for the analysis, a couple of computations were made and measures were taken to approximate the velocity at the model. These are described in this section per environmental condition.

Only current

In case of test with including only current, horizontal velocities are needed at the actual depth of the model. Some tests were done to measure the influence of the EMS depth on the magnitudes of the recorded velocities. The depth-velocity profiles found are plotted in Figure 25. The red line indicates the 0.2 m depth of the EMS used in this study. The two blue lines indicate the depth of at $\frac{1}{2}$ of the model height, needed for the analyses in this study. For the range of depths of the present study, the change of velocity magnitude due to the depth was found not to be significant.

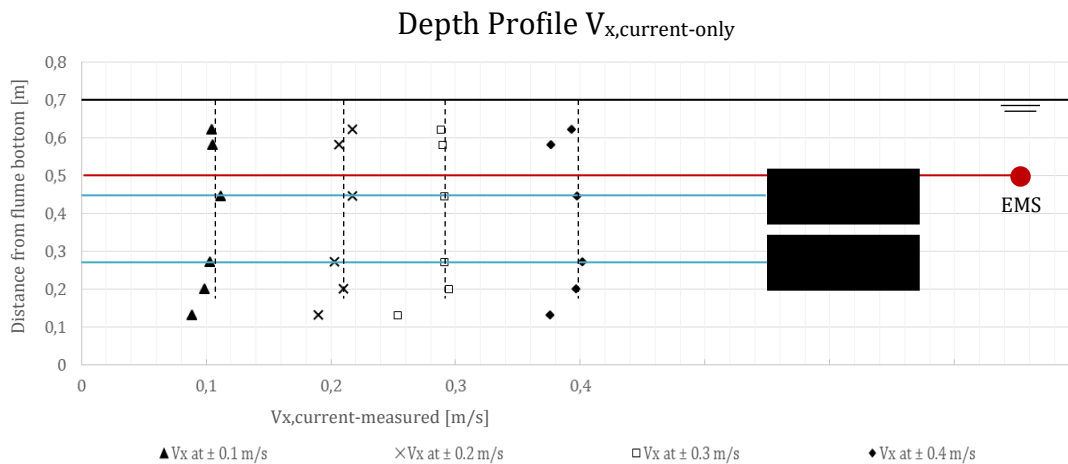


Figure 25: Velocity depth profiles of different input current velocities. And a schematization of the half tunnels heights of 0.175 m and 0.35 m tunnel submergence depth (blue) and the EMS depth during most of the experiments (red).

To conclude, no velocity computations are made for the current tests. There for the used velocity is equal to the measured velocity at the depth of the EMS:

$$U_{c,x} = U_{c,x,measured}$$

Regular Waves

For the analysis of the test with regular waves the centre of the model is of interest. To come to this velocity, two computations have to be made. One to account for depth shift of the velocity and one to account for the horizontal time shift of the velocity. The depth and time shifts applied to a velocity record is shown in Figure 26. After the figure the depth shift is discussed first.

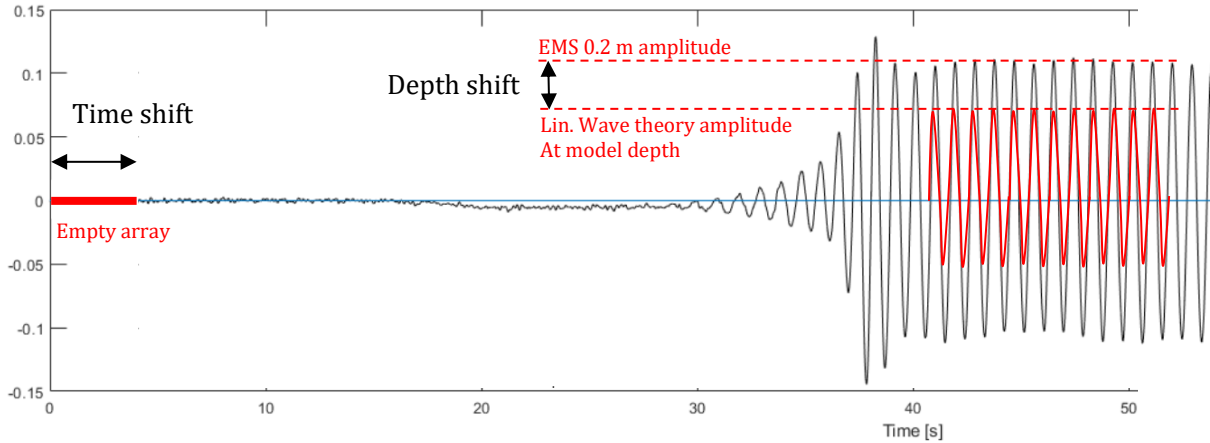


Figure 26: Depth and time shift applied to a water velocity record.

1. Depth shift:

To create a velocity signal for the velocities at the centre of the model, a sinusoidal function is created with an amplitude and wave period component:

$$u_x = \hat{u}_x \cos\left(\frac{2\pi}{T_{section}} t\right)$$

$$u_z = \hat{u}_z \sin\left(\frac{2\pi}{T_{section}} t\right)$$

Where:

u_x : The horizontal orbital velocity at the depth of the model [m/s]

u_z : The vertical orbital velocity at the depth of the model [m/s]

\hat{u}_x : The amplitude of horizontal orbital velocity at model depth from linear wave theory [m/s]

\hat{u}_z : The amplitude of horizontal orbital velocity at model depth from linear wave theory [m/s]

$T_{section}$: The mean period found in the analysis section of the EMS record [s]

The amplitudes, \hat{u}_x and \hat{u}_z , used in this function are the linear wave theory amplitudes of orbital velocities, described in section 2.1.2. The values of these amplitudes can be found in Appendix **Fout! Verwijzingsbron niet gevonden..** The period for these functions is the mean period found in the section of the EMS velocity record for the analysis. To conclude the computed velocity signals consist of a sinusoidal signal with a period equal to the period found in the recorded velocity at 0.2 m depth and a amplitude from linear wave theory.

2. Time shift:

When a wave propagates towards the model it arrives at the EMS a few seconds before it arrives at the model. The velocity needed for the Morison equation is the velocity at the model. To account for the difference in time, a time shift method is applied in this study. In Figure 27 the difference in time it takes for a wave to travel between the Ems and the model is schematized ($t_1 - t_2$).

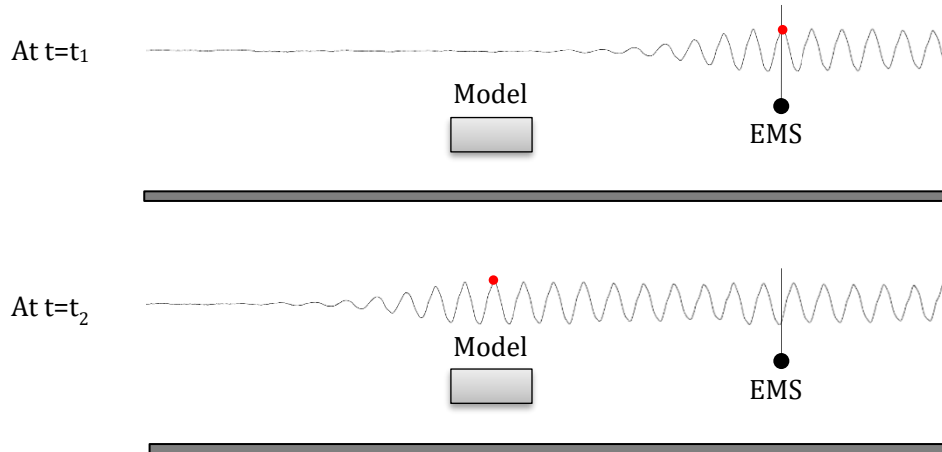


Figure 27: Example of a velocity time shift. At t_1 the red wave arrives at the EMS, at t_2 the wave arrives at the model centre of mass

The time shift method is based on the wave propagation speed. When knowing the spatial distance between two locations and the time it takes for a wave to travel between the two locations, the wave propagation speed can be determined.

For every wave that is analyzed in this study the wave propagation speed is determined from the measured wave gauge records. The spatial distance between wave gauge 1 and 4 is divided by the difference in time it takes a for a wave to arrive at wave gauge 4 after it arrived at wave gauge 1.

$$c_{wg} = \frac{\Delta_{WG \text{ spatial shift}}}{\Delta_{WG \text{ time shift}}}$$

Where:

c_{wg} :	The wave propagation speed determined from the wave gauges [m/s]
$\Delta_{WG \text{ spatial shift}}$:	The measured spatial distance between wave gauge 4 and 1 [m]
$\Delta_{WG \text{ time shift}}$:	The time it takes for wave to travel between wave gauge 4 and 1 [s]

The wave propagation speed is calculated for every test. This speed is then used to estimate the time shift, delay, between the velocity signal measured at the EMS and the velocity signal at the model position. The spatial distance between the model and the EMS is known, there is 3.0 m distance. The following formula is used to estimate the EMS time shift.

$$\Delta_{EMS \text{ time shift}} = \frac{\Delta_{EMS \text{ spatial shift}}}{c_{wg}}$$

Where:

c_{wg} :	The wave propagation speed determined from the wave gauges [m/s]
$\Delta_{EMS \text{ spatial shift}}$:	The measured spatial distance between the EMS and the model [m]
$\Delta_{EMS \text{ time shift}}$:	The time it takes for a wave to travel between the EMS and the model [s]

This calculated time-shift is transformed used to create an empty array with a time length equal to the calculated EMS time shift. The empty array is then added to the velocity signal to account for the delay between the EMS and the model.

The adjusted velocity record, where the depth and time shift have been applied, gives a new velocity called: $U_{wave,x}$. The same procedure is applied to find the vertical velocity $U_{wave,z}$.

Combined Wave and Current

Different procedures and variables can be chosen to compute the velocity for a combined wave-current environment. In previous studies with on the combined wave-current condition, for example by Venugopal (2008), a structure was towed through a wave field. To account for the combined wave-current velocity, the following expression was used:

Other studies

$$U_x = U_{c,x} + U_{wave,x}$$

Where:

$U_{c,x}$: The velocity with which the structure is towed [m/s]
 $U_{wave,x}$: The orbital water particle velocities determined from the undisturbed wave field with linear wave theory [m/s]

In the present study a similar expression is applied, only different definitions for the velocity components are used.

Present study

$$U_x = U_{c,x} + U_{wave,x}$$

Where:

$U_{c,x}$: The velocity measured in front of the model, by the EMS at 0.2 m depth [m/s]
 $U_{wave,x}$: The horizontal orbital water particle velocities determined by linear wave theory using the regular wave, undisturbed wave parameter values (T and H). [m/s]

For the vertical velocity, there is no vertical current component, so the total velocity is described by the wave component only:

$$U_z = U_{wave,z}$$

Where:

$U_{wave,x}$: The vertical orbital water particle velocities determined by linear wave theory using the regular wave, undisturbed wave parameter values (T and H). [m/s]

3.4.3. Computation of the Morison coefficients

To compute the Morison force coefficients from the fixed model test data, the least squared method is applied. This method defines the error between the predicted Morison force, from the measured water velocity and acceleration, and the measured force. This error squared and defined to be as small as possible by adjusting the force coefficients. This way the combination of force coefficients is found which results in the smallest error between the predicted Morison force and the measured force from the experiments. The method is applied separately for the horizontal and vertical direction, since separate coefficients and force are found for the two directions as well.

The equations used for the Least squared method in horizontal direction:

$$F_x = \frac{1}{2} \rho C_{Dx} D U_x \sqrt{U_x^2 + U_z^2} + \rho C_{Mx} A a_x \quad \rightarrow \quad f_{Dx} U_x \sqrt{U_x^2 + U_z^2} + f_{Mx} a_x$$

$$\varepsilon^2 = \sum [f_{Dx} U_x \sqrt{U_x^2 + U_z^2} + f_{Mx} a_x - F_{mx}]^2$$

$$\frac{\partial \varepsilon^2}{\partial f_{Dx}} = 0: \quad f_{Dx} \left(\sum U_x^2 (U_x^2 + U_z^2) \right) + f_{Mx} \left(\sum U_x \sqrt{U_x^2 + U_z^2} a_x \right) = \sum U_x \sqrt{U_x^2 + U_z^2} F_{mx}$$

$$\frac{\partial \varepsilon^2}{\partial f_{Mx}} = 0: \quad f_{Dx} \left(\sum U_x \sqrt{U_x^2 + U_z^2} a_x \right) + f_{Mx} \left(\sum a_x^2 \right) = \sum a_x F_{mx}$$

Solving these two equations, gives the horizontal drag and inertia coefficients in horizontal direction.

Where:

- ε : The error between the Morison force and the measured force [N/m]
- ρ : The density of the fluid [kg/m³]
- A : The frontal area of the cylinder [m²]
- D : The cylinder dimension, in vertical direction [m]
- B : The cylinder dimension, in horizontal direction [m]
- C_{Dx} : The drag coefficient in horizontal direction [-]
- C_{Mx} : The inertia coefficient in horizontal direction [-]
- a_x : The water particle acceleration in horizontal direction [-]
- U_x : The water particle velocity in horizontal direction [-]
- U_z : The water particle velocity in vertical direction [-]

The equations used for the Least squared method in vertical direction:

$$F_z = \frac{1}{2} \rho C_{Dz} B U_z \sqrt{U_x^2 + U_z^2} + \rho C_{Mz} A a_z \quad \rightarrow \quad f_{Dz} U_z \sqrt{U_x^2 + U_z^2} + f_{Mz} a_z$$

$$\varepsilon^2 = \sum [f_{Dz} U_z \sqrt{U_x^2 + U_z^2} + f_{Mz} a_z - F_{mz}]^2$$

$$\frac{\partial \varepsilon^2}{\partial f_{Dz}} = 0: \quad f_{Dz} \left(\sum U_z^2 (U_x^2 + U_z^2) \right) + f_{Mz} \left(\sum U_z \sqrt{U_x^2 + U_z^2} a_z \right) = \sum U_z \sqrt{U_x^2 + U_z^2} F_{mz}$$

$$\frac{\partial \varepsilon^2}{\partial f_{Mz}} = 0: \quad f_{Dz} \left(\sum U_z \sqrt{U_x^2 + U_z^2} a_z \right) + f_{Mz} \left(\sum a_z^2 \right) = \sum a_z F_{mz}$$

Solving these two equations, gives the vertical drag and inertia coefficients in vertical direction

Where:

- ε : The error between the Morison force and the measured force [N/m]
- ρ : The density of the fluid [kg/m³]
- A : The frontal area of the cylinder [m²]
- D : The cylinder dimension, in vertical direction [m]
- B : The cylinder dimension, in horizontal direction [m]
- C_{Dz} : The drag coefficient in vertical direction [-]
- C_{Mz} : The inertia coefficient in vertical direction [-]
- a_z : The water particle acceleration in vertical direction [-]
- U_x : The water particle velocity in horizontal direction [-]
- U_z : The water particle velocity in vertical direction [-]

3.4.4. Force Prediction Procedure

For the answering of the research questions a forces prediction is performed for both the fixed model and the tether model. The procedure for deriving the default force coefficients and using them to predict the hydrodynamic forces on the fixed model and the tether force in the tether model is shown in Figure 28.

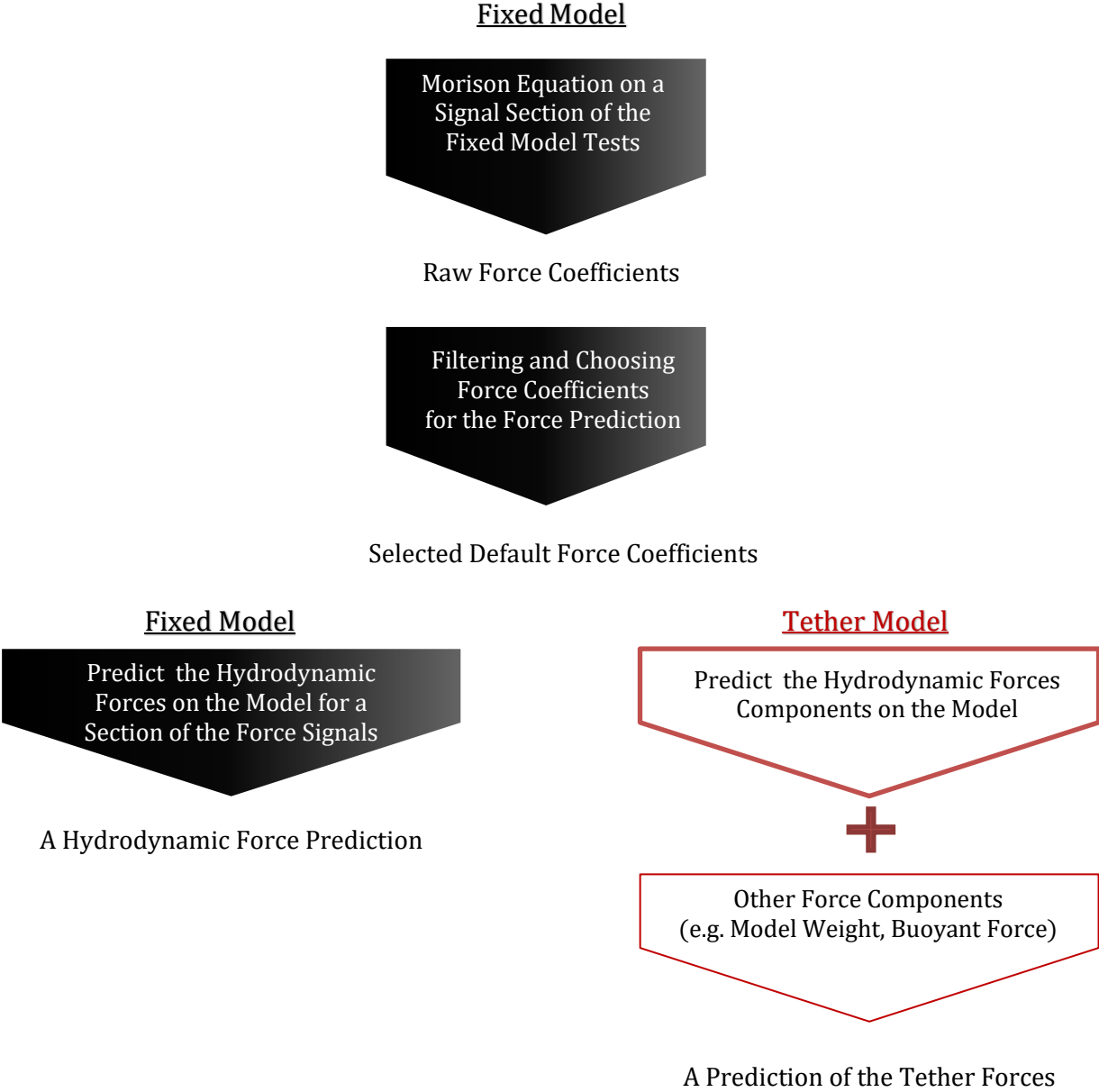


Figure 28: A schematisation of the force prediction for the fixed model and tether model.

4

Results and Analysis

This chapter presents the results from the physical model tests performed in the wave-current flume. First the results from the test are presented, after which they will be analysed. The order in which the results and analysis are presented, is the order of the research questions formulated in chapter 1.3. This leads to the following composition of this chapter:

4.1. The Relationship Between Environmental Conditions and Hydrodynamic Forces

Showing the time series of the fixed model tests and analysing the relationship between wave and/or current conditions and the hydrodynamic force on the model.

4.2 Force Prediction by Morison

Analysing the Morison drag and inertia coefficients for the different wave and/or current conditions found for the fixed model test. Values for the coefficients are chosen to predict the hydrodynamic forces. The paragraph is finalized by comparing and analysing the predicted hydrodynamic force to the measured hydrodynamic force.

4.3. The Dynamic Response to Environmental Conditions

Presenting the relationships found for the tether model, between kinematic parameters and the different wave and/or current conditions. Doing some preliminary analyses on composition of the dynamic force.

4.1. The Relationship Between Environmental Conditions and Hydrodynamic Forces

This paragraph focuses on the results from the fixed model tests. By analysing the processed data from the physical model tests, the following research question will be answered in this paragraph:

Research Question 1a

What is the relationship between the environmental parameters; wave height, the wave period, current velocity and submergence depth, and the hydrodynamic forces on a fixed rectangular cylinder in small-scale flume experiments subjected to a regular wave, current and combined wave-current conditions?

4.1.1. Experiment Observations

This section contains the observation of the output signals from the fixed model tests. Signal features are pointed out and discussed.

First of all, the wave gauge signals from two regular wave tests are shown in Figure 29. In red, features are marked and number. On the page and the page these will be discussed.

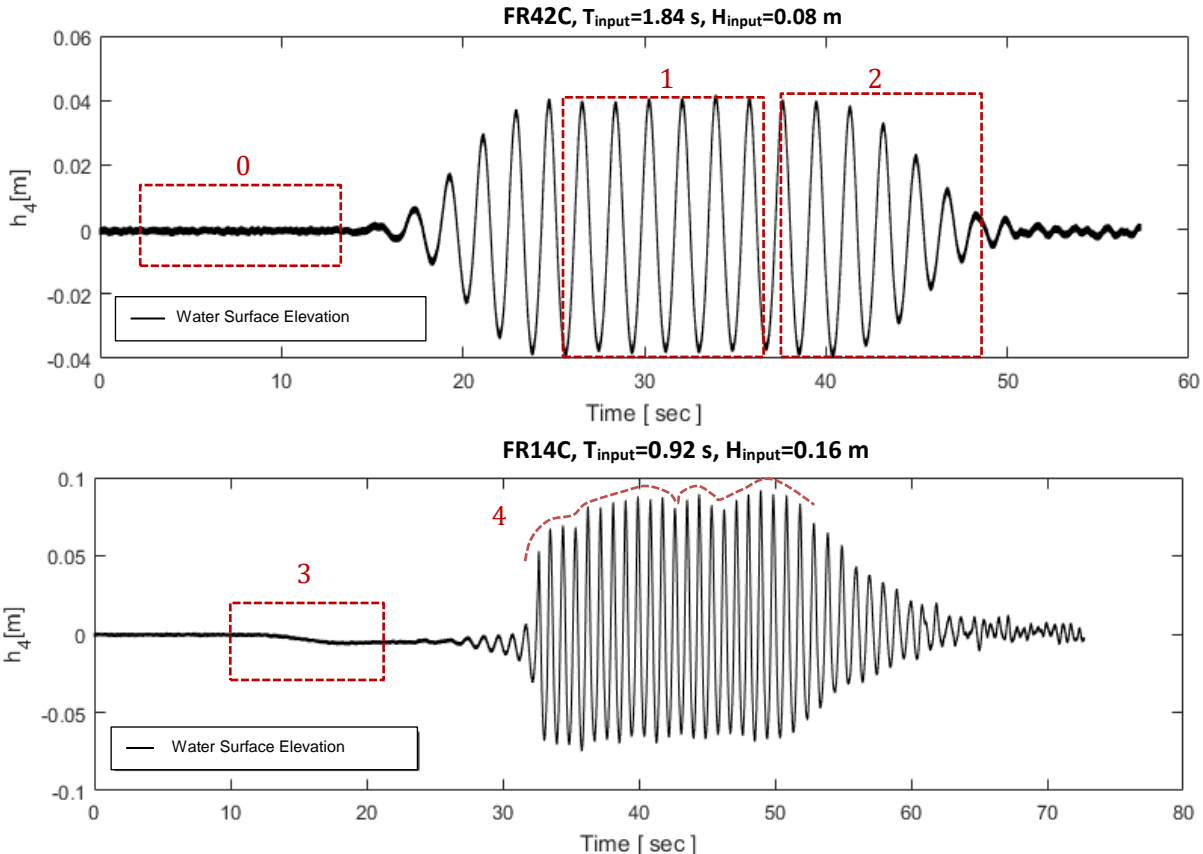


Figure 29: The water surface elevation signals from wave gauge 4 for 2 different tests: a long wave, and a short wave..

Long wave, FR42C

- [0] For all three graphs, this part of the signal depict the water surface before the waves arrive at the model.
- [1] In the top panel a long waves is shown. The waves of this long wave are a nice harmonic waves with of an approximately the same amplitudes. In contrast, the short wave in the middle panel shows less constant amplitudes [4] in the wave signal. An explanation is given at [4].
- [2] This part of the signal show the waves after the wave generator if switched off. As the wave paddle slows down it's movement the wave amplitude decreases until they have completely vanished.

Short wave, FRC14C

- [3] In some of the signal from the experiments this decrease in water level is noticed. This is created when the wave gauge is switched on and makes a sudden move towards it's active position. If the active position is to the front of the flume, the water level decreases a little, as is seen in this signal.
- [4] The signal in the middle panel is a short wave. Compared to the signal of the long wave [1] , this wave is a less constant harmonic. As the wave length of a short wave is smaller, the wave motion is more affected by the presence of the model. Disturbances reflect back from the model interfering with the incoming waves resulting in a fluctuating amplitude of the wave.

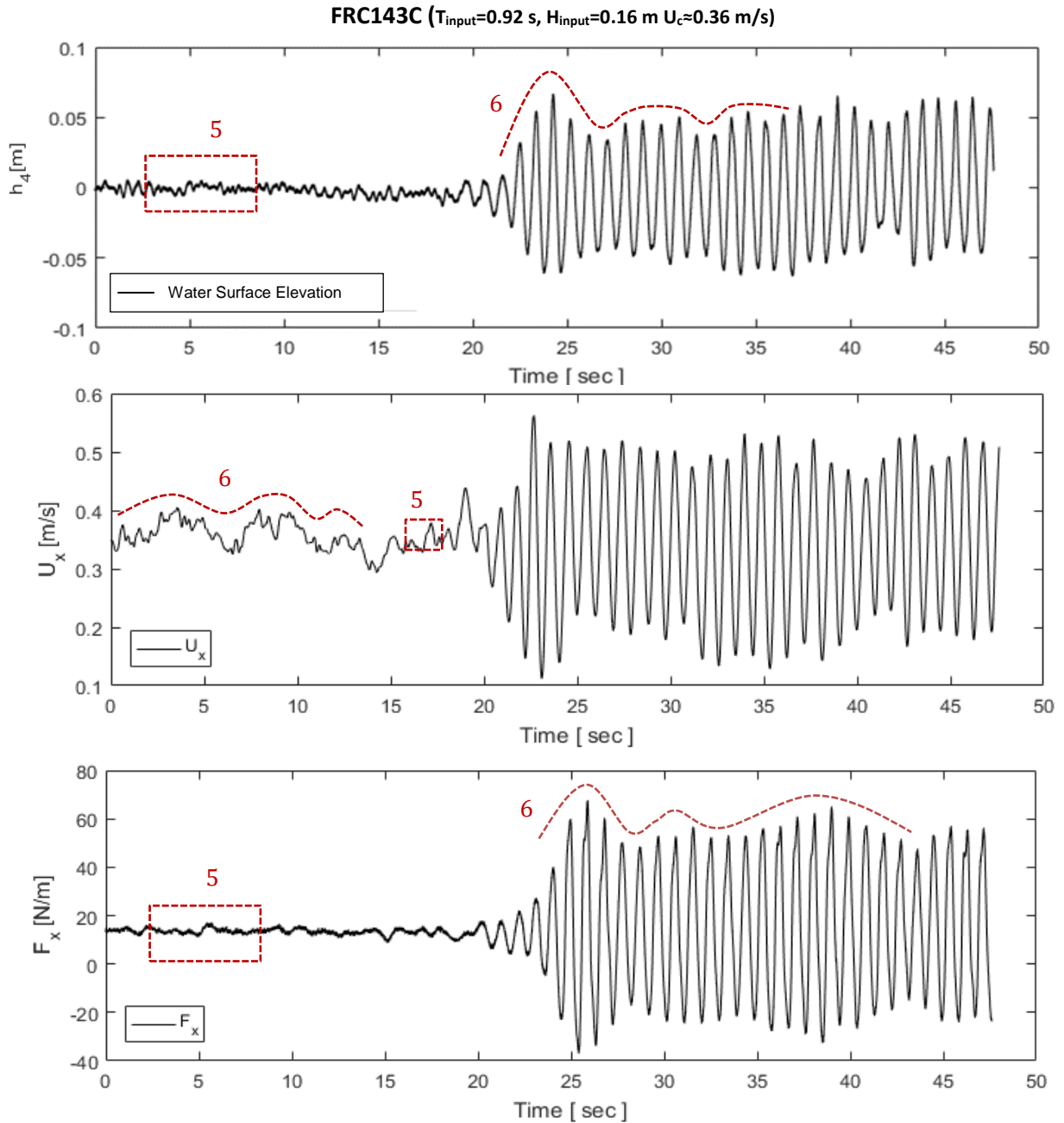


Figure 30: The water surface elevation (top), horizontal velocity (middle) and horizontal force (bottom) signals for a short wave with current (FRC143C)

In Figure 30, some signal features are shown in the signals from the water surface elevation and the horizontal water particle velocities measured by the EMS at 0.2 m water depth.

Short wave + current, FRC143C

[5] In the beginning part of all 3 signals, turbulences in the flow are seen. The mean and standard deviations of these velocity of only current tests are shown in Table 11. The maximum standard deviation for all only current tests is about 5%.

Table 10: For only current condition: the mean and standard deviation of horizontal velocities, in the first two columns, and the maximum and minimum recorded velocities in the last two columns

\bar{U}_x	U_x		$U_{x,max}$	$U_{x,min}$
Mean Velocity	Standard Deviation		Max. Velocity	Min Velocity
[m/s]	[m/s]		[m/s]	[m/s]
0,129	0,0057	4%	0,140	0,108
0,231	0,0127	5%	0,259	0,200
0,373	0,0181	5%	0,414	0,328

[6] Another type of disturbance with smaller frequency than the turbulences is seen in the 3 signals. This almost wavy-like motion is caused by the non-smooth inflow of the current into the flume. As seen in Figure 15, the current flows into the flume vertically right into the wave field (if present), after which the flow has to turn and flow horizontally. The larger the current velocity, the larger these 'wavy' patterns are in velocity amplitude. This explains why in Table 11, the standard deviation of the velocity increases for a larger current velocity.

The last two features to be studied, can be seen best in the force signals of regular waves, see Figure 31 and Figure 31.

Short wave, FR14C

[7] When a measurement record is long enough the waves reflected from the back of the flume can be distinguished. This is mainly seen in the force signals. In the signals in front of the model the reflection is less clear, because part of the reflected signal is blocked by the model and again reflected back to the end of the flume.

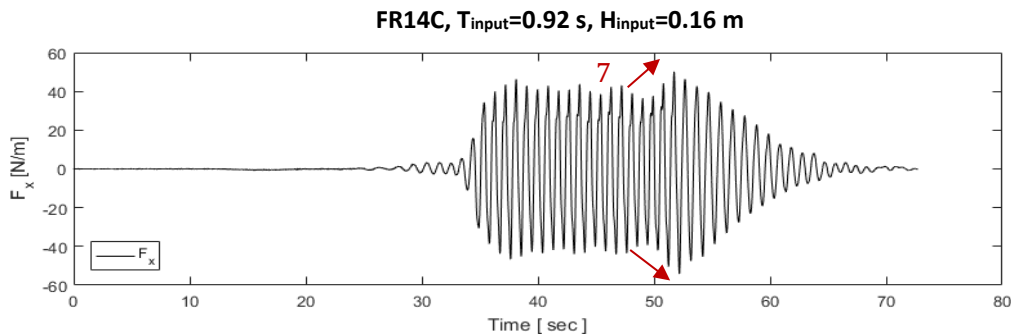


Figure 31: End of flume resonance in the signal of the horizontal force for a regular wave (FR14C)

Short Wave, FR14C, and long wave, FR42C

[8] A clear 'shoulder' is seen in the force signals of a short wave. This is due to the previously mentioned at [4], the larger relative model dimension to the wave length.

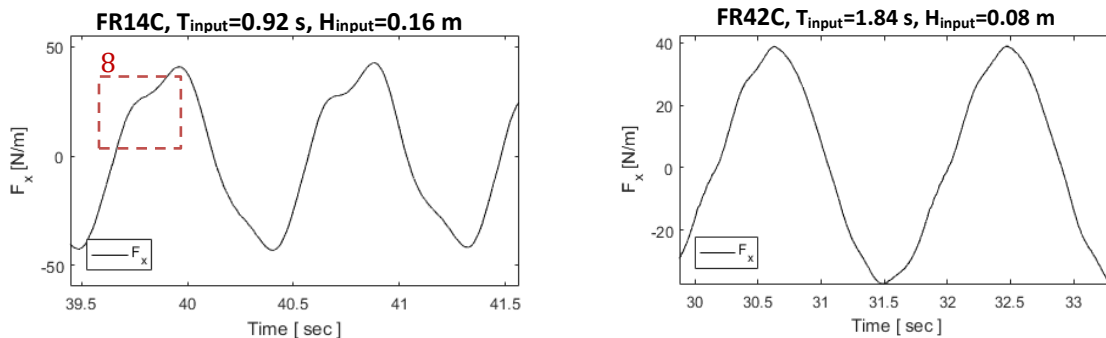


Figure 32: Close up horizontal force signals for a short (FR14C) and long wave (FR42C)

4.1.2. Wave-Current Effects

In this section the effect combining waves and current is studied. Also, the method for computing the combined wave-current velocities from section 3.4.2 is reviewed.

I. Wave-Current Signals

First, briefly an example is shown of an only current, regular wave and combined wave-current condition. In Figure 33, for these three conditions parts of the horizontal water velocity measurements of at EMS depth and the horizontal force measurement is presented.

A brief evaluation of the first column for the velocities show that roughly the velocity magnitudes found for the only current (≈ 0.3 m/s) and only wave condition (≈ 0.17 m/s) add up to the velocities found for the combined wave-current condition (≈ 0.45 m/s).

For the horizontal force, the same is found. The only current force magnitude (≈ 14 N/m) and the regular wave mean magnitude of the peaks (≈ 38 N/m), roughly add up to the peak magnitudes for the combined situation (≈ 54 N/m).

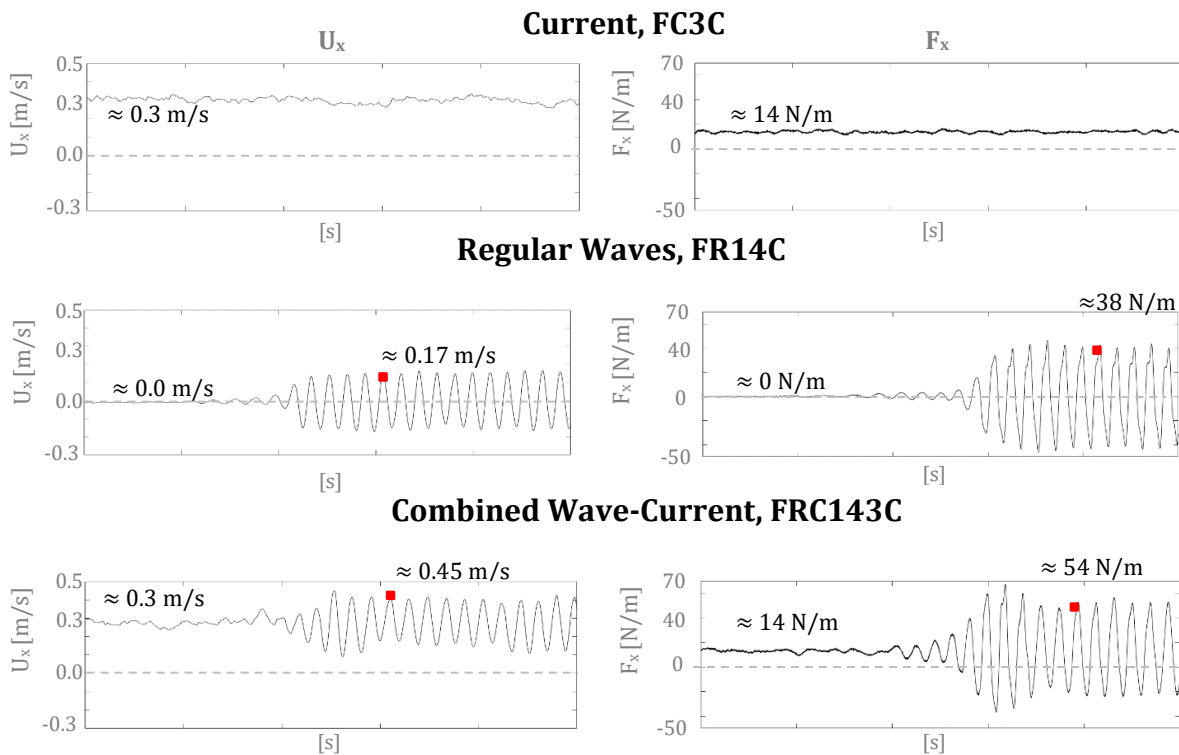


Figure 33: The non-adjusted EMS horizontal particle velocity signals and the horizontal force signals for three conditions: current ($U_c=0.3$ m/s, $H=0$ m, $T=0$ s), regular waves ($U_c=0$ m/s, $H_{input}=0.16$ m, $T_{input}=0.92$ s), and combined wave-current ($U_c=0.3$ m/s, $H_{input}=0.16$ m, $T_{input}=0.92$ s).

These 6 graphs were shown to give an indication of what the signals of separate environmental conditions look like relatively to the signals for a combined wave-current situation. The next sections go more in depth on the effect of the different components in a combined field, and how the components effect each other.

II. Current effects on Wave Parameters

In chapter 3, section 3.4.2, was described how the raw velocity measurements were translated into representative water particle velocities of interest at the location of the model. The procedure described how in case of a combined wave-current situation, the velocity component was measured and added to the wave component which was determined by linear wave theory expressions. To illustrate, the expression for the horizontal water velocity is repeated:

$$U_x = U_{c,x} + U_{wave,x}$$

Where:

- $U_{c,x}$: The velocity measured in front of the model, by the EMS at 0.2 m depth [m/s]
 $U_{wave,x}$: The horizontal orbital water particle velocities determined by linear wave theory using the regular wave, undisturbed wave parameter values (T and H). [m/s]

For the computation of the water particle orbital velocities the input values for the wave parameters are used. To study the influence of a coexisting current on the wave parameters, the input and measured wave parameters H and T are presented in Figure 34. From the left figure it can be seen that the wave height found for regular waves only is very close to the wave height that was sent to the wave maker to generate. It can also be seen that for an increase of the added current in case of a combined current environment, the measured wave height starts to show an increased deviation from the input wave height, to a maximum deviation of 45%. The right graph shows that the influence of the incoming current on the wave period is of much less significance. So the influence of a coexisting current velocity is significantly larger on the wave height than on the wave period.

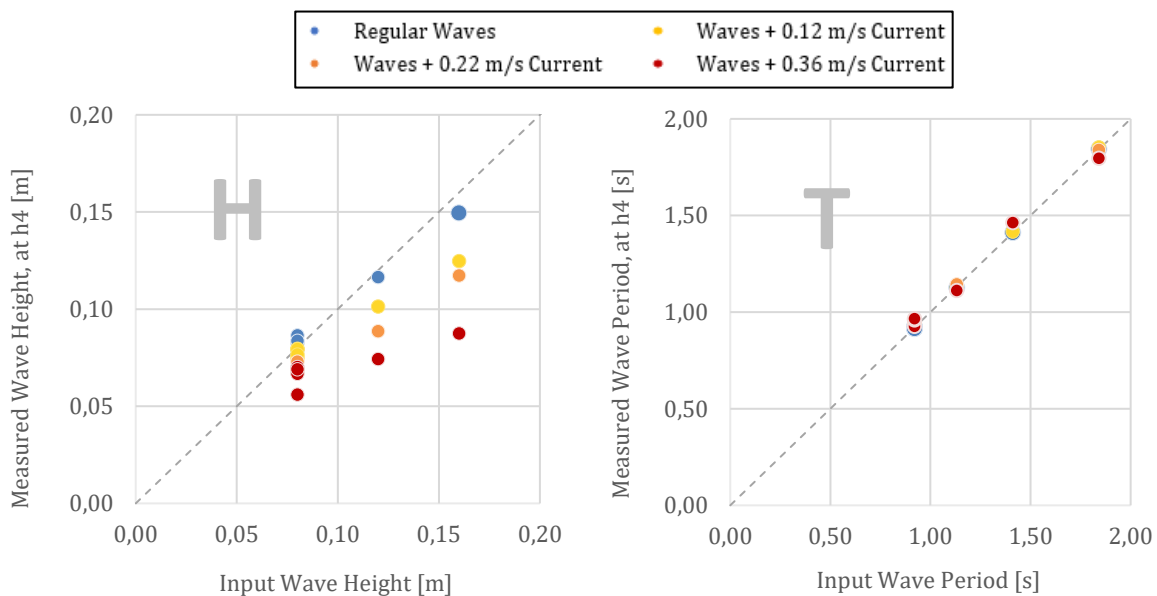


Figure 34: the influence of a co-existing current on the wave parameters wave height (left) and wave period (right)

To get a better understanding on the effect of a coexisting current in the wave height found in a water level elevation signal from the wave gauges, a frequency analysis is performed on the next pages. First the only wave condition will be studied after which the combined wave-current is analysed.

Frequency Graphs of Long and Short Waves

Figure 35, goes more in depth on the wave height signals between a short (FR14C) and long wave (FR42C). The Matlab CWT (continuous wavelet transform) graphs show the frequencies found in the water surface elevation signals. For both wave types, the bottom yellow frequency band, is the wave frequency. For the short wave a second frequency band is seen at a higher frequency. For the long wave, a second band is found as well, but is less clear. The higher order bands are due to the earlier mentioned reflection from the model, which was more significant for short waves.

The signals underneath the CWT graphs, show the signals filtered for only the wave frequency, the short wave FR14C is filtered for 0.7-1.28 Hz and long wave FR42C for 0.45-0.7 Hz. For the wave height of the short wave FR14C an error of a few centimetres (≈ 0.02 m) is found between the measured and filtered signal peaks. Following the blue dashed line, representing the input wave amplitude, it is seen that the filtered wave signal underestimates the input wave height by a few centimetres.

For the long wave FR42C, a different result is found. The error between the peaks of the long wave FR42C is smaller, only a few millimetres. In addition, the measured wave height is equal to the input wave height (blue dashed line).

To conclude, for the short wave a non-wave frequency band is of significance, together with the incoming wave adding up to the input wave height. While for the long wave, the wave frequency fully represent the water surface signal, and results in a wave height equal to the input wave height.

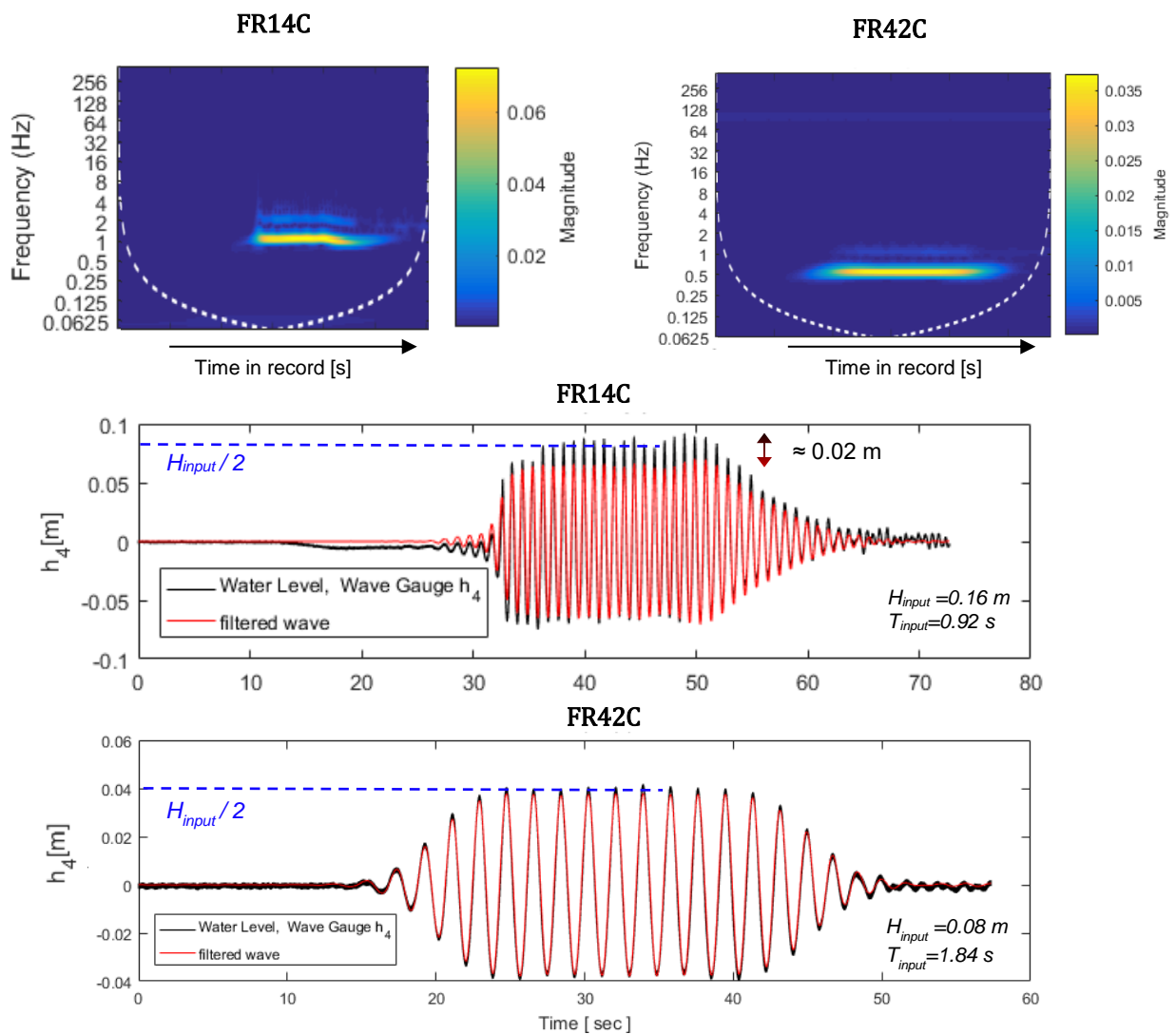


Figure 35: CWT and Filtered wave signals. Short wave FR14C filtered for 0.7-1.28 Hz and long wave FR42C for 0.45-0.7 Hz. Blue dashed line indicates the input wave amplitude ($H_{input}/2$)

Frequencies Short Waves With Current

Figure 36, shows the same short wave as in Figure 35 only now in a combined wave-current condition with a $U_c \approx 0.36$ m/s current. From the top CWT graph, 3 frequency ranges can be distinguished from the water surface record. The first box [1] shows that the current causes some disturbances at a higher frequency, before the wave arrives. When the wave arrives in box [2] a clear yellow band is seen at the wave frequency. Box [3] shows that still disturbances are shown at a higher frequency. The disturbances have become brighter in colour, indicating that the magnitude of the disturbances at a higher frequency have increased due to the presence of the wave. It is however noted that compared to the only wave condition with FR14C in Figure 35, the clear higher frequency band that was seen there, has vanished. For the situation combined with current, there is no longer a band-like higher frequency but more a 'cloudy' -like region in box [3].

The middle panel shows the same CWT graph as in the top panel, only zoomed in closer to the wave frequency band. From this CWT graph the wave frequency band is estimated to range from approximately 0.8 Hz to 1.27 Hz. The bottom panel shows that this filtered signal gives a good estimate of the water surface elevation, especially at the section of interest. Compared to the same wave without a current component, FR14C in Figure 35. The wave frequency estimates the water level better. However, compared to the input wave height/amplitude (blue dashed line) the wave is smaller than for FR14C only.

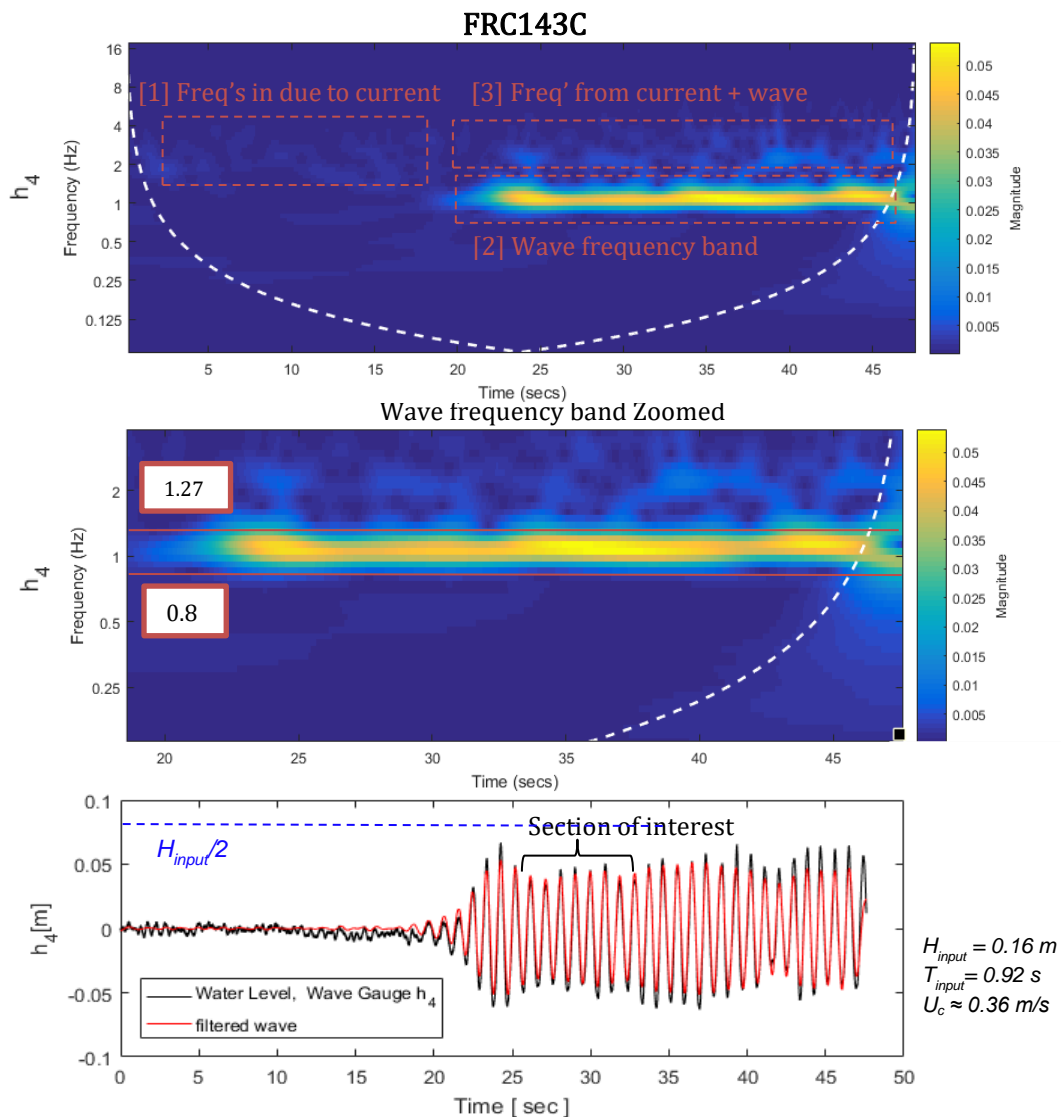


Figure 36: CWT and Filtered wave signals. Short wave FR14C filtered for 0.7-1.28 Hz. Blue dashed line indicates the input wave amplitude ($H_{input}/2$)

By comparing the frequency bands for regular waves, in Figure 35, to what was found in the frequency bands, in Figure 36, for the same wave but combined with a current, the following is concluded:

For a only short wave condition, the incoming regular wave (in red) alone does not result in a wave height equal to the input wave height, the wave height given to the wave generator (blue dashed lines). Because of high order frequencies, caused by reflection from the model, the wave height increases to a magnitude more or less equal to the input wave height.

Regular (short) wave condition: $H_{input} = H_{incoming\ wave} + H_{reflected}$

Regular (long) wave condition: $H_{input} \approx H_{incoming\ wave}$

For a (short) wave-current condition, the high order band from reflection of the model seems to have disappeared due to the current. Therefore, the wave signal is estimated better by the wave frequency band only than it was for a regular wave condition. However some higher order frequencies are still present due to fluctuations from the current. As for a regular wave, the water elevations due to the incoming wave alone are not equal to the input wave height. With the reflection component gone, the wave height is smaller than the input wave height.

(short) Wave-current condition: $H_{input} > H_{incoming\ wave} + H_{reflected}$

(long) Wave-current condition: $H_{input} > \approx H_{incoming\ wave}$

An example of a wave-current condition with a longer wave is given in Figure 37. It shows that the wave amplitude of the incoming wave is reduced to to the presence of a current.

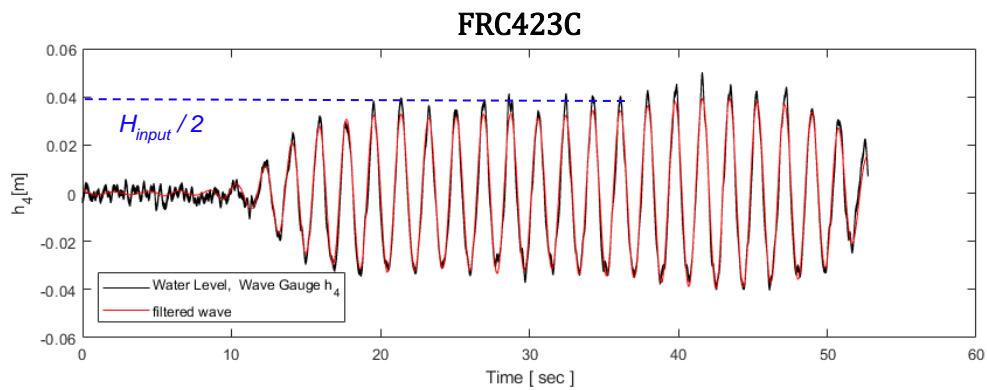


Figure 37: A filtered water surface elevation signal for a long wave combined with current, FRC423C.

III. Current effect on Water Particle Velocities

Next, the influence of an increasing added current component is studied in Figure 38. The graphs (1) and (3) of Figure 38 compare the absolute measured velocity amplitude U_x and U_z at 0.2 m to what the computed velocity magnitude gives at the same depth of 0.2 m. The graphs in the right column show the same, only now for just the wave component in the velocity, $U_{wave,x}$ and $U_{wave,z}$.

In graph (1) shows that the error between the measured and computed total horizontal water particle velocity U_x remains within the 15% error band. The mean error of these tests -2% with a standard deviation of the error of 6%. The largest error comes from the shortest wave tests, with wave ID R14. Graph (2) indicates that the largest errors are found in these short waves, because of the errors in the wave component, $U_{wave,x}$, of the velocity signal. This is due to a combination of two reasons. First of all, on the previous page was discussed how especially for short waves the measured wave height ($H_{reduced}$) is smaller than the input wave height (H_{input}). Second, for short waves the water particle velocities are least well determined by linear wave theory, because they are 3rd to 4th order Stokes waves. For a only wave condition, Stokes waves give smaller wave amplitudes than linear waves.

1. For all waves: $U_{computed,wave,x}(H_{input}) > U_{measured,wave,x}(H_{reduced})$
2. For short waves: $U_{wave,x,stokes} < U_{computed,wave,x,linear\ wave}$

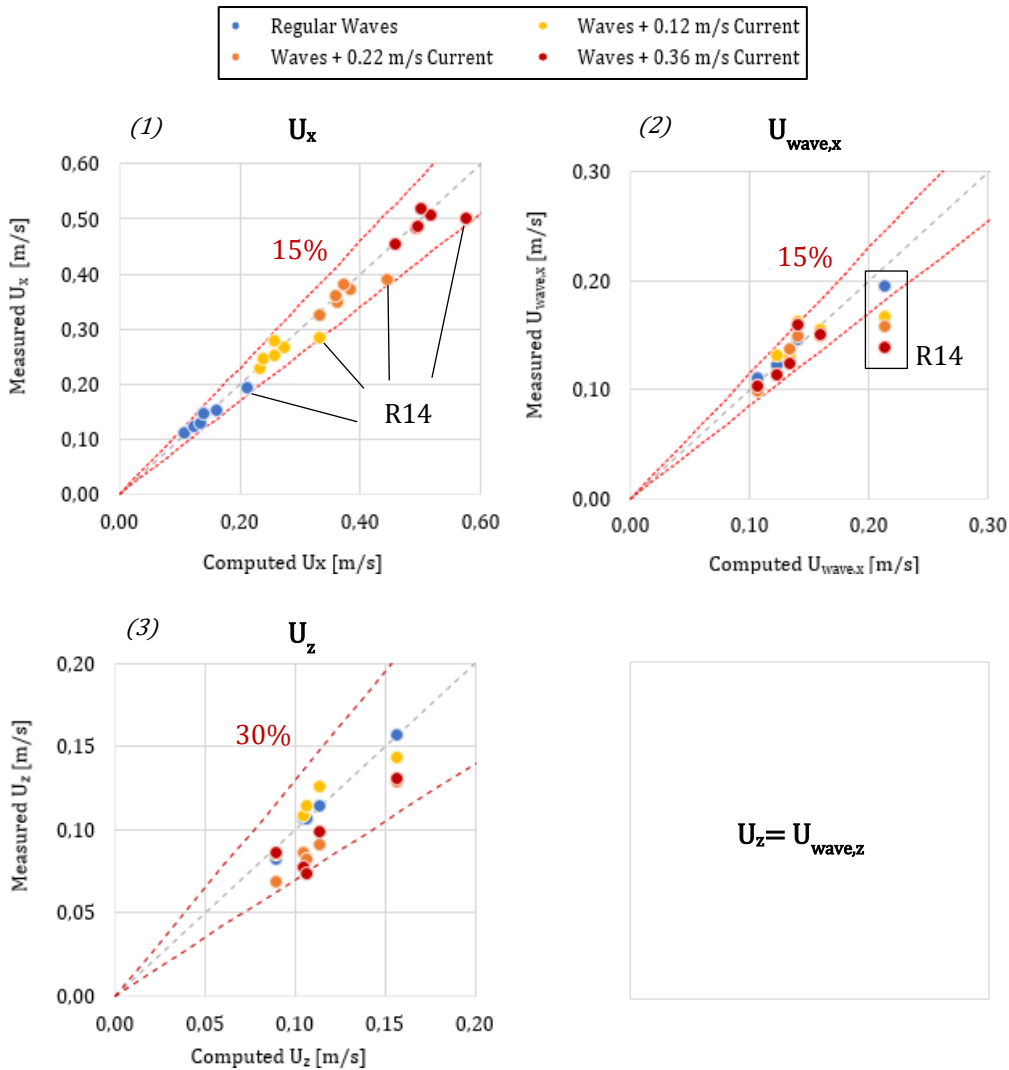


Figure 38: For 0.2 m depth the computed and measured total water particle velocities U_x and U_z and the wave component of the horizontal water particle velocity $U_{wave,x}$. Red dashes lines: error bands.

In graph (3) of Figure 38 the water particle velocities of the vertical direction are plotted. The errors reach up to larger values, of 30%, much higher than for the horizontal water particle velocities. The larger the current component (the more red the marker) the larger the error. The vertical velocities were defined as follows:

$$U_z = \overline{U_{\epsilon,z}} + U_{wave,z}$$

Where:

- U_z : The computed vertical water particle velocities [m/s]
- $U_{wave,z}$: The vertical orbital water particle velocities determined by linear wave theory using the regular wave, undisturbed wave parameter values (T and H). [m/s]

The errors for the vertical water particle velocities are much larger than for the horizontal water particle velocities. This is because of an increased unsteadiness in the inflow current. The expression of the computed vertical velocities works best for small (uniform steady) currents. When the current is large the flow is not steady anymore. This is discussed in CH5 more in depth,

4.1.2. The Relationships

This section discusses the relationship between various environmental conditions and the measured hydrodynamic forces on the fixed model. In this section, the velocity is the adjusted velocity described in section 3.4.2.

Current

The first environmental condition to be studied in relationship with the hydrodynamic force, is the only current condition. Figure 39, shows the results from the test with a 2nd order polynomial trend line running through the data points and intercepting at zero. The results show the expected relationship of the hydrodynamic force with the velocity squared.

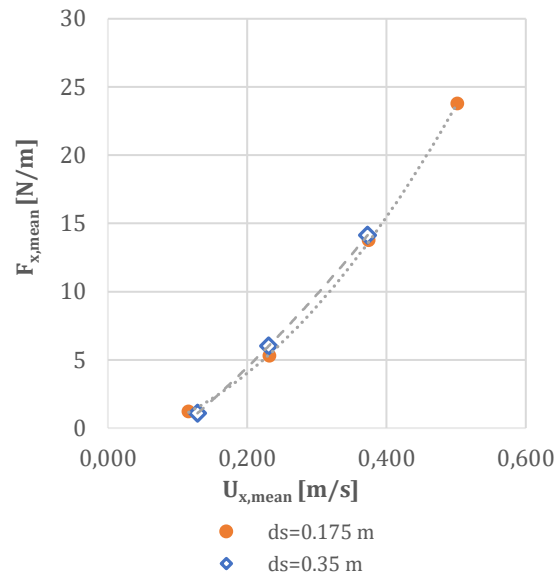


Figure 39: The mean horizontal hydrodynamic force for different current velocities

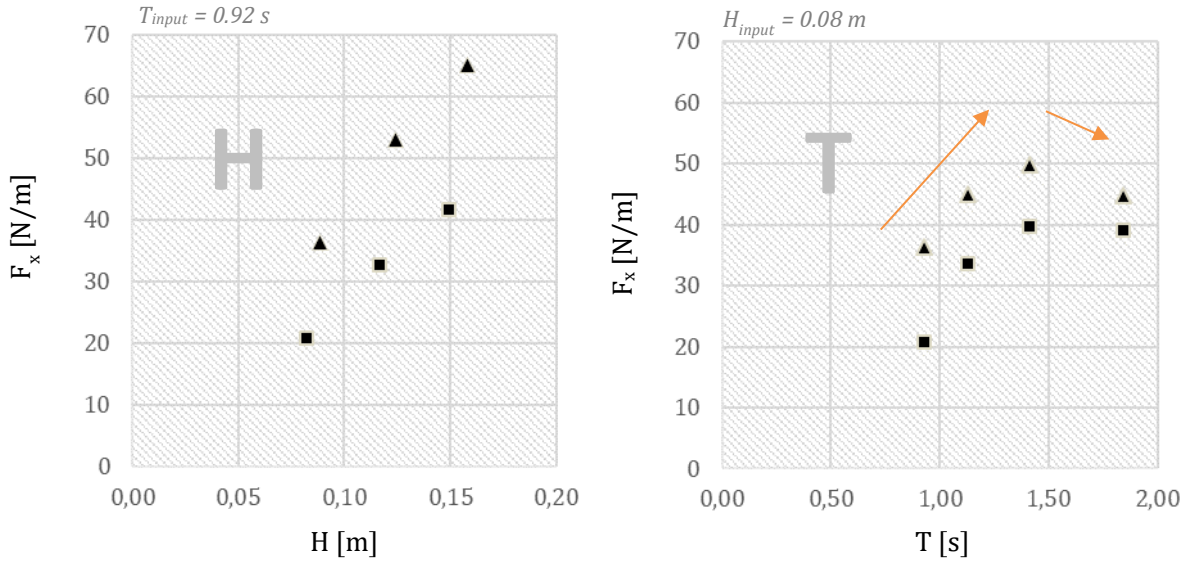
The graph includes the two submergence depths, 0.175 m and 0.35 m. From this data-set no clear influence of the submergence depth on the relationship between the hydrodynamic force and the mean water velocity can be seen. This emphasizes the assumption made in section 0. that the magnitude of the velocity is uniformly distributed over the depth in the range of submergence depths tested in this study.

Regular waves

The following environmental condition to be studied is regular waves. For the horizontal and vertical direction Figure 40 shows the relationship between the measured hydrodynamic force and the wave height and wave period. From all graph it can be seen that a larger submergence depth gives a larger hydrodynamic force magnitude.

First of all, the shapes of the relationships are studied. For both force direction a linear relationship is found between the force and the wave height. For the wave period a curved shape is found in the relationship to the hydrodynamic forces. Where these curves come from is explained underneath Figure 40.

Horizontal



Vertical

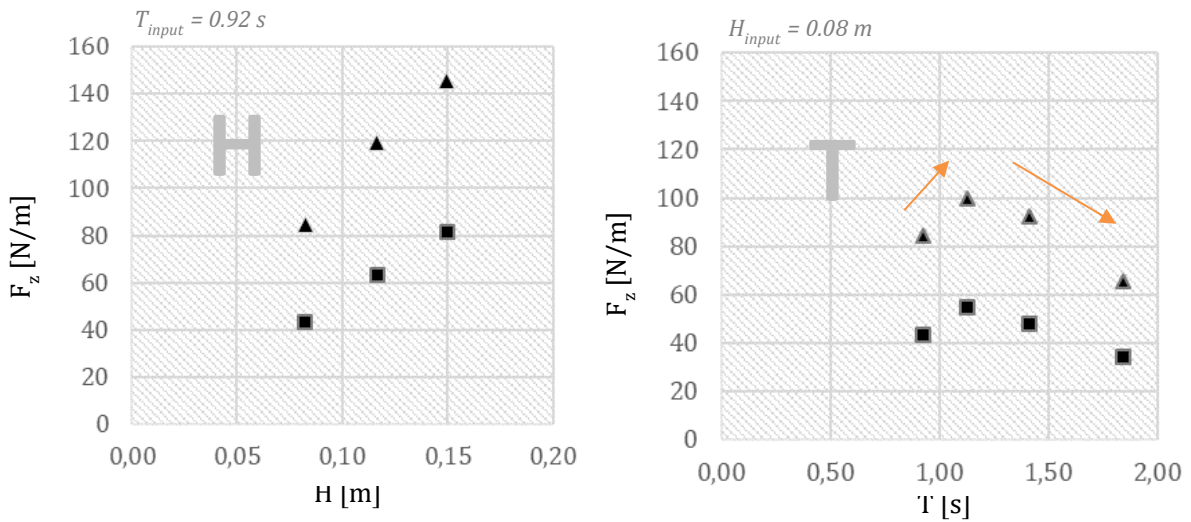


Figure 40: For both force directions: the relationship between the hydrodynamic force and the wave period (left column), and the hydrodynamic force and the wave period (right column).

To better understand the influence of the wave parameters, first the expression for the Morison Force is repeated. For a description of the variables, see section 3.4.3.

$$F_x = \frac{1}{2} \rho C_{Dx} D U_x \sqrt{U_x^2 + U_z^2} + \rho C_{Mx} A a_x$$

$$F_z = \frac{1}{2} \rho C_{Dz} B U_z \sqrt{U_x^2 + U_z^2} + \rho C_{Mz} A a_z$$

The KC numbers of the tests in the present study for regular waves are small, often no larger than 1. This indicates inertia dominance. Therefore, the first force component, the drag component, is removed from the force expressions for both directions, for the analysis on the relationship to the wave parameters. In chapter 4.2, KC-numbers, inertia forces and drag forces are discussed in depth.

In the rest of this section the remaining expression for the force is used for analysis.

$$F_i = F_{M,i} = \rho A C_{M,i} a_i$$

Where:

- F_i : The Hydrodynamic force in i -direction [N/m]
- $F_{m,i}$: The inertia force component in i -direction [N/m]
- ρ : Fluid density [kg/m³]
- A : Frontal area of the model [m²]
- $C_{M,i}$: The inertia coefficient in i -direction [-]
- a_i : The acceleration of the water particle motion in i -direction [m/s²]

This expression shows that the hydrodynamic forces among others is determined by the acceleration of the water particle motion. From linear wave theory the water particle acceleration can be derived from the water particle velocity by differentiating once. The following expressions are used and found for respectively the horizontal velocity and accelerations:

$$u_x = \hat{u}_x \sin(\omega t) \quad \text{with} \quad \hat{u}_x = \frac{\omega H \cosh[k(d+z)]}{2 \sinh(kd)}$$

$$\dot{u}_x = \hat{u}_x \omega \cos(\omega t) \quad \text{giving} \quad \hat{\dot{u}}_x = \frac{\omega^2 H \cosh[k(d+z)]}{2 \sinh(kd)}$$

In a similar way an expression can found for the vertical accelerations. Definitions of the variables in this expression are given in CH2, section 2.1.2. The accelerations are plotted in Figure 41.

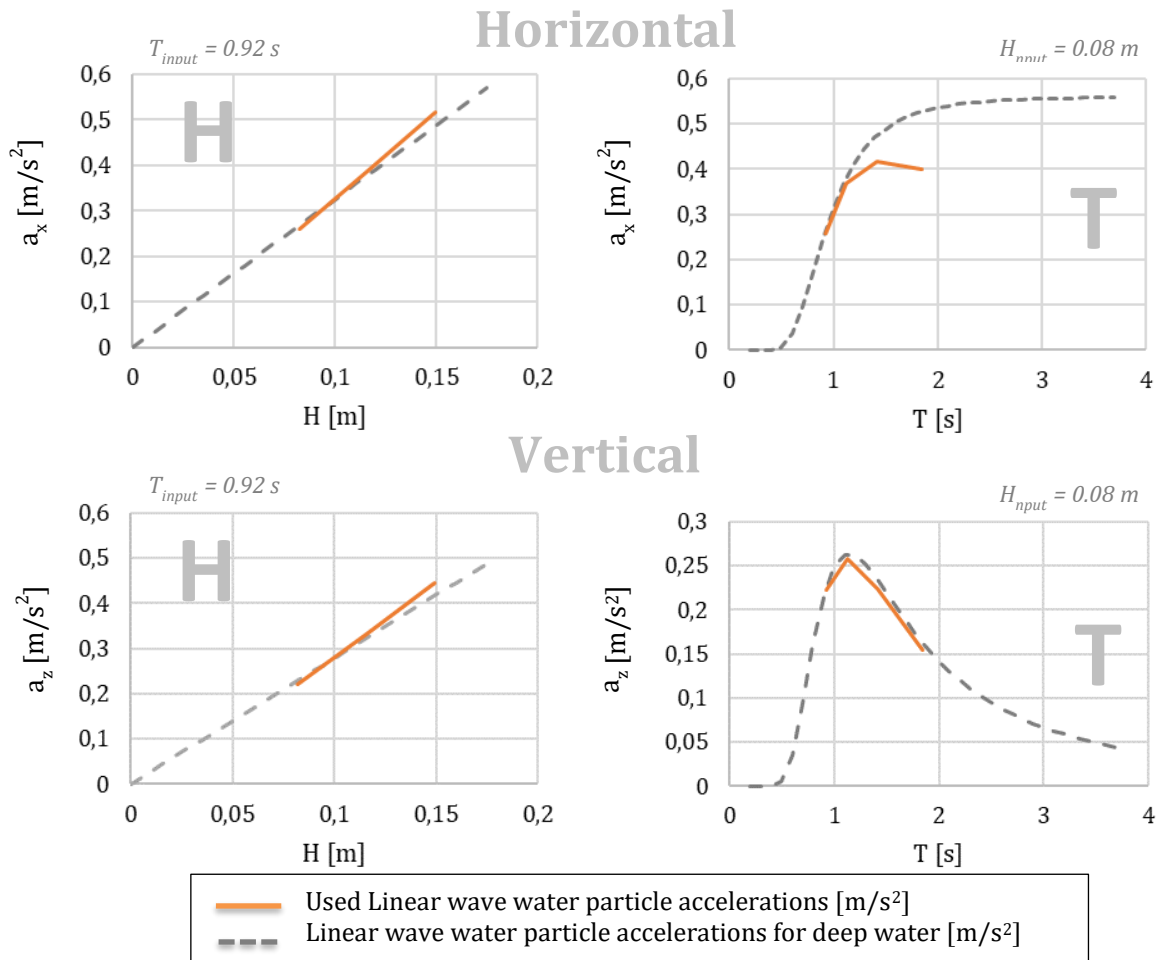


Figure 41: Example of an estimation of the water particle accelerations for a varying wave height for $T \approx 0.92$ s (left column) and wave period (right column). For $H \approx 0.08$ m and $d \approx 0.35$ m. Orange are the used accelerations, grey dashed line are deep water acceleration trends.

Comparing the shape of the relationships found in Figure 40 and Figure 41, shows that the relationship of the forces to the wave parameters is really determined by the accelerations. However, studying the magnitudes of the acceleration and the magnitudes of the hydrodynamic forces, it is seen that the largest acceleration does not necessarily imply the largest force. Looking at the expression for the force on the previous page, it is understood that this is due to the inertia coefficient. As the density, ρ , and the area, A , remain constant in the tests of this study, it is the product of the accelerations and the inertia coefficient that determines the magnitude of the force. The magnitude of the inertia coefficients is studied in the coming sections of section 4.2 on the Morison Force.

Combined Wave-current

The results from the combined wave-current conditions are shown and discussed in this section.

Figure 42, shows the horizontal hydrodynamic force for an increasing wave height in the left graph and for an increasing wave period in the right graph. Starting with the wave height, the earlier mentioned influence of the added current on the reduction of the wave can be seen. Except for the points corresponding to the ‘Wave + 0.36 m/s Current’ series, all wave-current combined situations show the similar linear relationship as is seen as for only waves. The graph also shows a linear increase in the force for an increasing coexisting current velocity component, for all series. For the combined wave-current tests the KC number still lays within the inertia dominated region, so the Inertia force component, still has the capacity to describe the force. The acceleration between the series remains the same since a constant current velocity does not influence the acceleration. So the increase in the forces for larger added currents, does not come from the inertia part but from a velocity related drag part, that has to contribute to the force to take account for the non-zero force base line. To conclude, the following has been found:

For an increasing coexisting current velocity:

- The relationship between the wave height and horizontal hydrodynamic force remains linear, because the inertia component remains dominant.
- The magnitude of the wave height decreases for the same input wave height.
- For the same wave height, the magnitude of the horizontal hydrodynamic force increases because the velocity increases which causes the drag to be of more significance. The velocity related drag part has to deliver a larger contribution to account for the increasing non-zero force baseline in the horizontal force.

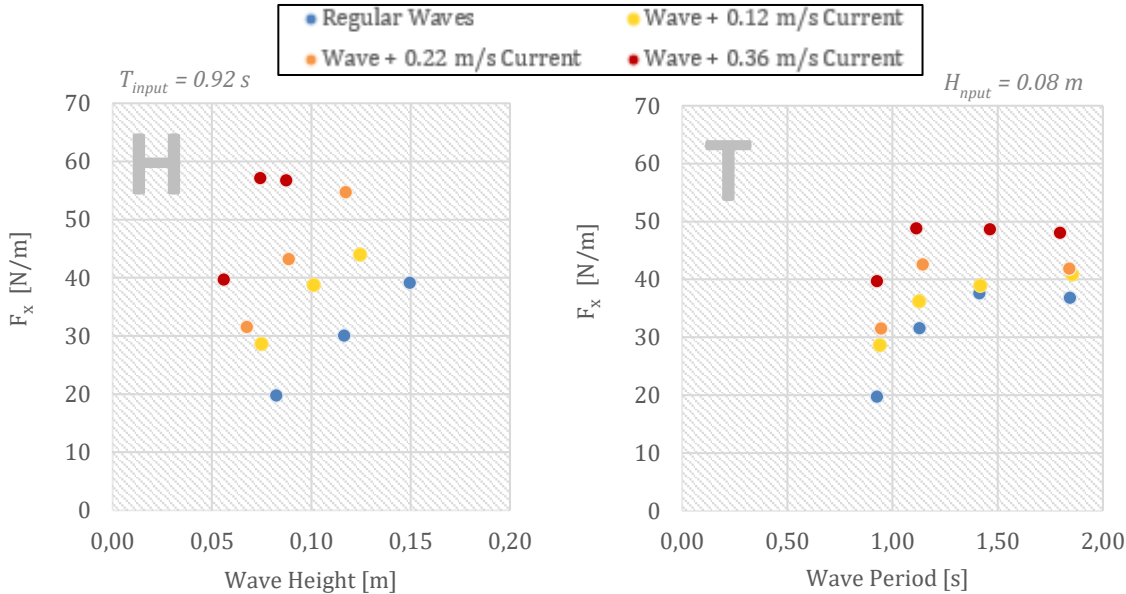


Figure 42: The relationship between the wave height (for $T \approx 0.92$ s) and the horizontal hydrodynamic force and the wave period (for $H \approx 0.08$ m), both with $d_s = 0.35$ m.

The right graph in Figure 42 gives the hydrodynamic force for an increasing wave period. From this graph an increase in the measured force is seen for an increase in the coexisting current component. As mentioned before, the magnitude of the wave period remains relatively unchanged. The series all show a similar curvature when related to the measured force. This curvature is equal to the expected curvature described for the situation of a regular wave only, see Figure 41. Further, it is noticed that the same wave period gives a larger force when the added current is increased. This is due to the same reason as for the wave height in Figure 42. Namely, due to an increasing contribution of velocity related drag component, which takes account for the non-zero baseline force.

Next, the relationship between the vertical hydrodynamic force and the same wave parameters, wave height and wave period, will be studied. Figure 43 gives the same graphs as Figure 42 but now for the vertical hydrodynamic force instead of the horizontal hydrodynamic force. The trend shapes of both graphs are similar to the shapes found for regular waves only in Figure 40. Looking at the left graph, presenting the wave height relationship, a few things are found:

Just like for the wave height in relation to the horizontal hydrodynamic force:

- The relationship between the wave height and vertical hydrodynamic force remains linear, because the inertia component remains dominant.
- The magnitude of the wave height decreases for the same input wave height.

In contrast to what was found for the wave height in relation to the horizontal hydrodynamic force:

- There still is a zero vertical velocity baseline and a zero vertical force baseline, since the added current is only added in horizontal direction. So an increased force due to an increased drag component is not the case for the vertical direction.
- Larger force magnitudes are found for some of the larger added currents. An explanation for this could be the increased horizontal velocity component which is also present in the expression for the vertical Morison force.

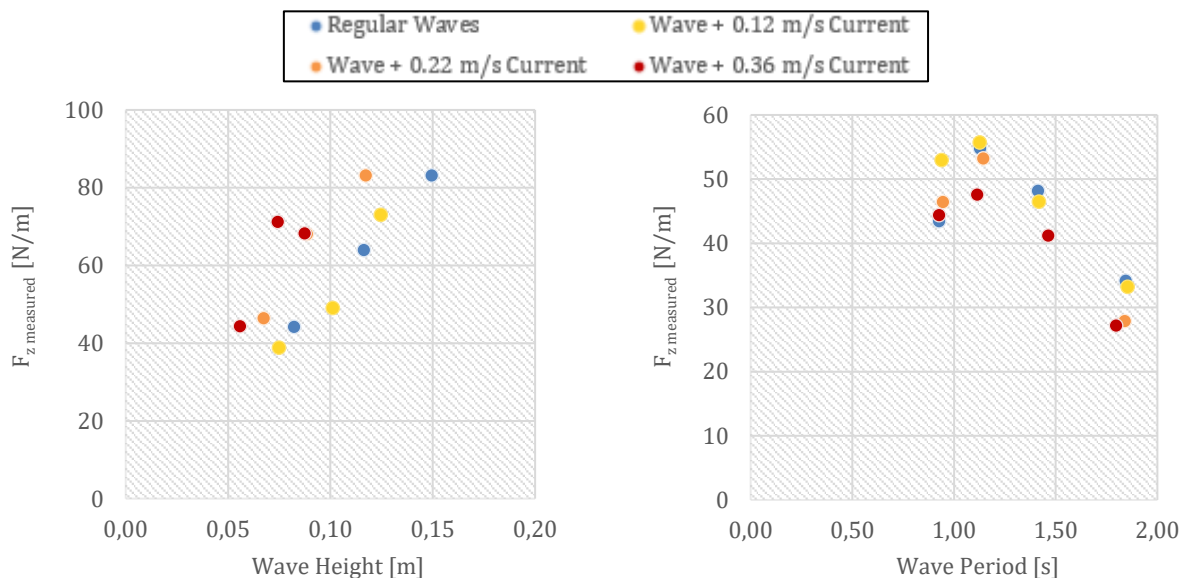


Figure 43: The relationship between the wave height (for $T \approx 0.92$ s) and the vertical hydrodynamic force and the wave period (for $H \approx 0.08$ m), both with $d_s = 0.35$ m.

At last the relationship between the wave period and vertical hydrodynamic force is studied in the right graph of Figure 43. The following is noticed about this relationship:

- The same shape of relationship curve is found as was for the regular waves, Figure 40.
- The wave period is almost not affected in magnitude by an added current, which agrees with Figure 34.

4.1.3. The Answer to Research Question 1a

In this paragraph conclusions are drawn for research question 1a based on the findings of the previous sections. Research question 1a was formulated as follows:

Research Question 1a

What is the relationship between the environmental parameters; wave height, the wave period, current velocity and submergence depth, and the hydrodynamic forces on a fixed rectangular cylinder in small-scale flume experiments subjected to regular wave, current and combined wave-current conditions?

The conclusions will be drawn for each relationship separately, starting with the wave height:

Wave height

The wave height is found to be linearly related to the vertical and horizontal hydrodynamic force in case of only regular waves as well as for a situation with combined waves and current. The magnitude of the wave height decreases as the added current component increases. For a similar wave height but increased added current, the magnitude of the horizontal hydrodynamic force is larger because of an increased drag component due to a non-zero velocity baseline. The magnitude of the vertical hydrodynamic force increases because of the horizontal velocity component present in the description of the vertical hydrodynamic force as well.

Wave period

The relationship of the wave period to the hydrodynamic forces is well predicted by the wave period-acceleration curves found with linear wave theory. For waves combined with current the same wave period results in higher horizontal forces because the velocity related drag component becomes of more importance due to the non-zero horizontal velocity baseline.

Current Velocity

In case of a only current situation, only drag is of significance since a constant velocity gives no acceleration and thus no inertia. Therefore the current velocity is related to the horizontal hydrodynamic force through an quadratic velocity term. When a current velocity is added to a wave field, it increases the drag component of the hydrodynamic forces. In case of the horizontal hydrodynamic force the drag component increases due to the increases baseline velocity value.

Submergence Depth

For regular waves it is found that a larger submergence depth gives smaller horizontal and vertical hydrodynamic forces. This agrees with linear wave theory describing smaller orbital water particle velocities and accelerations for larger depths. In case of an only current situation a clear influence of the submergence depth on the horizontal hydrodynamic force is not found. This agrees with the made assumption that for the depth range tested in this study, the velocity remains of equal magnitude over the depth.

4.2. Force Prediction by Morison

This paragraph put its focus on the coefficients for the Morison equation derived from the fixed model test data of the present study. Finalizing, with showing how well the measured force can be determined by the Morison equation. By doing this research question 1b will be answered at the end of this paragraph.

Research Question 1b

What is the hydrodynamic force prediction accuracy of the Morison equation for a fixed rectangular cylinder in small-scale flume experiments subjected to regular waves and combined wave-current conditions?

4.2.1. Force coefficients

In this part, the drag and inertia coefficients from the fixed model tests are presented and compared to previously done studies. First the force coefficients found for a only current condition are validated by comparing them to coefficients found in other studies. Validating these coefficients gives confidence in the quality of the results found for the regular wave and the combined current-wave tests.

Current

The horizontal forces determined for the only current tests, are translated into drag coefficients. To get the drag coefficient Drag coefficient [Eq. 1] is used. The mean drag coefficients from the present study (X) are compared to the drag coefficients from other studies in Figure 44. In the present study the aspect ratio between the width and the height of the model is 2.5 (B/D). For this ratio a mean drag coefficient of 1.18 is found. Removing the bottom outlier gives a mean drag coefficient of 1.23. Apart from one higher and one lower outlier, most of the red crosses, indicating the present study, are close to the value of approximately 1.3 found by Nagaguchi (1968).

Overall, the found values, are close to the values which would be expected when following the data trends found in the other studies done by Nakaguchi (1968), Bearman & Trueman (1972) and Courchesne & Laneville (1979) performed in wind tunnels and the study by Venugopal (2006) performed in a flume. This gives confidence in the reliability of the coefficients for other parts of the present study.

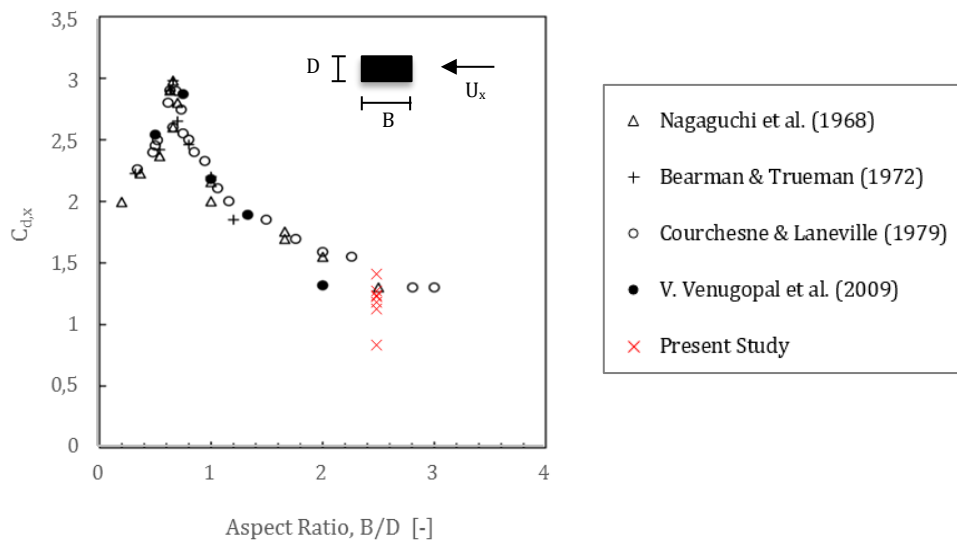


Figure 44: The drag coefficients found in the present and previous studies for different aspect ratios

Regular Waves

For regular waves the force coefficients are determined through the Morison equation together with the least-squares method. This results in the acceleration related inertia coefficient and the velocity related drag coefficient. In this section the drag and inertia coefficients are compared to a similar study as the present study, performed by Venugopal (2006). Venugopal (2006) studied the wave force coefficients for horizontal cylinders with aspect ratio $B/D = 1, 1.3$ and 2 , or $D/B=0.5, 0.75, 1$. However, in his study he uses the ratio of D/B for the aspect ratio, with the graph of Figure 44 as exception where he uses B/D . To stay in line off the definition most used by Venugopal in his 2006 and 2008 paper, from now on the definition of D/B will be applied. Venugopal (2006) applied two different submergence depths in his test of which one is comparable to the 0.175 m submergence depth of the present study and deeper than tested in the present study. He studies the effect of the submergence depth by means of a relative submergence depth given by:

$$\text{Relative submergence depth:} \quad \frac{d}{h}$$

Where:

d : The total water depth in the flume [m]

h : Model submergence depth. Taken as height of the water column from the mid-height of the model to the water surface [m]

Venugopal (2006) found his results to be in good comparison to results from studies by Ikeda (1988b) and two studies by Arai (1993) (Arai, 1995). The results from the present study are compared to the results from Venugopal (2006) in this paragraph, starting with the Inertia Coefficients.

Inertia Coefficients:

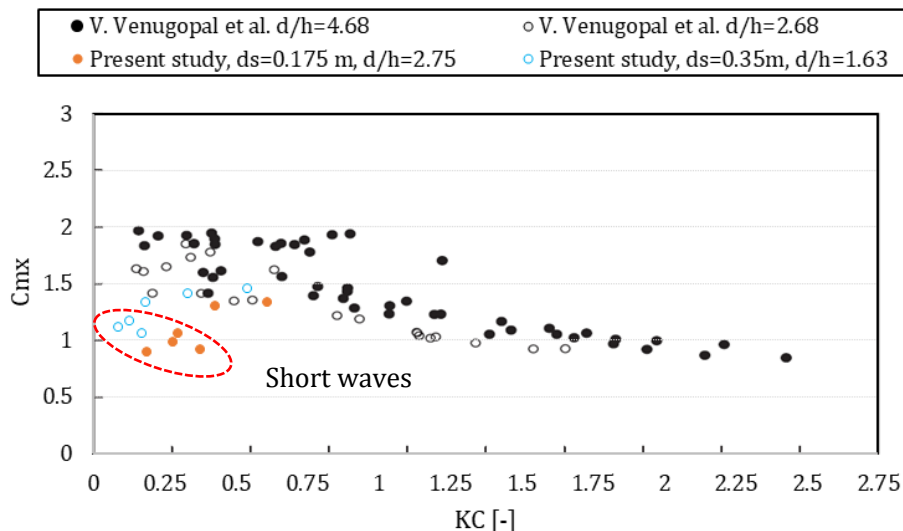


Figure 45: The present study horizontal inertia coefficients (aspect ratio 0.4) compared to the coefficients found by V. Venugopal et al. (aspect ratio 0.5). For different flume depth/submergence depth ratios (d/h).

In

Figure 45, the horizontal inertia coefficients found in the present study are plotted with the KC-number. The orange markers represent the smaller submergence depth of this study, and the blue markers the larger submergence depth. In general, the coefficients found in the present study are smaller than the ones found by Venugopal (2006). This might be due to the difference in aspect ratio between the present and Venugopals (2006) study. In his own study Venugopal (2006) found smaller values of C_{mx} for a smaller aspect ratio. The present study in

Figure 45 depicts a lower aspect ratio of 0.4 compared to 0.5 of Venugopal (2006). This might be an explanation for the lower coefficient values.

Another aspect shown in

Figure 45 is the influence of the (relative) submergence depth. Regarding the submergence depth Venugopal found 'some evidence of lower inertia coefficients at smaller relative depth of submergence'. In

Figure 45, this can be seen by the black solid markers having a larger value than the black empty markers. The present study rather depicts the opposite, the blue empty markers have larger values than the solid orange markers. The difference holds mainly for the first 4 orange markers for $KC < 0.4$. These orange markers represent the steepest waves, R12, R13 and R14, while the blue empty markers in the same KC range depict the longest waves. For the steep waves the linear wave theory water particle velocities used in the Morison analysis give an over prediction of the measured velocity at the EMS depth of 0.2 m. If this over-prediction holds for the model depth water particle velocities as well, smaller water particle velocities and acceleration magnitudes, associated with larger inertia coefficients, would be found. Besides this explanation another argument is found when studying closely the results from Venugopal (2006) between KC -number 0.3-0.7, his results between the two submergence depths mix and give the opposite results as well. To conclude, the present study has limited data in the graph, so full conclusions on the influence of submergence depth are hard to be drawn.

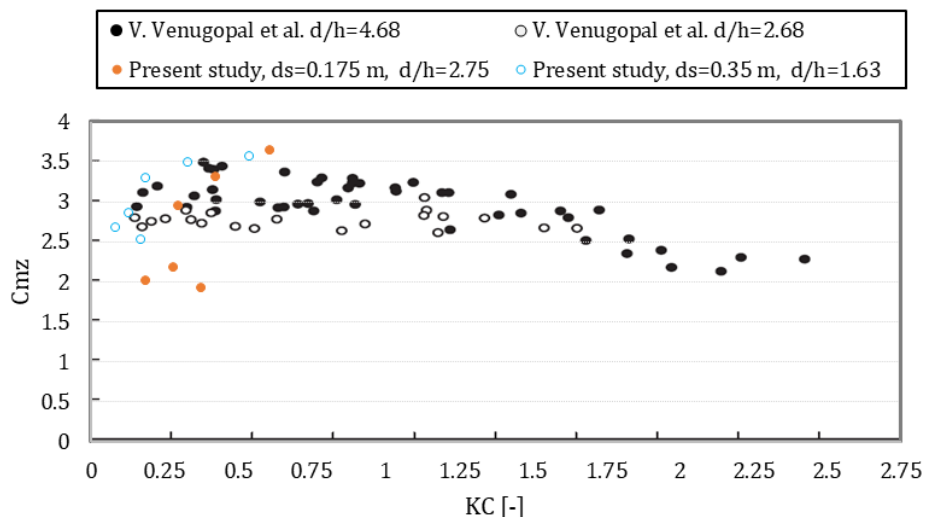


Figure 46: The present study vertical inertia coefficients (aspect ratio 2.5) compared to the coefficients found by Venugopal et al. (aspect ratio 2). For different flume depth/submergence depth ratios (d/h).

Next the findings of the present study in comparison to Venugopal's (2006) results will be discussed, regarding the vertical inertia coefficient. These are presented in

Figure 46. In general, the results between the present study and Venugopal (2006) compare well. Only three of the smaller submergence depth (larger relative submergence depth) results of this study are lower than expected, these are the steep waves. Like for the horizontal inertia coefficient, this can be explained by the over-predicted particle velocity amplitudes used, resulting in lower inertia coefficients. From

Figure 46 it can again be seen that the present study, like for the C_{mx} , seems to give an opposite relationship to the submergence depth as the results from Venugopal (2006). However, for the vertical direction it can also be noticed that in Venugopal's study the distinction between the two submergence depths is not very clear for all KC -numbers, and the solid and empty black markers also mix.

Besides, the comparison between the present study and the study by Venugopal (2006), the values for the horizontal and vertical inertia coefficient can be compared. When comparing the coefficients in these two directions it is seen that the vertical inertia coefficients reach up to larger values, of 3.6, compared to the horizontal coefficients, not being larger than 1.5. The larger coefficients found for the vertical direction can be explained by the increased complexity of the water particle path in this direction. For the vertical direction the water gets more distorted by the presence of the model, because the model dimension is larger normal to the vertical. Besides this larger projected area for the vertical motion, in addition the water has to come from below and there is a layer on top of the model. So to conclude, the distortion for the water in vertical direction is larger than for the horizontal direction, resulting in larger inertia coefficients.

Drag coefficients:

Now the drag coefficients are studied, beginning with the horizontal drag coefficients presented in Figure 47. Large negative drag coefficients are found for the smallest KC numbers. When the KC number increases the values become less negative and some even become positive. Comparing this to the studies by Arai (1993) and Venugopal (2006) shown in Figure 48, this trend shows to be opposite (around the KC axis) of their findings. Their values are evenly large in magnitude but are positive instead of negative. Nevertheless, this is not found to be too worrying, for which the reason will be discussed below Figure 48.

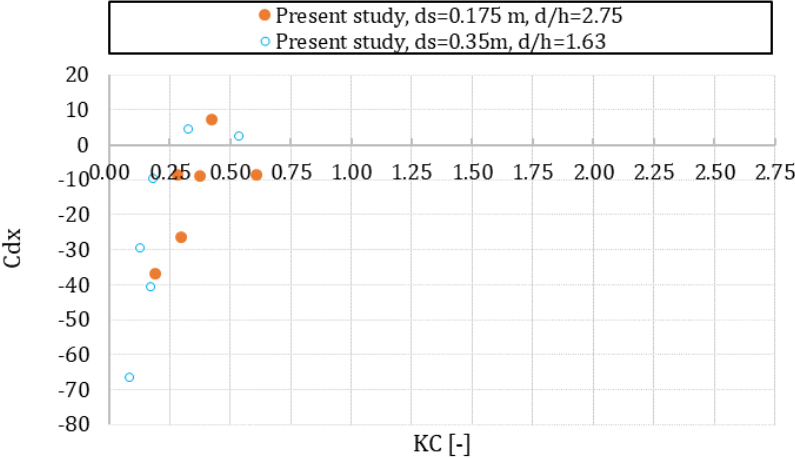


Figure 47: the horizontal drag coefficients found in the present study.

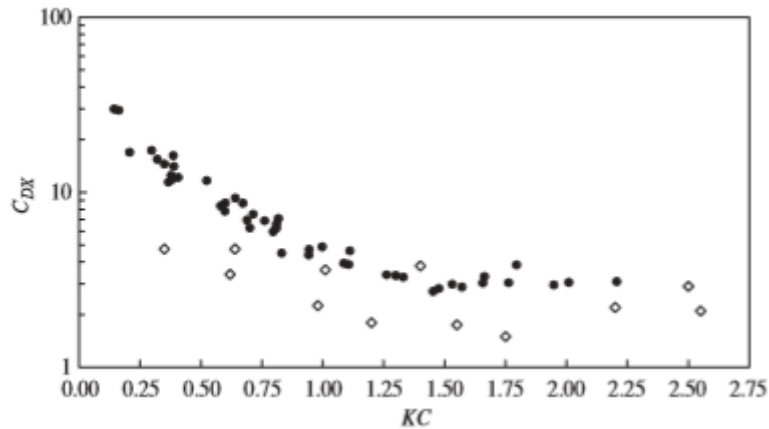


Figure 48: the horizontal drag coefficients found by • Venugopal (2006) and ◊ Arai (1993)

As has been discussed multiple times in this chapter, low KC numbers correspond to inertia dominance and to high drag sensitivity. For the force this means that it's magnitude is determined by the inertia force component, while the drag component mainly contributes to phase/shape shifts in the force. The sensitivity of the drag coefficients can be seen through the very large range of drag coefficient values found in many studies. The explanation for the negative drag coefficients found in the present study probably lies in the method of applying a phase shift between the force and velocity/acceleration signal. In case of inertia dominance, the acceleration signal has a very small phase shift to the force peak. The sign of this phase shift determines the sign of the drag coefficient. In the present study the force peak is a little earlier in time than the acceleration related inertia force peak. This is compensated for by the drag force component by giving a force peak $\frac{1}{4}$ wave period before the inertia peak. For the velocity to deliver a drag force peak at $\frac{1}{4}$ wave period a negative drag coefficient is needed. The studies by Arai (1993) and Venugopal (2006) probably have a force-inertia phase shift of opposite sign compared to this study. This leads to positive drag coefficients instead of negative. The concept of the influence of the phase shift will be explained in the chapter 5.

For the drag coefficient in vertical direction large negative values are found as well, shown in Figure 49. Again this is the opposite of what Arai (1993) and Venugopal (2006) have found. The same reason, being the inertia and force peak shift sign, is suggest as for the drag coefficient in horizontal direction.

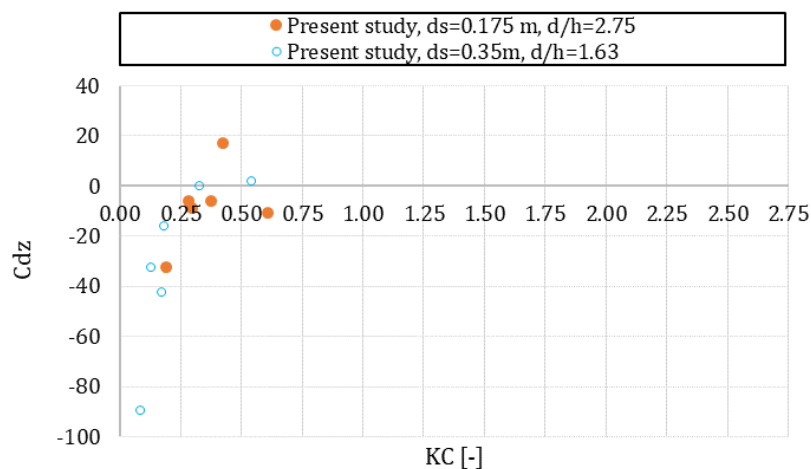


Figure 49: the vertical drag coefficients found in the present study.

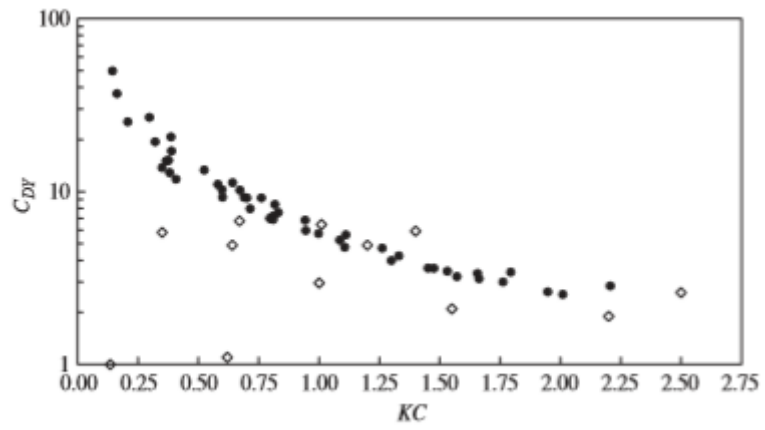


Figure 50: the vertical drag coefficients found by • Venugopal (Venugopal, 2006) and ◊ Arai (Arai, 1993)

Combined wave-current

This paragraph analyses the outcomes from the combined waves and current tests, by comparing them to the results of a similar study by Venugopal (2008). In his study Venugopal uses the same model as in his study for regular waves, giving the same aspect ratios of $B/D = 1, 1.3$ and 2 . In which the largest ratio of 2 is just a little smaller than the aspect ratio of the present study of 2.5 . Further, it must be noticed that the study by Venugopal added current velocities to the waves, do not come from an actual current, but the current is simulated by towing the model with a constant velocity through a wave field. While in the present study, an actual current was created in the flume, to which waves were added.

In this section the force coefficients will not be presented with the general KC -number, but with a adjusted version of the KC -number, where a multiplication factor is added.

$$KC_{new} = KC \left(1 + \left| \frac{U_c}{U_m} \right| \right)$$

In this new KC number the value for regular waves remains the same, so $KC_{new} = KC$. When a current is added the factor between brackets increases. The larger the current component of the velocity is relative to the particle wave amplitude velocity component of the velocity, the larger the factor becomes. The new KC -number is one of the KC -numbers defined by T. Sarpkaya (1985) to well present the force coefficient for combined wave and current condition.

First the inertia coefficients, presented in Figure 51 are studied. The horizontal inertia coefficients found in the present study, are in the same range as the results found by Venugopal. In the conclusion of his study, Venugopal (2008) mentions to have found significantly smaller inertia coefficients for tests including current compared to tests with only regular waves. From the results of the present study a conclusion like this seems less significant. Only two of the regular waves tests have an overlapping KC_{new} with tests including current. For those two waves, the horizontal inertia coefficients are a little lower. For the vertical inertia coefficients this is the same case. Therefore, from the present study it can only be concluded that the inertia coefficients remain relatively of the same magnitude when a current velocity is added to a wave field. The mean value for the horizontal inertia coefficient is 1.18 and the vertical inertia coefficient is 2.71 .

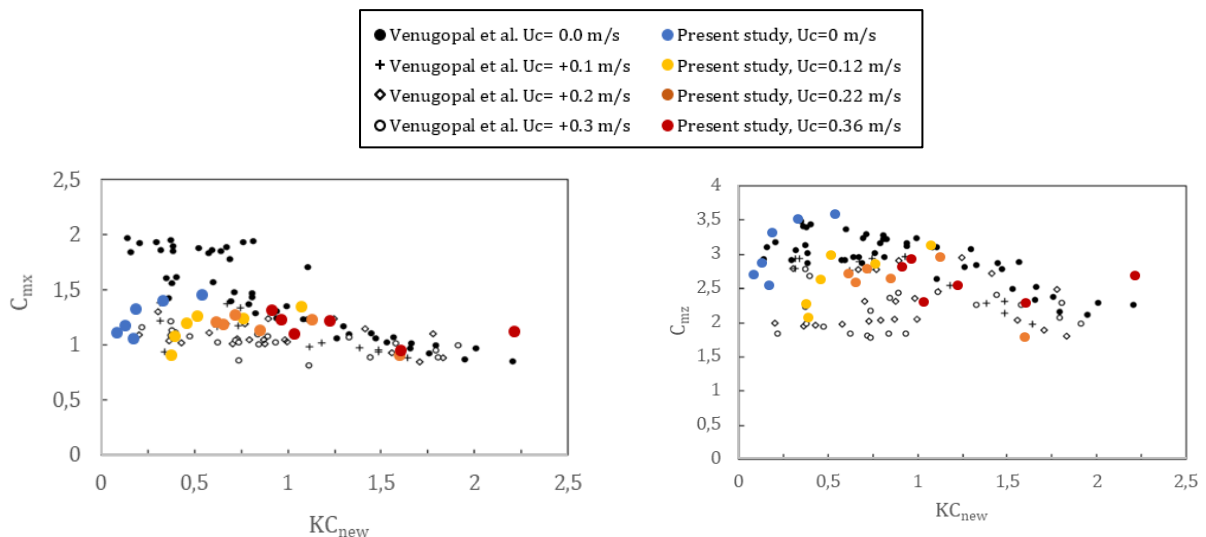


Figure 51; The horizontal and vertical inertia coefficients for the situation of combined wave and current. The results of the present study ($d_s=0.35$ m) with aspect ratio 0.4 (D/B) and the results by Venugopal (2008) with a larger aspect ratio= 0.5 .

Second, the drag coefficients, presented in Figure 52, are evaluated. Like for regular waves only, the drag coefficients for the combined wave and current situation are still highly variable in value. Again, the magnitude of the drag coefficients for the smallest KC number is in the same range, but the sign is the opposite. As the added current increases, the horizontal inertia coefficients increase and come to a more stable value for the largest two added currents, this seen in Figure 53. The mean value of the coefficients depicted in this graph is 1.18, which is equal to the drag coefficient found for the only current condition.

For the vertical drag coefficients, the magnitude of the coefficients also decreases, but they do not go to a stable positive value like was found for the horizontal drag value. In contrast to the horizontal direction, no non-zero baseline velocity is added in the vertical direction. For the horizontal direction it is this non-zero baseline that defines the horizontal drag coefficient to be positive, even though there might still be a phase shift between the inertia and force peak to be compensated for. Because no non-zero baseline vertical velocity is present, the drag coefficients can still flip sign to account for a positive or negative phase shift of the force and inertia force.

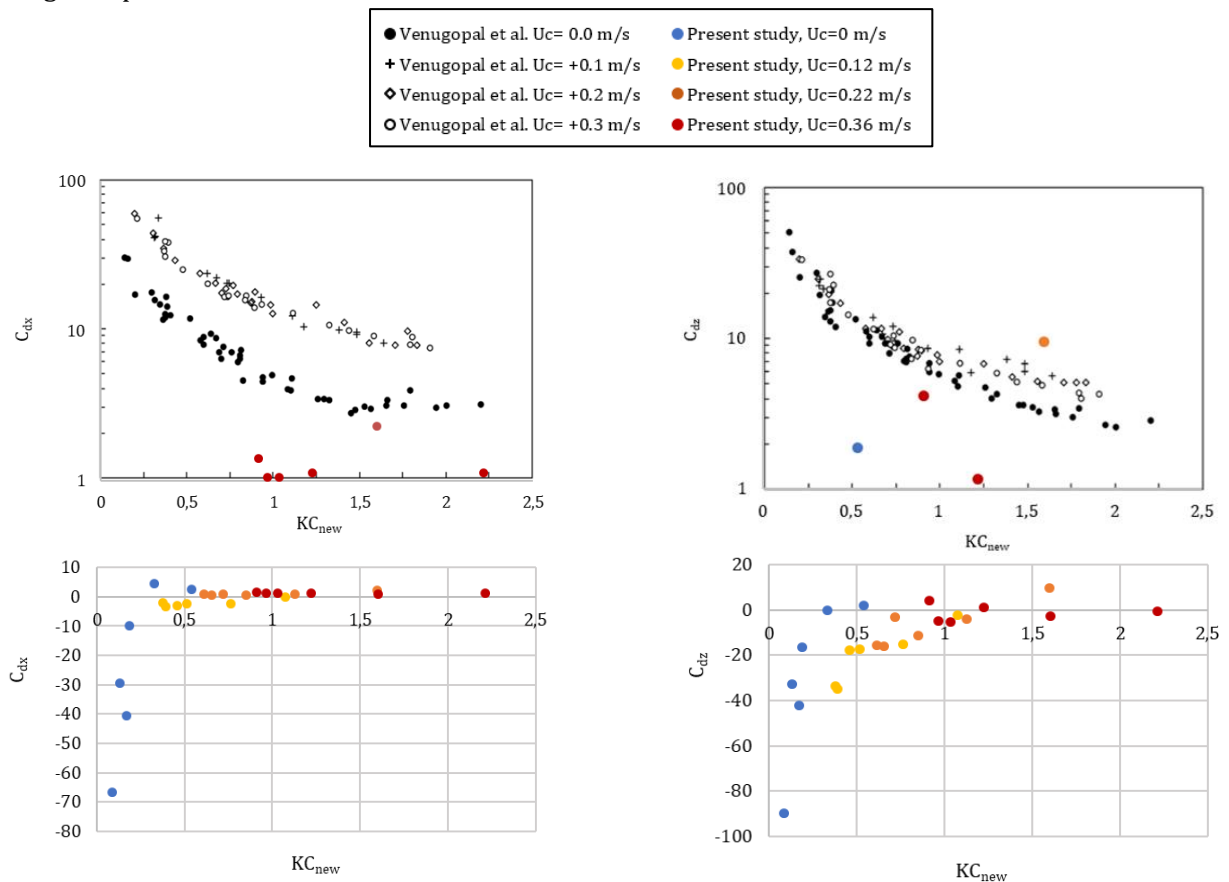


Figure 52: Horizontal and vertical drag coefficient from present study compared to the results of Venugopal study.

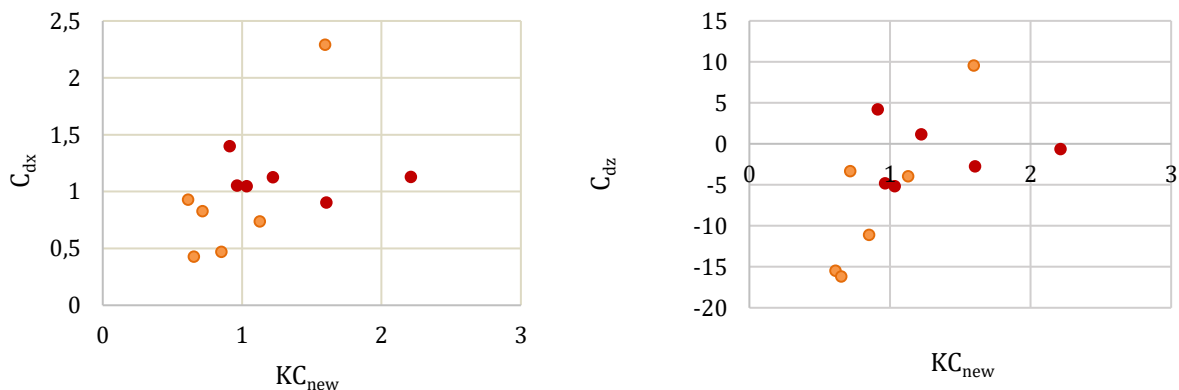


Figure 53: The horizontal (left) and vertical (right) drag coefficient for the two largest added current conditions.

4.2.2. Force prediction by the Morison Force

This last section of paragraph 4.2 deals with presenting the results of the prediction of the hydrodynamic forces by the Morison equation. First, the procedure of selecting coefficients for the force prediction is given, after which the results of the force prediction with these coefficients are presented and analysed.

The Force Prediction Coefficients

The previous section 4.2.1 presented the force coefficients found in the present study. The drag and inertia coefficients that are used for the force prediction are based on the force coefficients found in the previous section. The inertia coefficients for the force prediction in regular waves are based on a linear trend line found for the relationship between the KC-number and the coefficient. This holds for both the vertical and horizontal inertia coefficient. As an example the trend line for the horizontal inertia coefficient is given in Figure 54. The full prediction coefficient determination is given in Appendix C.

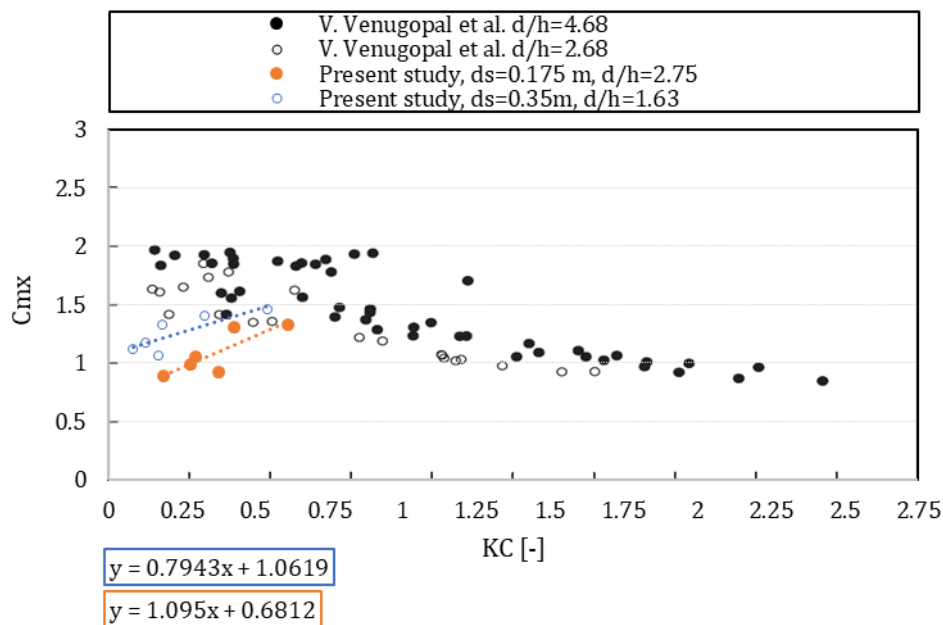


Figure 54: Example of the trend line used for determination of the Morison prediction coefficients for regular waves.

For the combined wave-current conditions a mean coefficient value is extracted from the inertia coefficients found in the previous section 4.2.1. From this mean a few outliers are removed, to eventually end up with a constant value for the inertia coefficients. This procedure is used for both the horizontal and vertical coefficients. An overview of coefficients used in this procedure is given in Appendix C.

The two procedures for the regular wave and combined wave-current conditions, leads to the following Morison force coefficients that will be used for the prediction of the hydrodynamic forces.

Table 11: The Values for the Coefficients used in the force prediction

Regular Waves		Combined Wave-current
for $d_s=0.175$ m:	$C_{mx} = 0.794 \cdot KC + 1.062$	$C_{mx} = 1.21$
for $d_s=0.35$ m:	$C_{mx} = 1.095 \cdot KC + 0.681$	
for $d_s=0.175$ m:	$C_{mz} = 3.818 \cdot KC + 1.281$	$C_{mz} = 2.68$
for $d_s=0.35$ m:	$C_{mz} = 2.079 \cdot KC + 2.570$	

For the drag coefficients for both the regular wave conditions and the combined wave-current conditions the values found for the only-current condition are used. For the horizontal drag coefficient the value of 1.18 for aspect ratio 2.5 (B/D), found in section 0 and shown in Figure 44, is used. For the vertical drag coefficient the value from Figure 44 of the opposite aspect ratio of 0.4 (D/B) is used, equal to 2.30 is used in the force prediction. The drag coefficients used in the force prediction are summarized in Table 12.

Table 12: The Values for the Coefficients used in the force prediction

Regular Waves	Combined Wave-current
$C_{dx}=1.18$	$C_{dx}=1.18$
$C_{dz}=2.30$	$C_{dz}=2.30$

Force Prediction

Now the coefficients for the force prediction are determined, the results of the Morison force prediction itself are presented and discussed. Therefore, first the prediction of the force magnitude is discussed. Second, the shape of the force is discussed.

Force Magnitude:

Figure 55, shows the measured forces on the vertical axis and the predicted force on the horizontal axis, for the regular wave conditions in blue and the combined wave-current conditions in yellow, orange and red for an increasing current component. The measured force, is the mean peak force value of a couple of wave from that specific wave type. The predicted force is the constant peak force value for the specific wave type. The left graph, for the horizontal force prediction, shows mainly an under-prediction of the force. Most of the cases show an estimation error smaller than 15%. Estimation errors larger than 15%, but smaller than 30%, are found mainly for the tests with the largest two current components. For the vertical force prediction in the right graph, the force is also mainly under-predicted, however, the number of tests that are over predicted is larger than for the horizontal force prediction. For regular waves, the over and under predictions are smaller than 15%. The yellow markers, representing the waves combined with the smallest added current component, show to give an error larger than 15% the most.

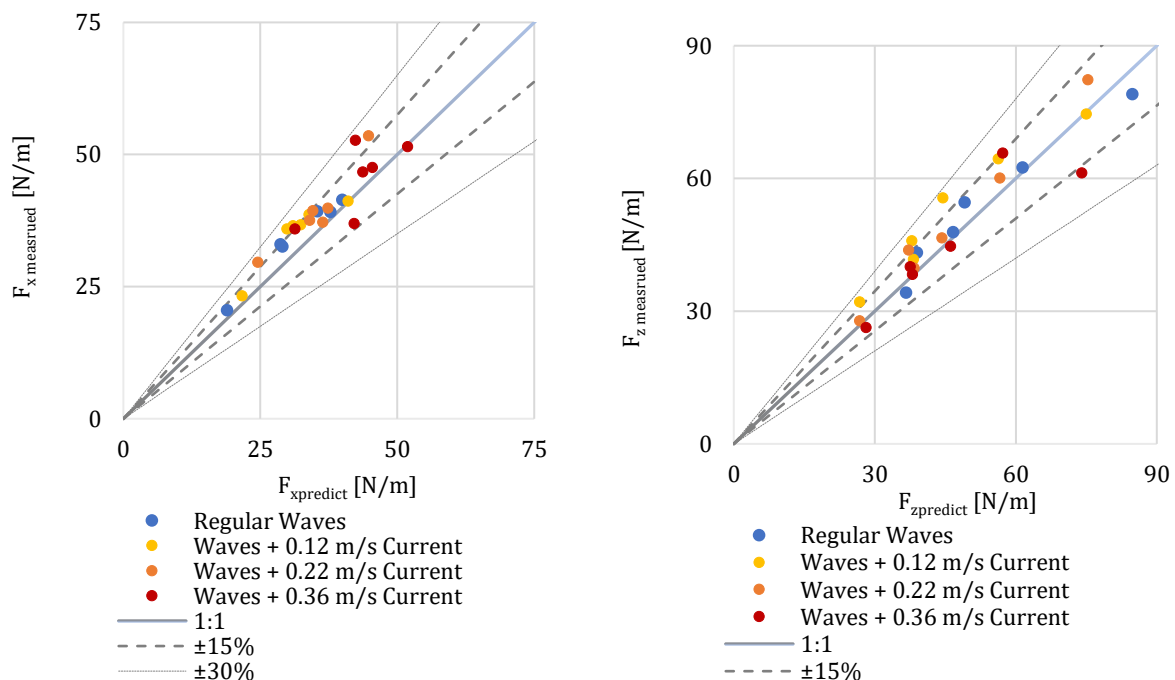


Figure 55: The mean measured horizontal and vertical hydrodynamic peak forces plotted with the predicted horizontal and vertical hydrodynamic peak forces.

Table 13, is presented to give more insight on the influence of the added-current component on the prediction of the force. In this table, the mean prediction ratio R and the accompanied standard deviation are presented. The following definitions are given to these parameters:

$$R = \frac{F_{measured}}{F_{predicted}}$$

Where:

- R: The force prediction ratio [-]
- $F_{predicted}$: The Morison predicted constant peak force [N/m]
- $F_{measured}$: The maximum measured peak force from the analysed force signal section [N/m]

Table 13, indicates that for both the vertical and horizontal direction the mean ratios for both regular waves and combined wave-current force conditions, are ratios ≥ 1 , meaning an under-prediction of the force. For both directions, an increase in the prediction error is found when a current component is added to the waves. However, no clear increase in the ratio is seen for an increases in the magnitude of the current component. For all conditions there is an increase in the standard deviation of the ratio for an increasing current component, indicating that a less consistent ratio between the measured and predicted force is found for the conditions of waves with the largest added current component. For all conditions the mean error between the predicted and measured force, is no larger than 15%.

Table 13: R, the ratio between the measured and predicted force, and the standard deviation. For horizontal and vertical directions.

	$\overline{R_x}$	σ_x	$\overline{R_z}$	σ_z
Regular Waves	1.09	0.04	1.02	0.07
Wave +0.12 m/s	1.12	0.07	1.15	0.09
Wave + 0.22 m/s	1.12	0.07	1.07	0.05
Wave + 0.36 m/s	1.06	0.12	0.99	0.10

Force Shape:

Next, the shape of the Morison predicted force is compared to the shape of the measured force. Figure 56, the left column shows three panels. From top to bottom these panels show, the measured force and the predicted force, the measured force and the inertia force component, and the measured force with the drag force component. In the right column, the same three panels are shown, but now for the condition of waves with the largest current component.

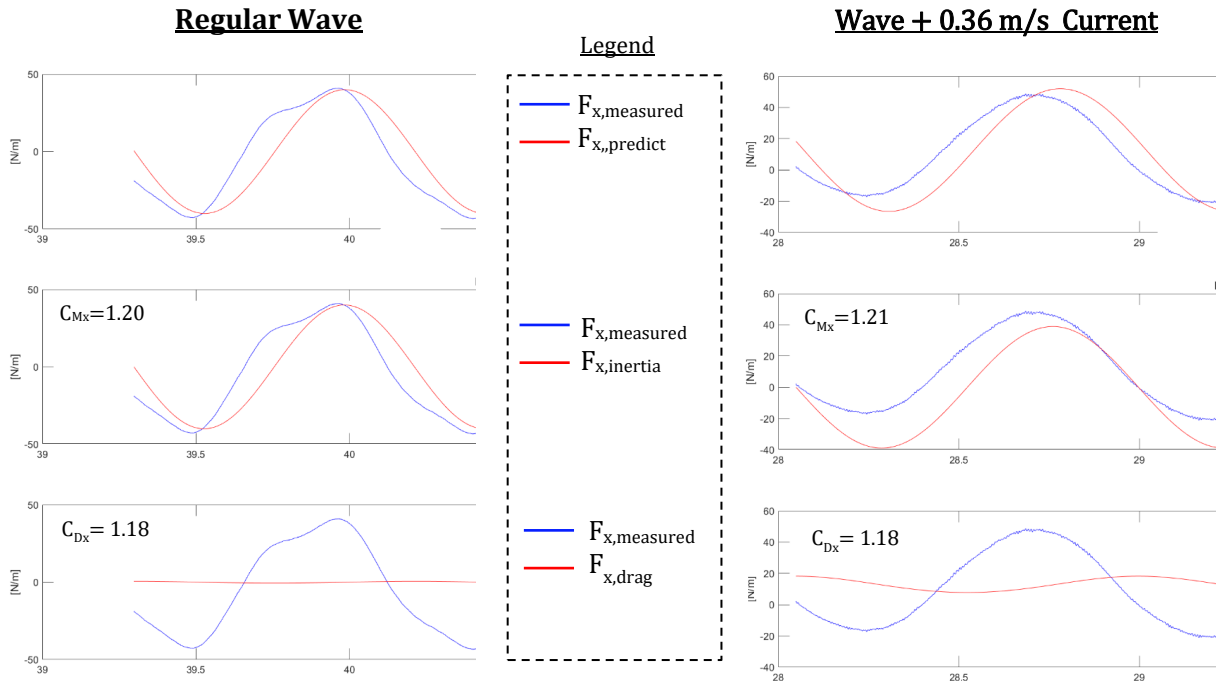


Figure 56: The horizontal measured force signal plotted with the total Morison force (top panel), the inertia force component (middle panel) and the drag force component (bottom panel). For two environmental conditions regular wave and combined wave and current (FR14).

First the regular wave condition is studied. For the wave in Figure 56, the peak of the force, in blue, is very well determined by the predicted force, in red. Looking at the middle panel, it is seen that the magnitude of the force is determined completely determined by the inertia component of the force. The bottom panel shows that the drag force component is of negligible influence. Shape-wise the force is not approximated well by the Morison (inertia) force. The highest peak in the force signal does relatively coincide well with the peak of the Morison force. However, the measured force shows a shoulder in the signal, which is not accounted for by the sine-shaped Morison force signal. To approximate the shoulder better, a large negative drag coefficient, would help. This is shown in Figure 57. Here the force prediction is shown for three different values of C_d (C_d , C_d-50 and C_d-20), while the C_M is remained constant and equal as in Figure 56. This figure shows that a larger negative drag coefficient shifts the Morison force peak to the left closer to the 'shoulder', while the magnitude of the peak is remained relatively unchanged. These larger negative drag coefficients agree with the drag coefficient values found in the previous section 4.2.1.

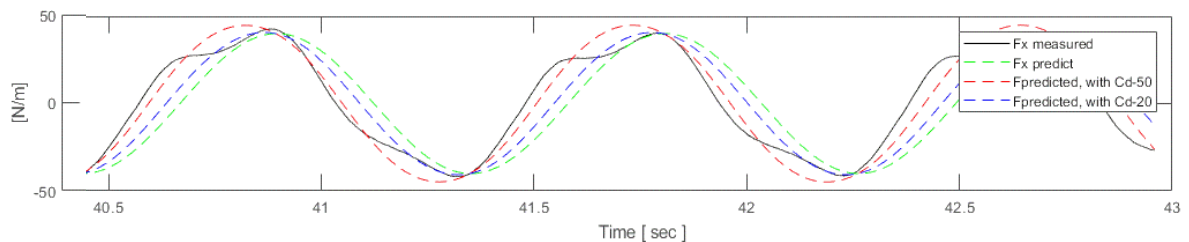


Figure 57: The measured force (black) with a Morison force prediction for three different values of C_d . For a regular wave.

The right column in Figure 56, shows the condition of waves combined with the largest current component. This specific test is one of the test that give an over-prediction of the force. Again the peak of the force signal coincide relatively well, there is only a small shift of predicted Morison force to the right. The middle panel shows that the inertia component of the Morison force only gives an under prediction of the force. More interesting to see is the bottom panel, presenting the measured force

signal together with the Morison drag force component. In contrast with the regular wave condition, the water particle velocity has increased due to the presence of the added current, resulting in a larger more significant drag force component. However, the force amplitude of the drag force component is still small, it is mainly the non-zero force baseline that gives a large contribution to the total Morison force approximation. In total, the force magnitude from the inertia component, combined with the non-zero force base-line from the drag force component, the total Morison force prediction is the result.

Figure 58, shows the same wave, but now with the vertical forces. For the regular wave, shown in the panels of the left column, the phase shift between the force signals is more clear than for the ‘shoulder’ in the horizontal force. The magnitude of the force is approximated well by the inertia again, only the error is a little larger and giving an over-prediction. The contribution of the drag force component, in the bottom panel, to the regular wave force is again negligible. This is in agreement with inertia dominance. The right column, showing the wave combined with the largest added current, a difference is found compared to the horizontal force. Where for the horizontal direction the measured force showed a non-zero baseline, which was accounted for by the Morison drag force component, this is not the case for the vertical direction. This corresponds to what is expected for a zero velocity baseline, compared to the non-zero velocity baseline for the horizontal direction. The drag force component in the bottom panel, has a larger force amplitude than for the regular wave condition. This is explained by the influence of the horizontal velocity (from the added current) which is present in the expression for the vertical Morison force as well, see section 3.4.3.

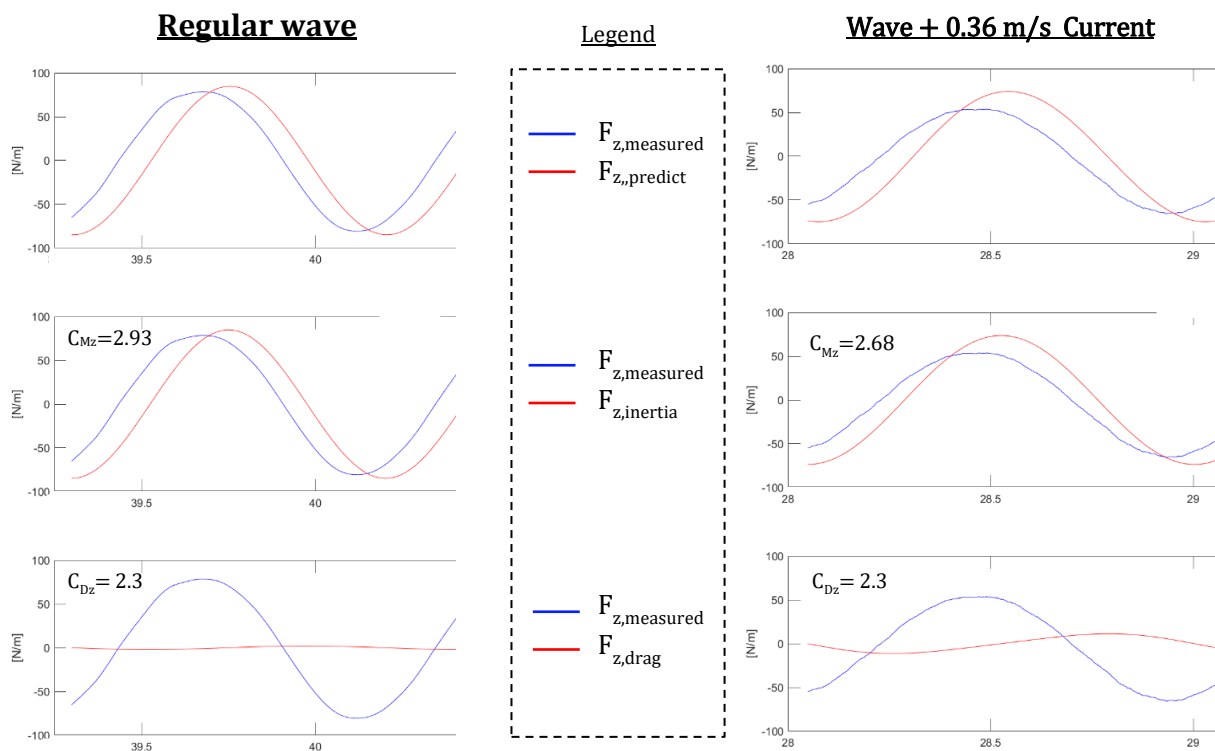


Figure 58: The vertical measured force signal plotted with the total Morison force (top panel), the inertia force component (middle panel) and the drag force component (bottom panel). For two environmental conditions regular wave and combined wave and current.

4.2.3. The Answer to Research Question 1b

In this paragraph, conclusions are drawn for research question 1b based on the findings of the previous sections. Research question 1b was formulated as follows:

Research Question 1b

What is the hydrodynamic force prediction accuracy of the Morison equation for a fixed rectangular cylinder in small-scale flume experiments subjected to regular waves and combined wave-current conditions?

For the prediction of the horizontal hydrodynamic force by the Morison equation a maximum mean magnitude error of 12% is found. For the vertical hydrodynamic force a slightly larger mean magnitude error of 15% is found. For both directions, the force is generally under-predicted by the Morison force. For most of the cases of a combined wave-current condition larger differences between the measured and predicted forces are found, than for regular waves. The amplitude magnitude of the force is predicted well by the inertia force component, while the drag force component approximates the non-zero force baseline, in case of a combined wave-current condition. For most cases a phase shift is found between the measured force and the inertia force component, thus for the total Morison force.

4.3. The Dynamic Response to Environmental Conditions

In this paragraph the results from the tether model are discussed. Relationships between the environmental conditions and the response of the model are analysed. At the end of the paragraph a reflection will be made on the second research question formulated in the introduction chapter of this report. The question was as follows:

Research Question 2

What are the kinematic model response and the force tether response of a tethered rectangular cylinder subjected to a regular wave environment in small scale flume experiments? And what is the influence of the structure submergence depth and tether angles on these responses?

In this paragraph the prediction on the tether forces are made by using the force coefficients found for the fixed model, discussed in the previous paragraph 4.2.

4.3.1. Experiment Observations

For the tether model tests some additional variables were obtained compared to the fixed model tests. The kinematics related variables measured for the model were the sway and heave displacements from video records and the model accelerations were measured with accelerometers inside the model itself. An overview of all measured variables is listed in Chapter 3.

Model Movements

Figure 59, shows three snaps short of a short wave and a long wave running over the model. Comparing the position of the model, the model is seen being tilted clockwise and counter clock wise due to the short wave and the model is almost undisturbed for a long wave. When the short wave arrives at the model it pushes down the front. As it runs over the model, the wave breaks at the end of the model and pushes down the model. The long waves does not break. However some high frequency fluctuations of the water surface can be seen in the wake at the back side of the model.

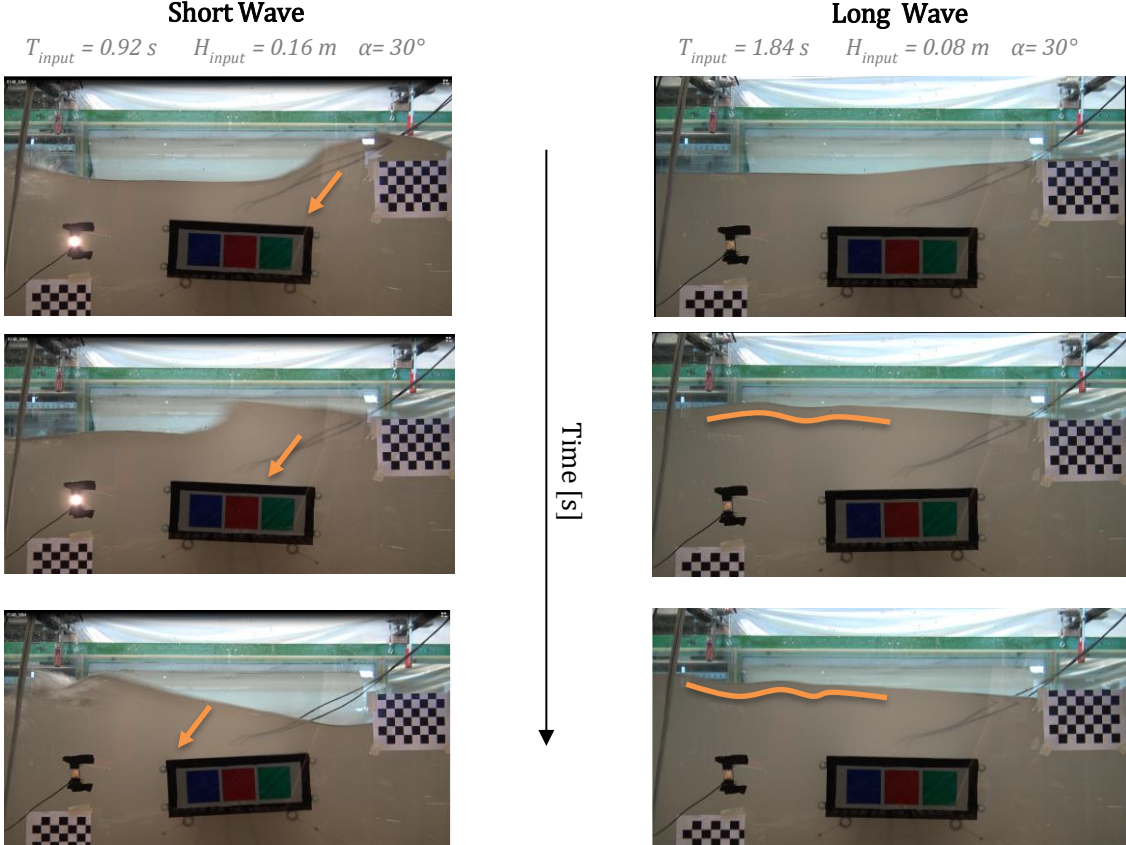


Figure 59: Snap shots from a short wave (R14) and a long wave (R42) running over the model. $d_s=0.175\text{ m}$. $\alpha=30^\circ$

Next, Figure 60, shows snap shots of the model movement of the 70° configurations under the same short and long wave, for the short wave it is seen that the horizontal movement, sway, is relatively equal to both directions. For the long wave, this is different. The model first makes a movement to the left. Next it moves to an intermediate position just left of the centre. After switch it makes a large movement to the right.

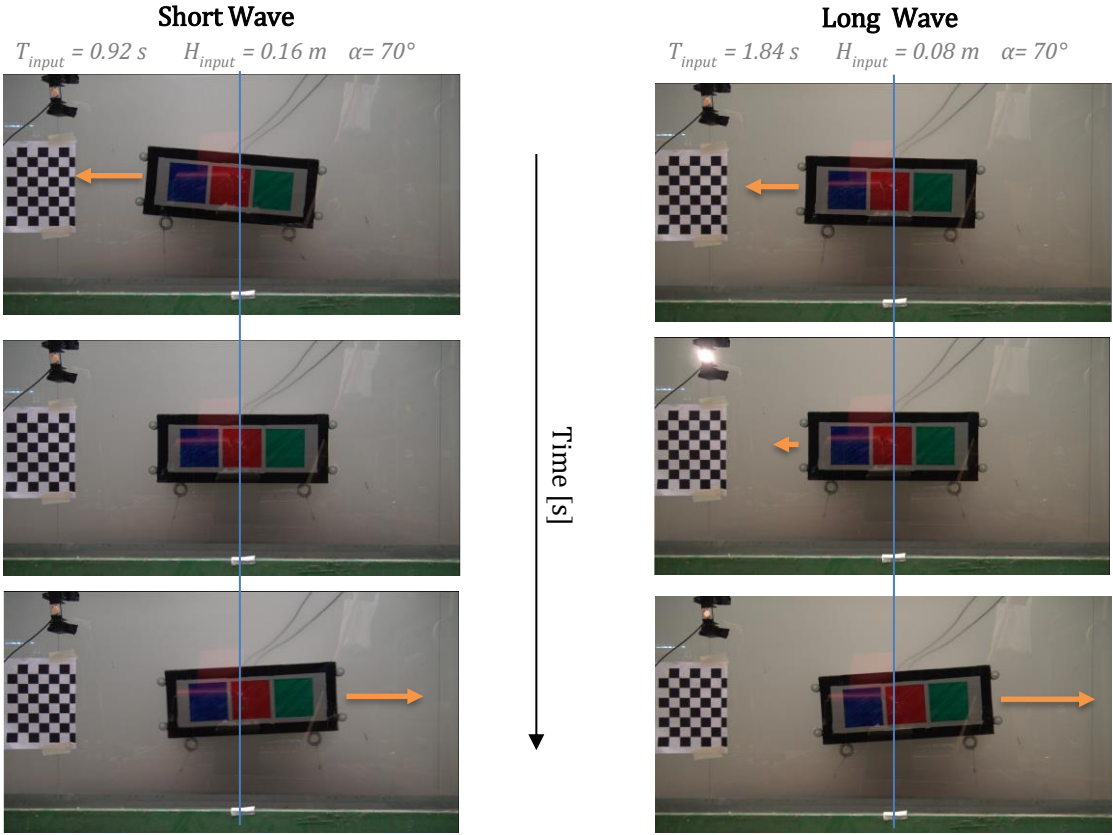


Figure 60: Snap shots from a short wave (R14) and a long wave (R42) running over the model. $ds=0.35\text{ m}$, $\alpha=70^\circ$

The sway and heave motions for both wave types of Figure 60 are plotted in Figure 61. The signal for the horizontal displacements verify the motions from the snap shots. Another thing noticed in these signals, is that the magnitude of the sway motions are much larger than those of the heave motion.

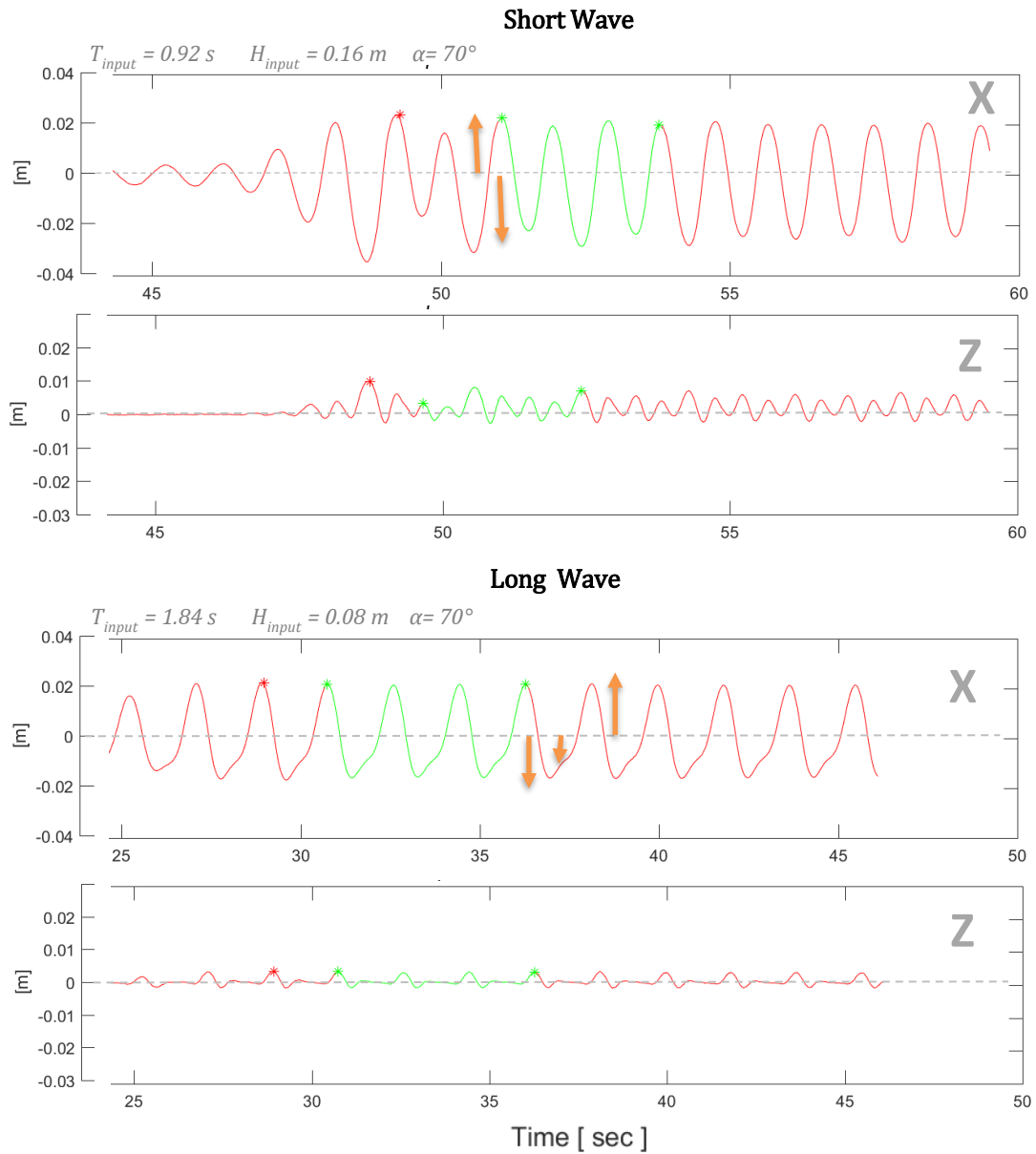


Figure 61: The vertical and horizontal displacements of the red marker for a short (R14) and long wave (R42) for $ds=0.35\text{ m}$, $\alpha=70^\circ$

Slack

In still water an initial tension force is found in the tether of the model, due to the net upward directed force acting on the model. However, during the tests the displacements can be of such a magnitude that the tension in the tether is gone and slack occurs. Slack is followed by a large snap force when the model is displaced back and the tether suddenly is under tension again. The phenomenon of slack disturbs the harmonic force signal and gives large force peaks.

For the tests with a submergence depth of 0.35 m and a tether angle of 30°, in Figure 62, the signals of the absolute total tether forces shows that no slack occurs. The signal remains nicely harmonically and the negative amplitudes of the force remain at a close distance of the 0 N. Absolute tether forces of close 0 N would indicate slack.

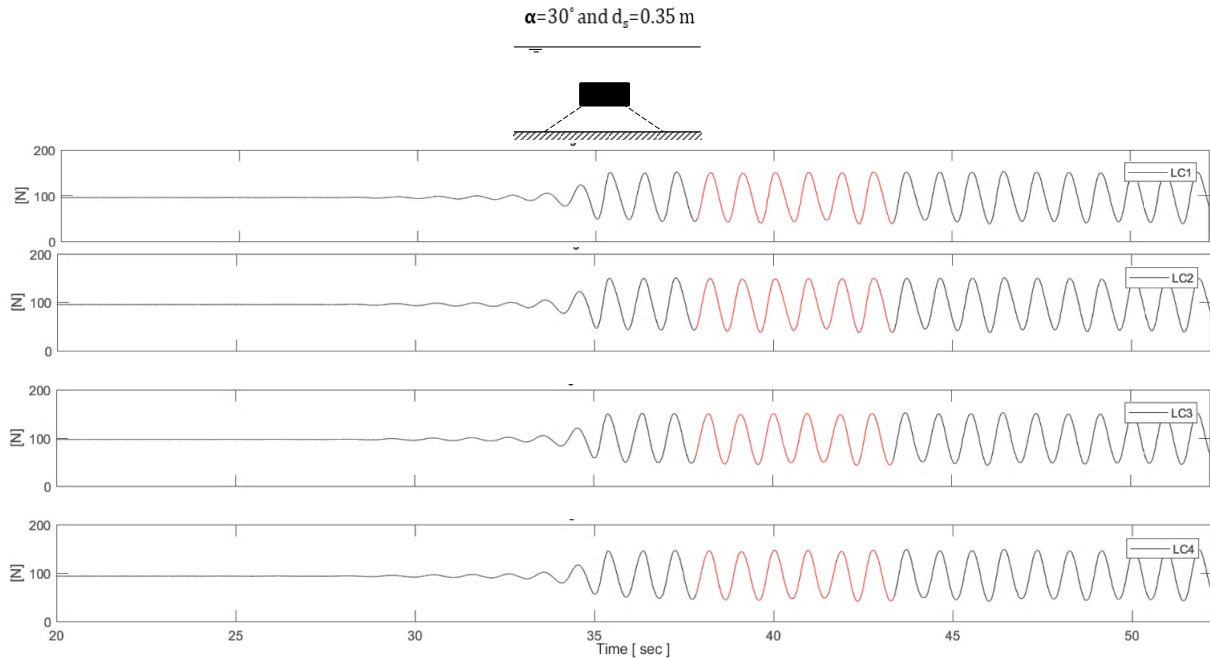


Figure 62: Example of a total tether force signals. For the condition of a submergence depth of 0.35 m and a tether angle of 30°. (R14C_30)

For the condition of the same submergence depth but a tether angle of 70° , in Figure 63, the force gets very close to zero, which means no slack and snap forces should occur. Still the shape of the signal changed significantly and does not look as clear harmonically any longer.

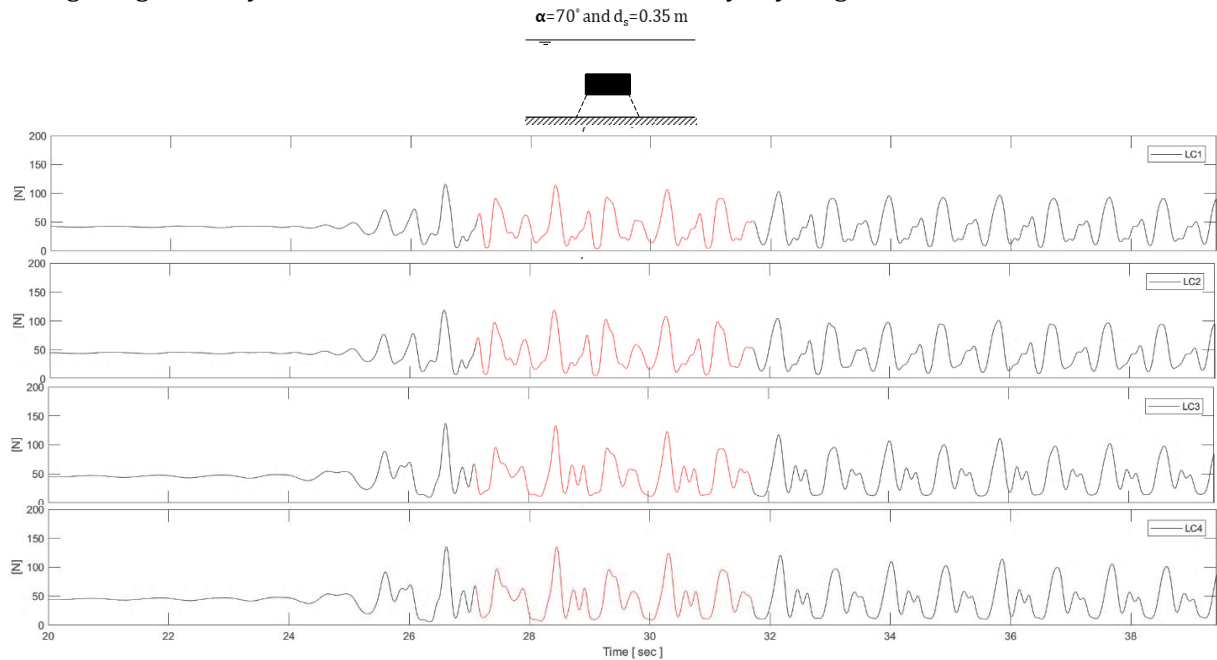


Figure 63: Example of a total tether force signals. For the condition of a submergence depth of 0.35 m and a tether angle of 70° (R14C_70)

For the condition of the smallest submergence depth of 0.175 m and a tether angle of 30° , for some tests zero tether forces and thus slack takes place. The test in Figure 64 shows clear slack combined with high snap forces. Tether 1 and 2 experience slack, tether 3 and 4 do not. However, the high snap forces in tether 1 and 2, are seen in tether 3 and 4 as well.

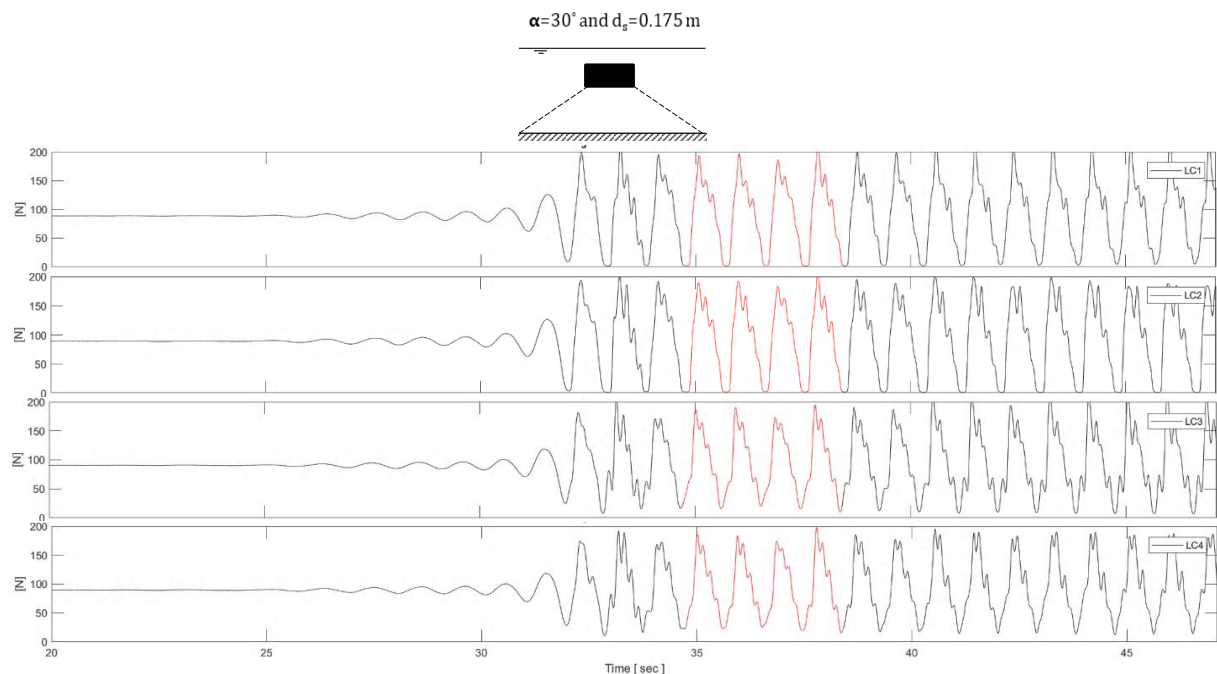


Figure 64: Example of a total tether force signals. For the condition of a submergence depth of 0.175 m and a tether angle of 30° (R14B_30), where slack occurs.

For scope of the present study only the tests with the smallest submergence depth of 0.175 m, combined with a tether angle of 70 ° and the smallest wave period (the steepest waves), results in zero tension forces, thus slack. For submergence depth of 0.35 m and a tether angle of 30 °, no slack is found but the large peaking force are found for the same steep waves. In Table 14 below an overview is given of the tests in which slack occurs.

Table 14: An overview of the occurrence of slack and snap

		Slack	'Snap' like peak*	'Snap' like peaks in Analysis Section*
<i>Configuration 1</i>	R12B_30	maybe	Yes	High Peaks
	R13B_30	yes	Yes	High Peaks
	R14B_30	yes	Yes	Yes
	R22B_30	no	<i>High Peaks</i>	<i>High Peaks</i>
	R32B_30	no	<i>±Harmonic</i>	<i>±Harmonic</i>
	R42B_30	no	<i>±Harmonic</i>	<i>±Harmonic</i>
<i>Configuration 2</i>	R12C_30	no	<i>Harmonic</i>	<i>Harmonic</i>
	R13C_30	no	<i>Harmonic</i>	<i>Harmonic</i>
	R14C_30	no	<i>Harmonic</i>	<i>Harmonic</i>
	R22C_30	no	<i>Harmonic</i>	<i>Harmonic</i>
	R32C_30	no	<i>Harmonic</i>	<i>Harmonic</i>
	R42C_30	no	<i>Harmonic</i>	<i>Harmonic</i>
<i>Configuration 3</i>	R12C_70	no	<i>High Peaks</i>	<i>High Peaks</i>
	R13C_70	no	<i>High Peaks</i>	<i>High Peaks</i>
	R14C_70	maybe	Yes	Yes
	R22C_70	no	<i>High Peaks</i>	<i>High Peaks</i>
	R32C_70	no	<i>High Peaks</i>	<i>High Peaks</i>
	R42C_70	no	<i>High Peaks</i>	<i>High Peaks</i>

* For some tests only the first peak is very large but the peaks after not ('Snap like peak'). While for other tests a long range of wave signals show snap like peaks ('Snap' like peaks in Analysis section')

Accelerations

The accelerations can be determined by two methods: from the accelerometers (method I) and by deriving the displacement signals from the video twice (method II). With an already noisy displacement signal, deriving it twice will lead to a peaky computed acceleration signal. Therefore, the accelerometers are used. However, first the accelerations from both methods are compared to see if the accelerometer signal can be validated by the accelerations found from the displacement signal.

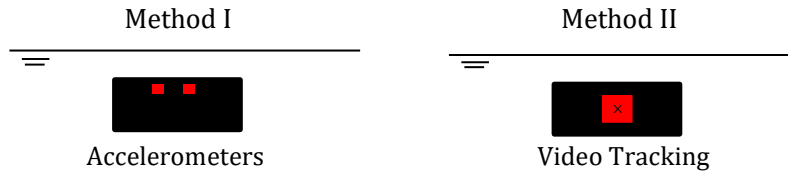


Figure 65: Schematisation of the two acceleration measuring methods. (I) the accelerometers signal, (II) the derivative of the video record of the displacement of the red marker.

Larger displacements with relatively small noise lead to the clearest computation of the acceleration from the displacement signal, Method II. Therefore the vertical displacements for the 70° tether angle configuration, having the largest displacement magnitude is used to compare with the accelerations from accelerometer. An example of two vertical acceleration signals from both methods is seen in Figure 66. The top graph gives the accelerometer signal, the bottom graph shows the derived acceleration in a dashed black line and the derived acceleration by only the dominant non-wave frequency component in red. It is clearly seen that the derived signal is quite peaky. The magnitude of the acceleration signal ('wave') height of the red section (of the top graph) is compared. Resulting in 1.12 m/s² for the accelerometer signal, and a value of approximately 0.8 m/s² for the derived signal. Applying the same procedure for the other waves types in this configuration leads to the differences between the two methods, presented in Table 15. This table shows that the difference in the accelerations found for the two methods lead up to 30%. That is a significant difference, indicating that the two methods can give different accelerations.

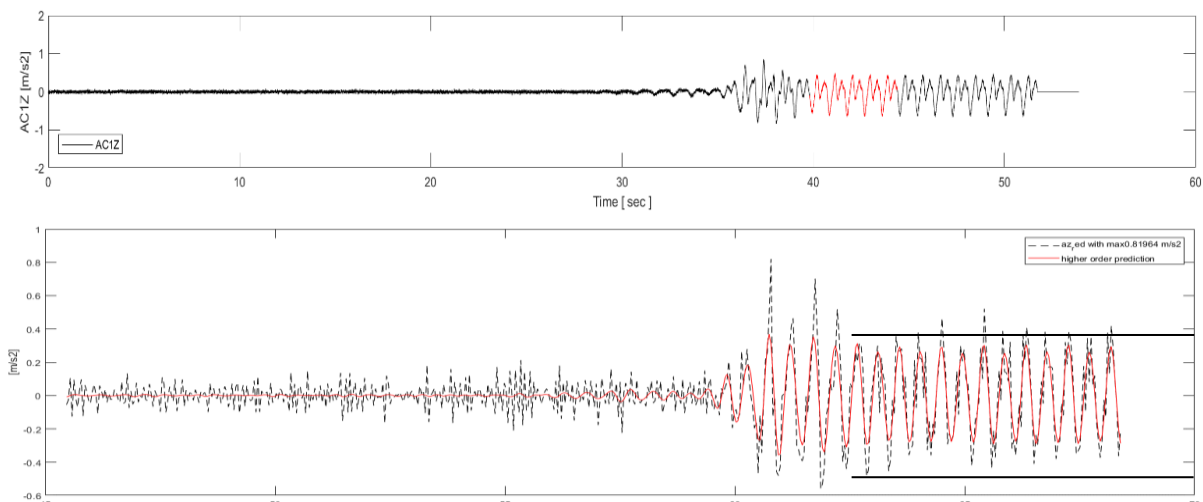


Figure 66: The vertical acceleration signal for the same wave (R12) from both methods: From the accelerometer (Method I), and derived from the displacement signal (Method II).

Table 15: The vertical acceleration signal 'wave' height from the accelerometers and from the computed acceleration. For configuration $\alpha=70^\circ$ and $ds=0.35$ m

Test ID	Mean AC1Z and AC2Z	Approximate ACZ from video	$\frac{\overline{ACZ}_{measured} - ACZ_{video}}{\overline{ACZ}_{measured}}$
R12C_70M	1,12 m/s ²	0.80 m/s ²	29%
R13C_70M	1,55 m/s ²	1.25 m/s ²	20%
R14C_70M	2,27 m/s ²	1.875 m/s ²	17%
R22C_70M	2,62 m/s ²	1.875 m/s ²	28%
R32C_70M	1,37 m/s ²	1.00 m/s ²	27%
R42C_70M	0,48	0.50	-3%

The deviation between the two methods can be explained by various reasons such as:

- Inaccuracies due to the double deviation of the displacement signal in Method II
- Inaccuracies in the spatial video calibration, giving errors in Method II
- The centre of the red marker indicated the centre of the model, but not necessarily the centre of rotation.

In the next sections the acceleration from the accelerometers is used to analyse the relationship between the acceleration and the wave parameters.

4.3.2. Response to a Regular Wave Conditions

In this section the relationship between the wave parameters and different response variables of the model is studied. Three different model configurations are analyzed to study the influence of the submergence depth and the tether angle on the relationship between the kinematics and the environmental conditions. The three configurations are shown in Figure 67.

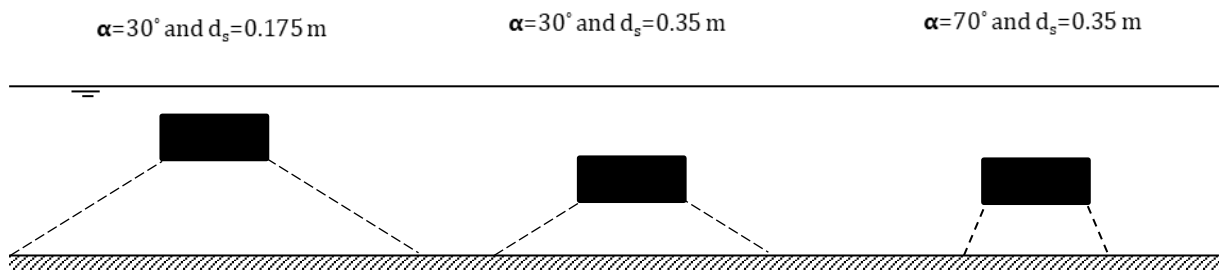


Figure 67: The three model configurations discussed in this paragraph. The submergence depths and tether angles are varied for these configurations.

Regarding the axis, in the data from the video, a positive displacement represents a movement towards the wave paddle. The movement in this direction is largest in magnitude for most of the tests. This is the axis definition opposite of what is used for all other instruments. For all other instruments the positive x-axis is directed toward the end of the flume.

Displacements

The first kinematic property to be studied, is the displacement of the model. For this analysis the displacement of the red marker on the model is used as it depicts the middle of both the vertical and horizontal dimension of the model. The middle of the red marker also depicts the centre of mass of the model. The location of the red marker is shown in Figure 68.

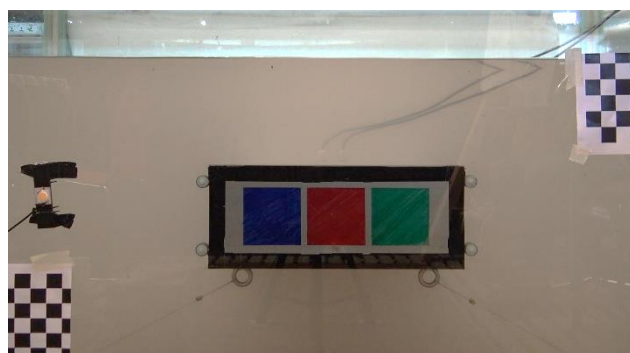


Figure 68: Picture of Markers on the model.

The displacements are presented in Figure 69. The horizontal displacement is marked by the dots (•) and the vertical displacement by the crosses (X). From this figure it is noticed that for a model with a 30° tether angle the vertical displacements are larger than the horizontal displacements, while for the 70° angle configuration the horizontal displacements are the largest. Overall, the largest horizontal displacements are found for the 70° angle configuration. For this configuration the natural frequency of the system lays in the range of the wave frequencies used in this test, especially for the horizontal direction. Therefore the magnitude of the displacements is magnified for these tests, compared to the of the other two configurations. An elaboration on the Eigen frequencies of the systems is found in Appendix D.

The shape of the relationship between the wave parameters, H and T, and the displacements looks very similar to the shapes found in Figure 40 for the hydrodynamic forces. Only in the relationship between the horizontal displacement and the wave period in configuration 1, some deviation in shape is found. This will be discussed in the next paragraph.

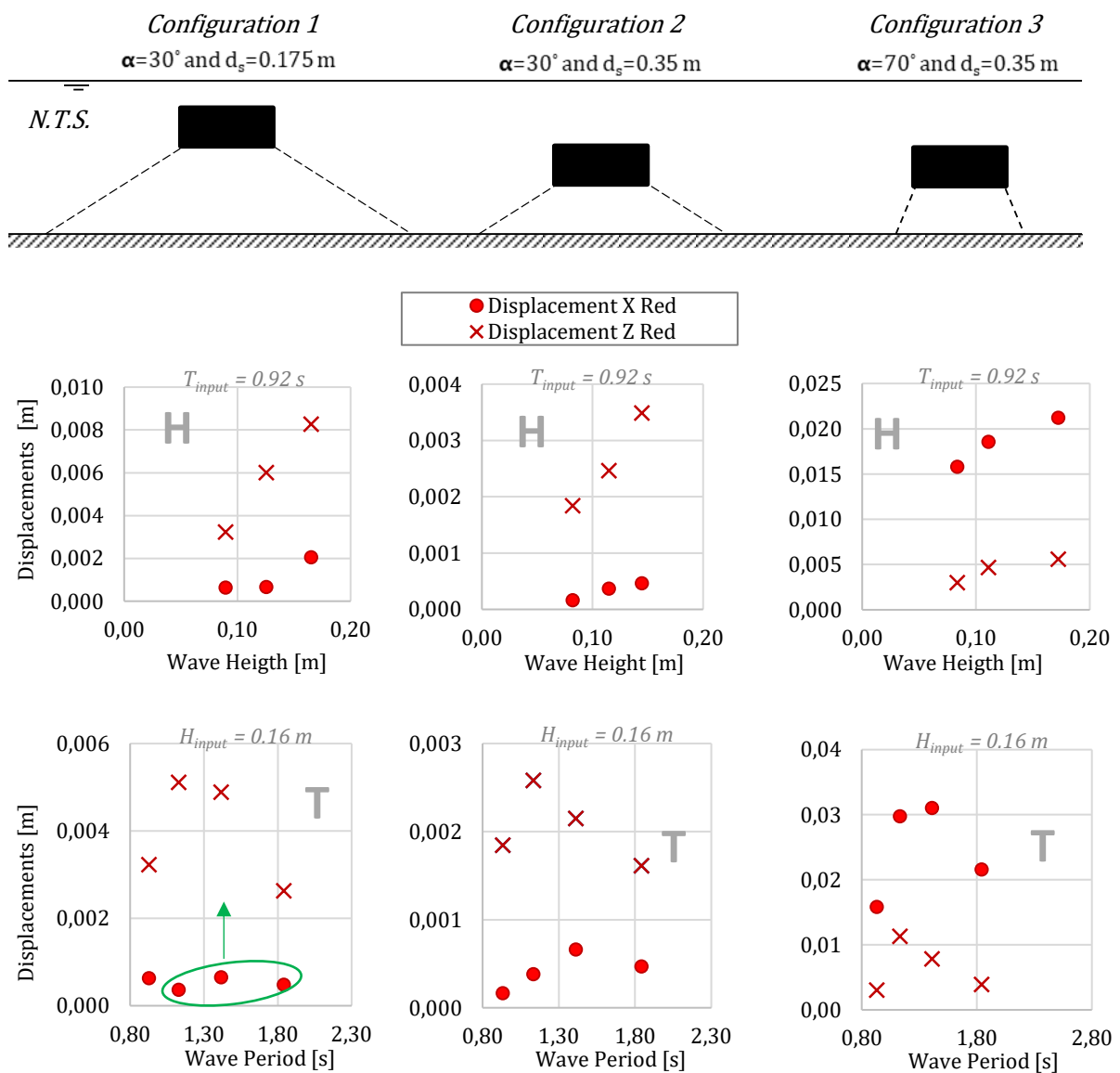


Figure 69: The wave parameters, H and T, and the vertical (X) and horizontal (•) displacements of the model for the three model configurations with varying submergence depth (0.175 m and 0.35 m) and tether angle (70° and 30°).

To discuss the data points in the green ellipse in Figure 69, Figure 70 is used. This figure shows Matlab CWT (continuous wavelet transform) graphs for the two waves, R32 and R42, with the largest wave period of configuration 1. The wave frequencies lay around 0.71 Hz and 0.54 Hz, respectively for R32 and R42, depicted by the lowest band in both graphs. The horizontal displacement in the two left graphs show a frequency band at a higher frequency that is dominant or significant for the displacement. While for the vertical displacement in the right figure, the wave frequency is the only significant frequency. Appendix E, gives a full overview with tables about the dominance of frequency bands found in the various signals of the tether tests. To conclude, the of a higher frequency band in the horizontal displacement of configuration 1 result in smaller displacements than expected.

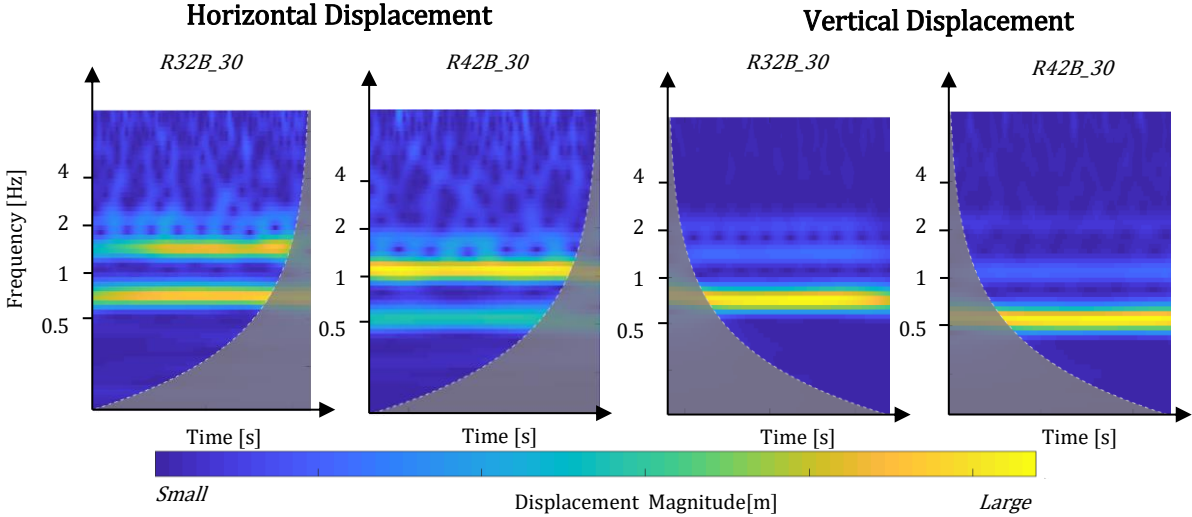


Figure 70: CWT-graphs of the horizontal displacement (left) and vertical displacement (right) for the same waves (R32 and R42) for configuration $\alpha=30^\circ$ and $ds=0.175$ m. ($f_{wave}\approx 0.71$ Hz & $f_{wave}\approx 0.54$ Hz)

Going back to Figure 69 the influence of the submergence depth can be analysed by comparing the left and middle graph. It is found that for both directions the displacements are larger for a smaller submergence depth. This seems reasonable, since for the fixed model in section 4.3 it was found that larger hydrodynamic forces are found for a smaller submergence depth. This is because higher in the water column the orbital motions are larger, giving larger displacements.

Accelerations

For the study on the relationship of the wave parameters on the acceleration of the model, accelerometer 1 is chosen. The results plotted in Figure 71 are the mean amplitude values of a chosen signal section. The largest accelerations of the model are found for the configuration 1 with 30° tether angles and a submergence depth of 0.175 m. This is in contrast to the largest displacements which were found for configuration 3 in Figure 69. Table 14, showed how slack and snap forces (except for one test in configuration 3) only occur for configuration 1. If snap and slack come with large acceleration peaks, this explains why the magnitude of the accelerations in configuration 1 are larger than for configuration 3, even though smaller displacement magnitudes were found in Figure 69.

Further, it is noticed in the frequency analysis in Appendix E, that for configuration 1 and 2, the R12 tests are dominated by the wave frequency, while other tests with the same wave height but larger wave periods, also significant higher frequency bands are seen. The R12 tests are marked with the red ellipse in Figure 71. So, wave frequency dependency indicates larger accelerations for these tests. This explains why the marked tests show a larger acceleration than would be expected from the familiar wave period curve, found in Figure 40 and Figure 69.

Two other points that stand out, in Figure 71 are the accelerations marked with the orange dashed line in for configuration 3. For this test (R22) the largest snap force peaks are found compared to the test for the other wave periods. This could be because this wave is closest to the eigen period of the system.

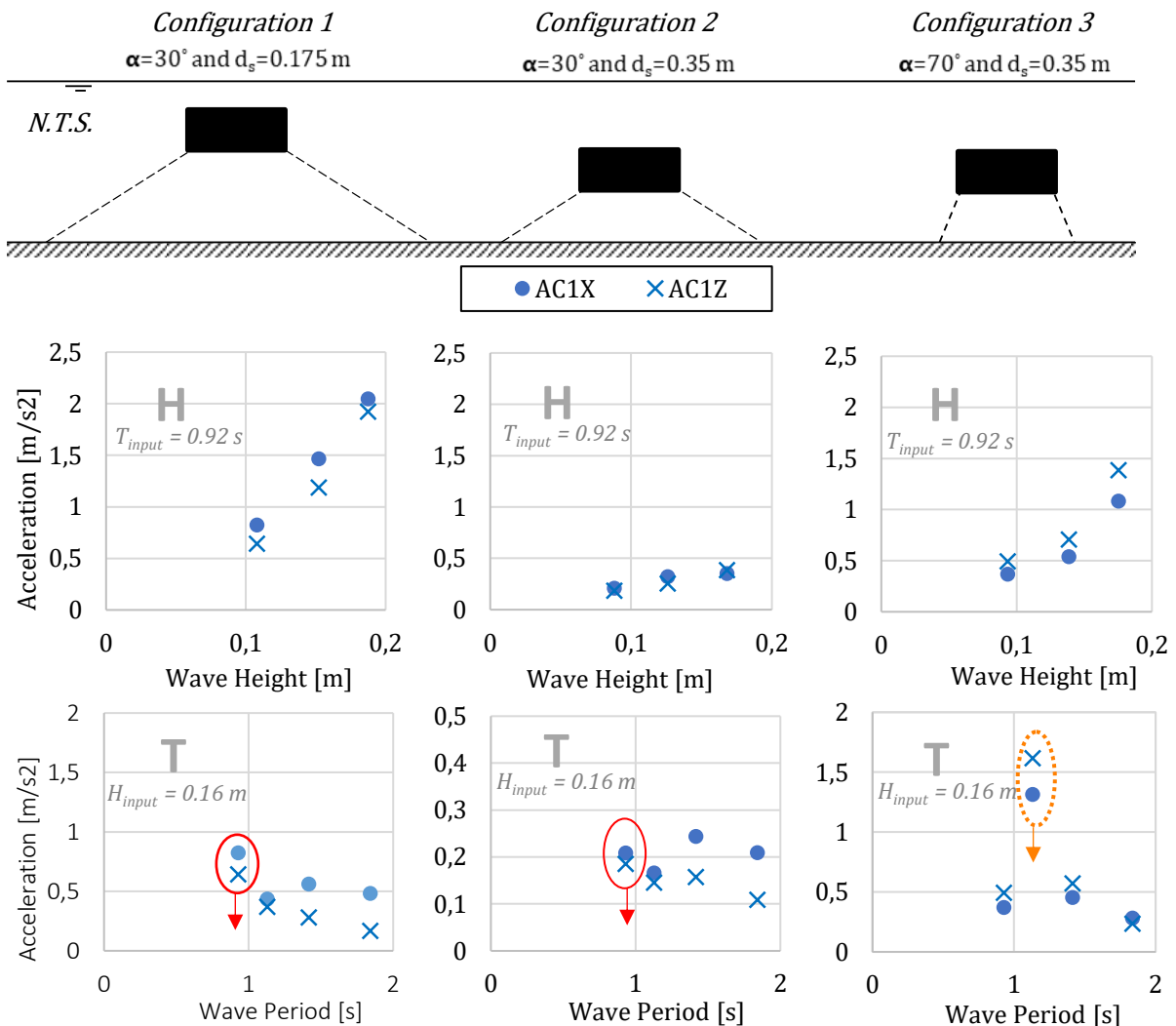


Figure 71: The wave height and the vertical (crosses) and horizontal (dots) accelerations of the model for the three model configurations with varying submergence depth (0.175 m and 0.35 m) and tether angle (70° and 30°).

Tether Forces

Last, it is studied how the forces in the tethers respond do different environmental conditions. Figure 72, shows the mean maximum and mean minimum amplitudes of the forces in the tethers for an increasing wave height. The initial tensions forces in the tethers are removed to find these fluctuating forces. An example of a tether signal and the initial and fluctuating tension forces are presented in Figure 73. The same relationship conclusions can be taken as for the wave parameters and the accelerations:

- The largest tether forces are found for configuration 1, where most slack and snap occur.
- The shape of the relationships are defined similar to Figure 40
- In configuration 3, a large force is found for $T \approx 1.13$ s, because of snap forces
- A larger submergence depth results in smaller tether force, because of reduced wave motions
- A larger tether angle results in larger tether forces.

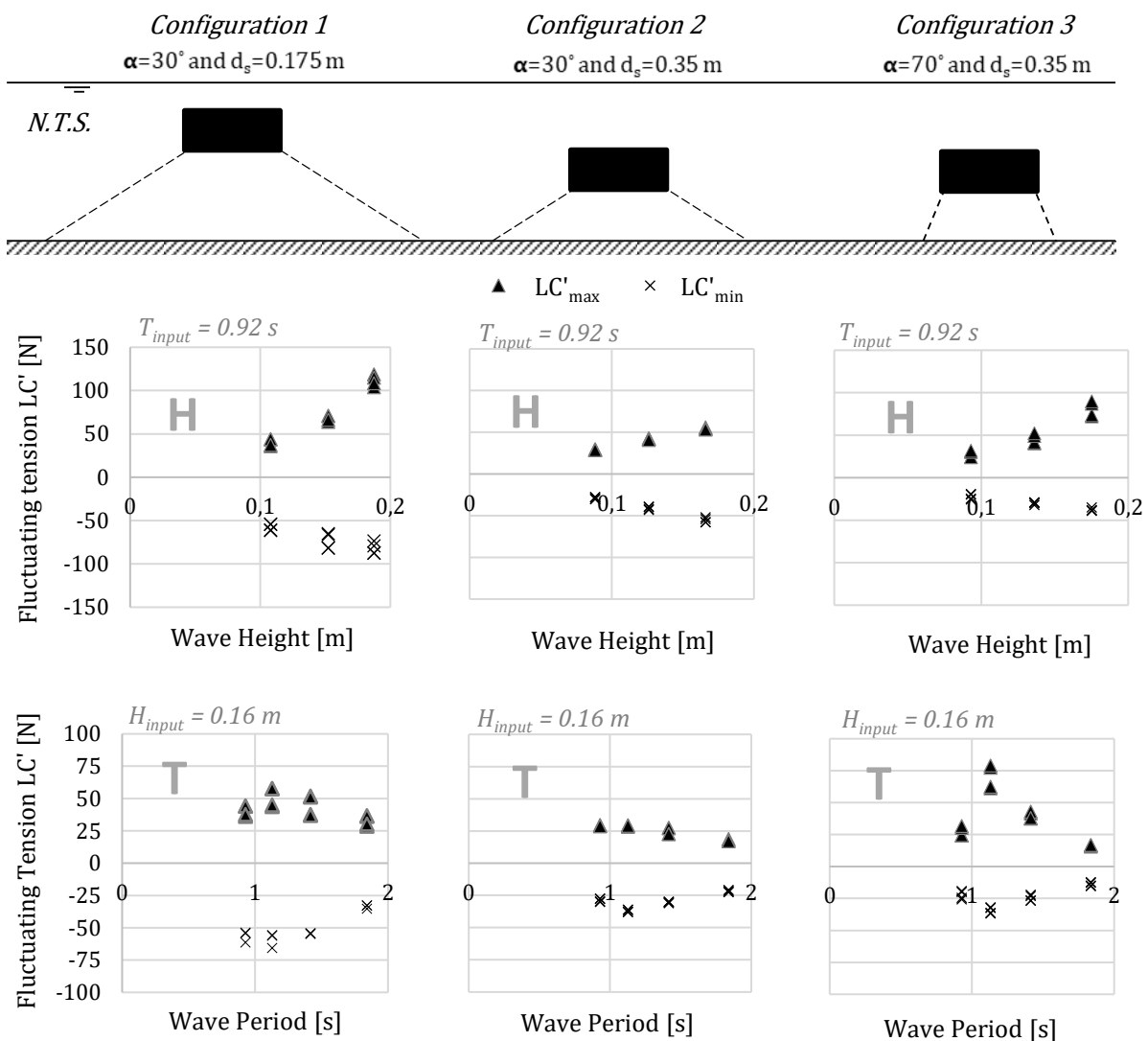


Figure 72: The fluctuating tether forces for increasing wave period for different model configurations ($T=0.92$). Left) tether angle $\alpha=30^\circ$ and $d_s=0.175$ m, middle) $\alpha=30^\circ$ and $d_s=0.35$ m right) $\alpha=70^\circ$ and $d_s=0.35$ m

Besides these findings a few new aspects are noticed in Figure 72. For most tests the maximum amplitude value (the signal peak) of the tension force is larger than the minimum amplitude (the signal trough). This is the case for most tests, except in configuration 2, there the maximum and minimum amplitude are of approximately equal magnitude. The reason that a difference in magnitude is found in the other 2 configurations, followed by a trough smaller in magnitude. Figure 73, is an example of such a test which shows steep and short maximum peaks and longer less steep troughs in the signal.

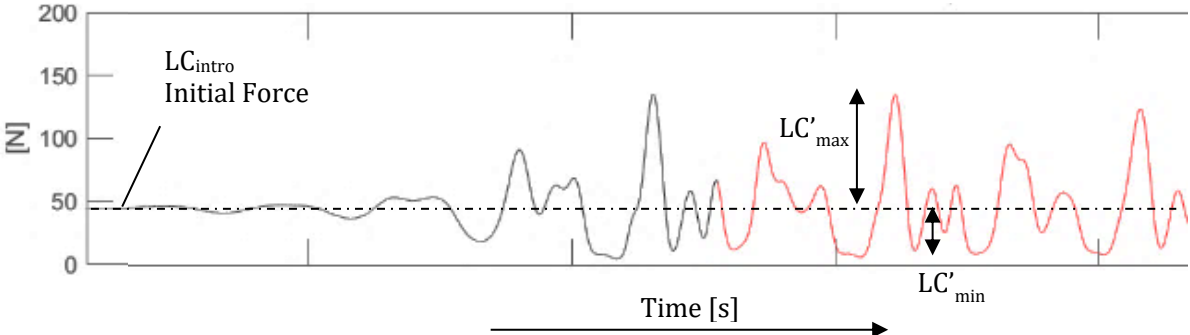


Figure 73: Example of a tether force signal and definitions of the variables. From (R14C_70)

4.3.3. Force prediction by Morison

In section 4.2.2, it was studied how well the Morison equation was able to predict the forces measured on the model for a fixed model. In this section the same prediction method, with the same Morison force coefficients, is used to see how well the Morison equation can predict the resulting net horizontal and vertical tether force components. The following expressions for the resulting horizontal and vertical force components will be used:

$$LCX(t) = \cos \alpha [LC2'(t) + LC1'(t) - LC3'(t) - LC4'(t)]$$

$$LCZ(t) = \sin \alpha [LC2'(t) + LC1'(t) + LC3'(t) + LC4'(t)]$$

Where:

- LCX : The resulting horizontal force component off all tethers combined [N] or when divided by the model dimension [N/m]
- LCZ : The resulting vertical force component off all tethers combined [N] or when divided by the model dimension [N/m]
- $LC1'$: The fluctuating part of the tension force in tether 1 at the front side of the model [N]
- $LC2'$: The fluctuating part of the tension force in tether 2 at the front side of the model [N]
- $LC3'$: The fluctuating part of the tension force in tether 3 at the back side of the model [N]
- $LC4'$: The fluctuating part of the tension force in tether 4 at the back side of the model [N]
- α : The input tether angle [rad]

These will then be compared to the hydrodynamic forces determined with the Morison equation found in the following equation:

$$LCX(t) = F_{x,morison}(t)$$

$$LCZ(t) = -F_{z,morison}(t)$$

Figure 74, shows for both force directions, this comparison of the measured resultant tether force and the predicted Morison Force. Table 16, shows the mean error between the predicted and measured force, and the standard deviation from the mean error, for the three configurations. In the following paragraph the results for the X direction and for the Z-direction are discussed.

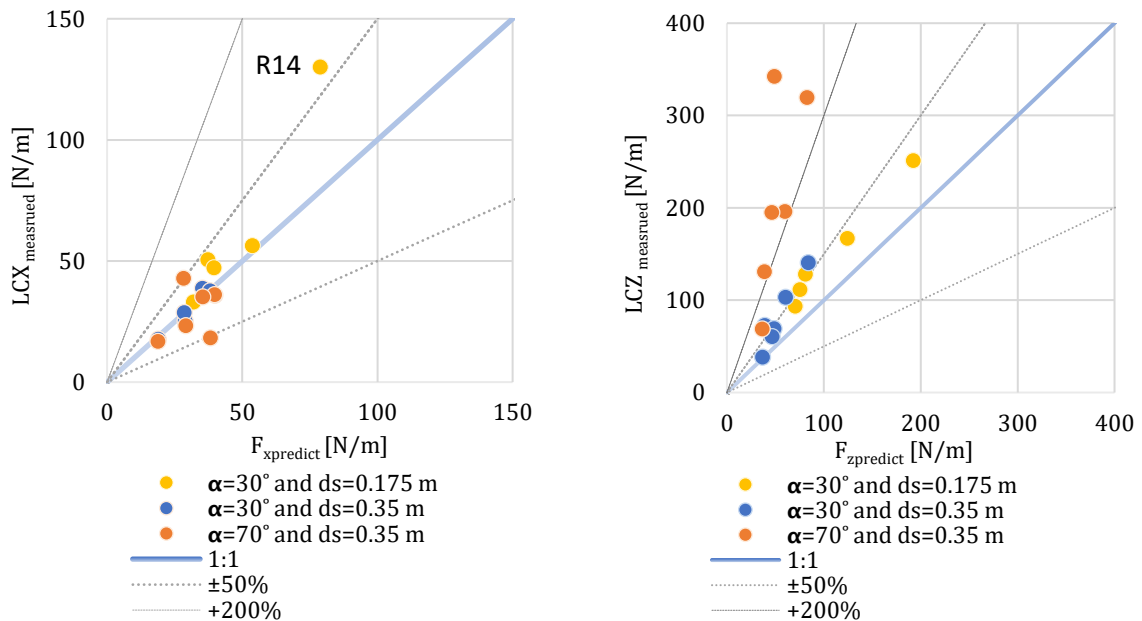


Figure 74: the horizontal net resultant tether force (a, left) and the vertical net resultant tether force (b, right), plotted with the predicted horizontal and vertical Morison Force.

Table 16: The mean error factors and standard deviations for the prediction by the Morison.

	$\overline{R_x}$	σ_x	$\overline{R_z}$	σ_z
$\alpha=30^\circ$ and $d_s=0.175$ m	1,26	0,23	1,41	0,11
$\alpha=30^\circ$ and $d_s=0.35$ m	0,97	0,08	1,43	0,16
$\alpha=70^\circ$ and $d_s=0.35$ m	1,05	0,25	4,52	1,28

X-direction

From Figure 74 and Table 16 is seen that the largest error comes from configuration 1. This is mainly due to the large error coming from the R14 wave type, for which the largest slack and snap effect were found. The error R for configuration 1 without this wave, would be only 1.15. The prediction by the Morison force for prediction in configuration 1 is well, with a small error and small deviations in the errors. For configuration the mean error is 1.05. However, the standard deviation of the error is large, 0.23, indicating that the spread in the errors is large for this configuration. To get a better understanding of the of the spread, the errors of this configuration are presented per wave type in Table 17.

Table 17: The mean error factors and standard deviations for the prediction by the Morison per wave. For configuration 3, with $\alpha=70^\circ$ and $d_s=0.35$ m

	R_x	
R12C_70	0,89	
R13C_70	0,80	Short wave
R14C_70	0,91	Short wave
R22C_70	1,51	Snap forces
R32C_70	0,99	
R42C_70	1,02	Long wave

Table 17, shows that an large under prediction by the Morison force is found because of the large snap force found for this wave type (R22). This is the wave type closest to the Eigen frequency of the system. The largest over prediction by the Morison force are found for the wave types R13 and R14. These waves are the only two wave in the analysis of this study, for which the waves are breaking on the model. Because the back side of the model does not experience a full wave but a broken wave, the forces in the tethers are smaller than expected.

Z-direction

From Figure 74 and Table 16 is seen that the prediction of the vertical force is of bad quality, with large under predictions, indicating that the vertical force is not well predicted by the Morison equation. That the errors are larger for configuration 1 and 2 can be explained by the fact that the vertical displacements are larger than the horizontal, see Figure 69. As more motion is involved the prediction by the Morison equation made for a fixed structure, fits less well.

The largest error is found for configuration 3. For this configuration the largest displacements were found, making this the least fixed system. Because of these large displacements the tether angle deviates most from the input tether angle α , which is used in the expressing of the resulting tether force components on the previous page.

$$\frac{LCZ}{LCX} = \tan(\alpha)$$

Figure 75, gives an example of a very bad approximation by the Morison force (red) compared to the vertical measured resulting tether force (blue) in the left graph. The right graph shows a very good prediction of the horizontal force Morison force (red) and the measured resulting horizontal tether force (blue).

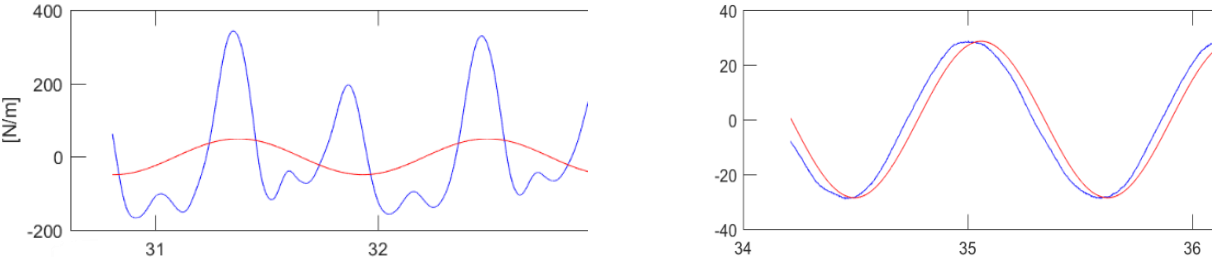


Figure 75: Blue is measured tether force resultant, red the prediction by the Morison force. Left (R22C_70 Z), right (R22C_30 X)

4.3.4. The Answer to Research Question 2

In this paragraph, conclusions are drawn for research question 2 based on the findings of the previous paragraphs. Research question 2 was formulated as follows:

Research Question 2

What are the kinematic model response and the force tether response of a tethered rectangular cylinder subjected to a regular wave environment in small scale flume experiments? And what is the influence of the structure submergence depth and tether angles on these responses

The response of the model are discusses per kinematic variable:

Displacements

The relationship between the wave height and the displacements resembles the relationships between the wave height and the hydrodynamic forces found for the fixed model in section. For configurations with a 30° tether angle the vertical displacements are larger than the horizontal, while for the 70° tether angle configuration the horizontal displacements are largest. A larger submergence depth is found to give smaller displacements in both directions. This seems reasonable, since deeper in the water column smaller wave motions are found. Studying the influence of the tether angle it is seen that a larger tether angle gives larger displacements.

For the displacements and the wave period, the relationship also generally resembles the acceleration related shape as found for the hydrodynamic forces. Only the relationship with the horizontal displacement of the 30° tether angle configuration and 0.175 m submergence depth seems to deviate a slightly for the largest wave periods. This can be explained by the significance of high order frequency bands in the horizontal displacements of these tests.

Accelerations

First of all the accelerations from the accelerometers and the accelerations from a double differentiated displacement signal are compared and found not to be convincingly of the same order of magnitude. The accelerations from the accelerometers are chosen to use for the analysis of the relationship to the wave parameters. For the relationship with the wave height, a fairly linear relationship is seen for the configurations. The accelerations do not vary much between the vertical and horizontal direction. Even though the largest displacements were found for the 70° tether angle, the largest accelerations are found for the 30° tether angle with the smaller 0.175 m submergence depth, configuration 1. In this configuration slack and snap forces occur the most, causing large accelerations. In configuration 3 for one test the wave frequency comes close to the natural frequency of the model system, resulting in larger accelerations as well.

Tether Forces

Next the fluctuating part of the tension forces in the tethers was studied. the shapes of the relationships between the wave parameters are similar to the linear and curved for respectively the wave height and wave period, found for other kinematic properties. The conclusions drawn for the tether forces are the same as for the accelerations. The same effect of snap forces and eigen frequencies is seen.

In the last section. the resulting net components of the forces in vertical and horizontal direction were compared to the predicted Morison forces for a fixed model. In general the Morison force predicts the resultant tether forces best for configuration with 30° tether angle and 0.35 m submergence depth. This makes sense, because the magnitudes of all kinematic properties were smallest for this configuration, making it resemble most a fixed model. However, for the vertical force prediction, large overestimations found. So overall the force prediction by the Morison equation is only found to be reasonable for the horizontal force of the 30° tether angle and 0.35 m submergence depth configuration, with a mean error of 3% and a small standard deviation from this mean error.

5

Discussion

The next chapter covers a discussion of the present study. By evaluating the methodology and the interpretation of the results, the significance of the findings of the present study is explored.

The Inflow of Current

For the present study a current was generated by pumping water from the basement basin into the wave flume. No special measures were taken to create a smooth inflow of current. It is common to use structures like a honey comb to smoothen the inflow for flume experiment with only current. Unfortunately for the present study this could not be done, because for the case of combined waves, the wave field created by the wave generator would be severely disturbed when it would encounter such a structure. As a result, the inflow of water was not smooth and disturbances were seen clearly in the tests including waves. Figure 76 and Figure 77 portray the two different conditions. The red dashed line shows the wave amplitude values expected from linear wave theory and the input wave height. For the regular wave case with no added current, in Figure 72 a nice harmonic water elevation is found. For the combined current and wave case, in Figure 73 a wavy signal is found that often deviates significantly from the dashed lines. To create a smaller difference between the theoretical linear wave theory measurements and the real measurements, measures could be taken to smoothen the inflow and create less disturbances. Research has been done on the effect of different types of inflow on the current that is developed. Suggestions made, for example, in the paper by Robinson (2015) on this topic, can be used to make adjustments to the flume design.

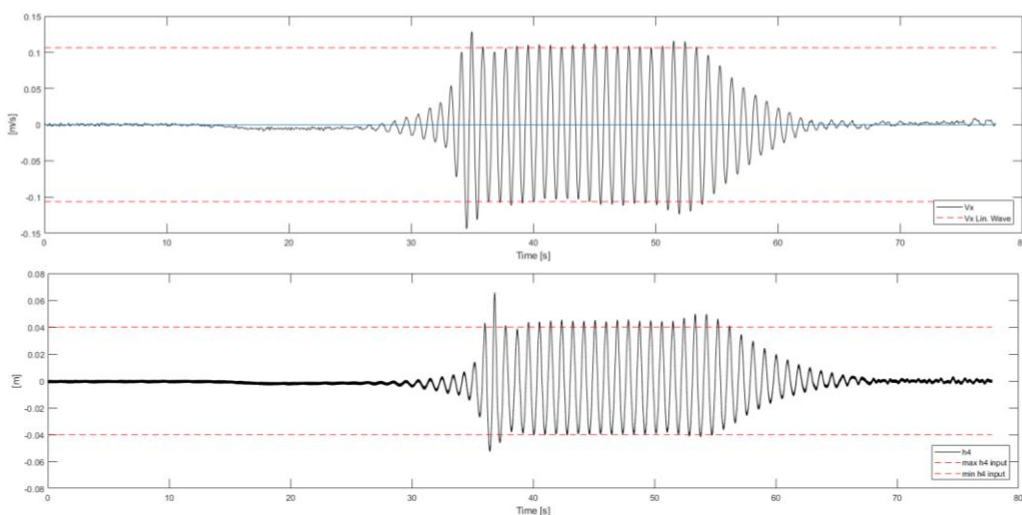


Figure 76: The horizontal velocity and wave gauge signal of a regular wave (FR12C)

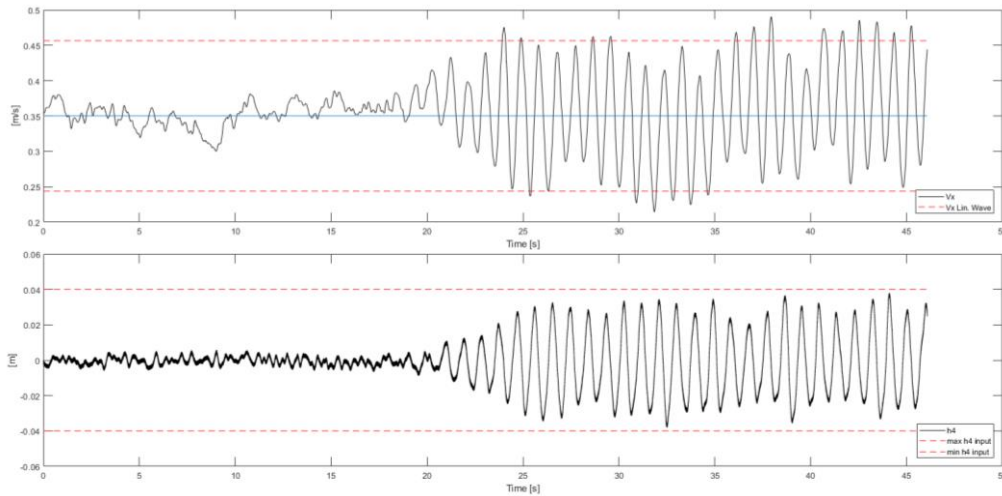


Figure 77: The horizontal velocity and wave gauge signal of a combined wave-current (FRC123C)

For the velocity signal it are these linear wave theory values of the amplitude that are used for the study on the Morison coefficients. If these are indeed an over prediction of the real velocity, different relations between the force and the velocity would be find if the real velocity were to be used. Which would again result in different values for the Morison coefficients.

Velocity Depth Shift Computations

In section 3.4.2 on the Depth Shift, it was shown that in the present study for the analysis part of tests including waves, not the measured amplitude velocities are used but the linear wave theory orbital particle velocities. However, in Figure 38 it was found that for tests with combined waves and current, the velocities measured at a depth of 0.2 m gave values that are significantly smaller than linear wave theory suggests. Still, the linear wave theory values for the model depth are used in the computation of the Morison force coefficients. In general, the measured velocity amplitudes, and thus the accelerations, are lower than the used velocities and accelerations. Looking at the Morison equations this suggests that in general larger coefficients are expected if the real, smaller, velocities were to be used. The significance of this over-prediction of the velocity on the coefficients can be studied by rerunning some of the Morison analysis.

As this difference in velocity might turn out to be significant, for future studies it can be tried to prevent this difference from being there in the first place. For example, the velocity can be measured at the depth of the model instead of at a smaller depth. Then for the analysis part, the mean velocity of the measured waves can be used to compute the Morison equation. Because of this, any reductions in the velocity amplitude due to a coexisting current is better accounted for.

Velocity Time Shift Computations

Besides the depth shift, a time shift was applied to the velocity record as well. The function of this shift was to account for the delay in time which is found for a wave to travel from the EMS, where the velocity is recorded to the middle of the model. The wave propagation speeds found between two wave gauges was used to calculate this time shift from the known spatial shift. However, in the discussion of the results it was found that in an inertia dominated KC-regime, the drag is significantly influenced by this shift due to its sensitivity. It can lead to an opposite sign of the drag force. Except for the sign, the magnitudes for the drag coefficients were found to be similar to those found by Venugopal in his two studies (2008) (2006). This hints at the explanation that the time shift method differs from the method he used, causing the acceleration peak and the force peak to have phase shift of opposite sign.

The fact that for the KC range of the present study the drag is found to be sensitive and the inertia found to be relatively unaffected by the phase shift between the force and the velocity signal, is for example confirmed by (Hudspeth, 1988). Besides, the small Dean eccentricity parameter values of no larger than 0.2 found in the present study indicate an inertia dominated regime.

In Figure 78 two graphs are presented. Both graphs show the same wave test. In the left graph the applied time shift, Δt , relative to the wave period T , is varied to study the influence of the time shift on the outcome of the inertia coefficient, of both directions. The same is done in the right graph, but then for the drag coefficients. In both graphs the force coefficients values for a phase shift of 0, marked with a red dot, depict the value that was presented in the results chapter in section 4.2.1. Before was discussed how different studies found similar drag coefficients, but with an opposite, non-negative sign. Studying the right graph, this could imply that the phase shift in other studies a negative, compared to my reference at 0. If the same holds for the inertia coefficient, this would lead to equal, maybe slightly larger inertia coefficients.

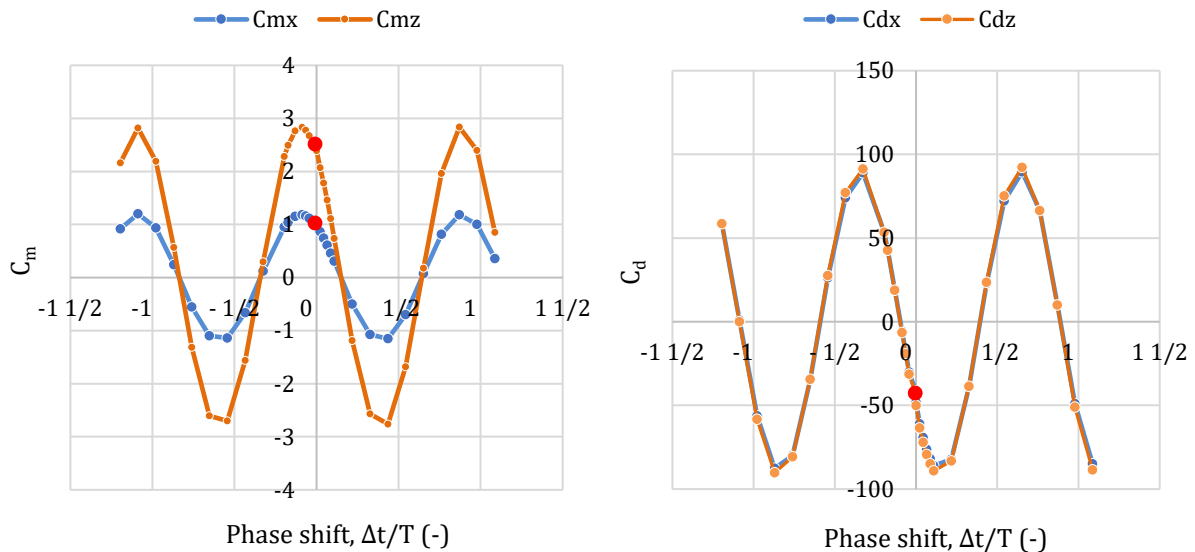


Figure 78: The influence of the velocity time shift on the Morison force coefficients. The used coefficients as red dot.

In general, looking at the inertia graph In Figure 78, it is seen that for this test the inertia coefficient is also sensitive to a the phase shift. Especially the vertical inertia coefficient has a steep slope for slightly larger time shifts, Δt . To conclude, the drag is very sensitive to the time shift, but for the inertia coefficient it can be significant as well.

Velocity Time Shift for a Moving Model

The discussion on the time shift is discussed a little bit further for specifically the tether model tests. For these tests, the same time shift method is applied as for the fixed model. In this way, the shift remains based on the spatial difference between the EMS and the centroid of the non-displaced model. However, when the model starts to displace itself in a wave field, this spatial difference changes as well. In the results it was found that the phase shift between the force and acceleration changes, contributing to a worsened prediction of the force by the Morison equation. For future research with a displaced model, it is advised to look for an alternative way of applying a time shift to the velocity signal or looking for an alternative way of using a velocity record in general.

Combining the Wave and Current Components

In computing the velocity for a combined wave-current environment the only current component is added to the linear wave theory orbital water particle velocity component. This method of computing a velocity for the combined situation, neglects the influence of the effect of the coexisting current on the development of the waves. In section 4.1.1 it was shown how the current effects the amplitude of the orbital water particle velocities as well as the magnitude of the wave height. The used velocities are generally higher than the reduced velocity, in case of an added current component to a wave field. This has an influence on the force coefficients found in the Morison equation.

Wave Size Compared to Model Size

Another aspect, which has not been discussed so far is the size of the model with respect to the size of the wave. In the methodology the wave motion is approached as a point object, like in the drag and inertia forces. While in reality some averaging of the whole motion over the whole model is done, because the model is of significant size. The width and height of the model are 0.40 m and 0.16 m respectively. The wave length ranges from approximately 1.30 m to 4.7. Thus the wave lengths are larger than the model dimensions, but especially for the smallest waves the presence of the model is not negligible for the water motions.

Lift Forces

The lift force is normal to the vector of the velocity and due to the orbital motion of the water it will rotate round the model axis. Too little of the lift force is known in the present study, no magnitude no direction or period, so the force is not accounted for in the Morison equation. Previous research (Chaplin & Subbiah, 1997) has demonstrated that this translates into noise in the drag and inertia force components.

Tether Force Distribution

When preparing the set-up of the tether model tests, the distribution of the force over the 4 tether cables was found to be very sensitive. Increasing the tension in one tether influenced all other tethers simultaneously. This made it hard to establish perfectly equal distributed tether force of equal magnitude. As a result, the tension in the forces vary up to approximately 2 N between the different tethers.

Besides the initial tension forces varying at the start of the tests, it was also found that during the tests the initial force could change. These changes were of a couple of Newtons. This might be due to the fact that when large forces are found, accompanied with slack and snap, the attachment point of the tether to the load cells was slightly turned, increasing or loosening the tension in the cable. Therefore, it is advised for future studies to design a set-up in which a tension adjustment mechanism is created that does not allow for any changes in tension during the tests.

Measurement Inaccuracies

When using the set-up, different aspects of the set-up can influence the results. A few of these aspects will be mentioned. The water level in the flume deviated up to 1.0 centimetre, due to a water level very sensitive to the weir height and the opening valve of the inflow, mainly for the tests including current. In processing the results, the water level is assumed to have a constant level of 0.7 m water column. This assumption results in orbital water particle velocities that are a little bit higher or lower than in reality, due to the lower or higher water level. An error in velocity of a couple of cm/s is the result. However, for the fixed model tests on which the analysis of the forces and Morison coefficients is based on, the water level was 0.7 m so that does not play a role. For the other tests that were done but not being analysed in this study, this should be kept in mind.

Another measurement inaccuracy is the offset of the velocity. When the velocity is processed into the unit of m/s, the value in Volt recorded at a still water level of 0.7 m is subtracted first. During one of the testing days this was done at the start and ending of this testing day. The voltage found deviated between these moments of the day. When processing the data, only one velocity offset value is applied, usually measured at the start of the testing day. If the deviation of the voltage offset is too large it can result in a significant inaccuracy. For this specific day on which this was noted within half an hour an offset difference of approximately 0.002 m/s was measured. It must be mentioned that this was on a particular hot day with fast rising temperatures. The amount of difference found on this day is not too large, however, it is advised to check the velocity offset at least twice a day.

Additionally, inaccuracies can occur in the calibration methodology of the video processing. The spatial calibration applied in the video processing based on drawing a line of the width of the model on a snapshot of the video. The pixels are counted and the ratio between m and amount of pixels, is used for the rest of the video processing into displacements. The selection of pixels in the calibration is not highly accurate, not on the scale of mm. While for mainly the 30° tether angle configurations, the displacements found for the horizontal direction are smaller than 1 mm. Therefore it should be kept in mind that the smallest displacements relatively have the most influence of possible calibration errors.

Scaling Effects

In chapter 3 is shown how Froude scaling is applied in the present study. However, the Reynolds number is not scaled. Meaning scaling effect might be found. On the contrary, it is known that cylinders with sharp edges are little sensitive to the effect of Reynolds numbers. For conditions including waves, it was found for square cylinders by Venugopal (Venugopal, 2006), that the β -factor (including the Reynolds number) showed to be of little influence. Leading to the suggestion that the force coefficients are not significantly affected by the Reynolds number.

6

Conclusions and Recommendations

In this chapter the final thoughts on this study are presented. The study is concluded by reflection on the research objective and research questions, and by making recommendations for future research on the topic of this study. In the reflection the results from chapter 4 and the discussions from chapter 5 are used.

The following research objective was given for this study:

To perform small scale flume experiments to develop a better understanding of the effect of the hydrodynamics from a wave, current and combined wave-current environment on a submerged floating tunnel.

Based on this objective two main research questions were formulated:

1. *What is the relationship found between environmental parameters and the hydrodynamic forces on a fixed small scale tunnel element and how well can these forces be predicted?*
 - a. What is the relationship between the environmental parameters; wave height, the wave period, current velocity and submergence depth, and the hydrodynamic forces on a fixed rectangular cylinder in small-scale flume experiments subjected to regular wave, current and combined wave-current conditions?
 - b. What is the hydrodynamic force prediction accuracy of the Morison equation for a fixed rectangular cylinder in small-scale flume experiments subjected to regular waves and combined wave-current conditions?
2. *What are the kinematic model response and the force tether response of a tethered rectangular cylinder subjected to a regular wave environment in small scale flume experiments? And what is the influence of the structure submergence depth and tether angles on these responses?*

The research questions are discussed one-by-one.

1.a. *What is the relationship between the environmental parameters; wave height, the wave period, current velocity and submergence depth, and the hydrodynamic forces on a fixed rectangular cylinder in small-scale flume experiments subjected to regular wave, current and combined wave-current conditions?*

Regular waves

The tests performed in the present study result in hydrodynamic forces that are dominated by the acceleration-related inertia force component. As a result, the shape of the relationship found between the parameters and the force, is well determined by the shape found for the relationship between the wave parameters and the accelerations. For the magnitude of the hydrodynamic forces another aspect is of importance. The vertical water motion is more distorted by the presence of the model, because the model dimension normal to the vertical axis is larger. Besides this larger projected area for the motion, the water has to come from below and there is a layer of water on top of the model. As a result, the vertical hydrodynamic force is larger than the horizontal hydrodynamic force, even though the horizontal water particle accelerations are larger than the vertical. As for the influence of the submergence depth on the hydrodynamic forces, it is found that a smaller submergence depth gives larger hydrodynamic forces in all cases.

Current

As expected, the horizontal hydrodynamic force in case of an only-current condition, is increasing non-linearly for an increasing current velocity. An increase of the submergence depth does not show a significant effect on the hydrodynamic force.

Combined Wave-current

When a current is added to a wave environment, the wave height is reduced and the wave period. Specifically for the shortest wave type, it is noticed that the computation of the horizontal velocity via linear wave theory with the input wave height, gives the worst prediction of the measured velocity. In general, for all wave types, the error between the measured horizontal water particle velocity and computed horizontal velocity increases for an increasing added current. For the computation of the vertical water particle accelerations for large added currents, errors of double the magnitude, close to 30% are found.

The shape of the relationship between the wave parameters and the hydrodynamic force remains fairly similar to the shapes found for regular waves only. As the added velocity increases, the horizontal hydrodynamic force increases. This is because the velocity related drag part of the forces increases in importance to account for the non-zero force baseline. For the vertical hydrodynamic force, the influence of an added current is at first not significant. However, for the largest two added currents larger vertical forces are found for the same wave height. This is because the horizontal water velocity is also present in the expression of the vertical force. While the vertical force baseline remains at 0 N/m, this does result in an increase of the magnitude of the vertical force amplitude.

1b. *What is the hydrodynamic force prediction accuracy of the Morison equation for a fixed rectangular cylinder in small-scale flume experiments subjected to regular waves and combined wave-current conditions?*

The forces found in the present study were compared and validated by comparing drag coefficients for the only current tests. The drag coefficients of the present study are very comparable to the values found in other studies. The inertia coefficients in case of a regular wave and combined wave-current conditions are similar to those found by Venugopal (2008). For the lowest KC numbers the drag coefficients are opposite in sign, but similar in magnitude. The negative drag coefficients are the result of the time shift applied to velocity signals to compute the water velocities at the model. The negative drag coefficient suggest that compared to e.g. the study by Venugopal (2008) a larger shift is applied in the present study. As a result the drag coefficient of this study are a negative and the inertia coefficients can be equal or slightly lower in value. The influence of the phase shift force coefficients has also been studied by Hudspeth

(1988). In addition, the large magnitudes of drag coefficients for the smallest KC-numbers, no longer show a relationship to the physical processes of the interaction between the water motions and the model. This indicates a limitation of the Morison equation.

The prediction of the force by the Morison equation is shown to be best for the regular wave condition. Adding a current to the wave field increases the chance for larger errors occur between the measured hydrodynamic forces and Morison forces for both the horizontal and vertical direction. For all tests, the maximum mean magnitude error for the horizontal hydrodynamic force prediction is 12% and for the vertical hydrodynamic force prediction 15%. In general, the error is an under prediction of the force. Regarding the prediction of the shape of the force signals, phase shifts between the peaks are found. In addition, for regular waves a 'shoulder' is found in the measured signal, which is not accounted for by the Morison force signal. To conclude, the prediction by the Morison equation is fairly good. However, for design purposes, errors of a magnitude of 12% and 15% are too large. Therefore, measure have to be taken before the Morison equation can be used for the prediction of the Hydrodynamic forces.

1. What is the relationship found between environmental parameters and the hydrodynamics forces on a fixed small scale tunnel element and how well can these forces be predicted?

The relationship between the environmental parameters are described well by the velocities and accelerations of the water. The range of waves used in the present study result in a inertia dominated environment. Only as the magnitude of the added current velocity increases, the significance of the drag is shown. Larger vertical hydrodynamic forces are found than horizontal hydrodynamic forces. Using the Morison equation to predict the forces, results in a general under prediction of the hydrodynamic forces. Therefore, for design purposes additional measures will have to be taken to reduce the prediction error.

2. What are the kinematic model response and the force tether response of a tethered rectangular cylinder subjected to a regular wave environment in small scale flume experiments? And what is the influence of the structure submergence depth and tether angles on these responses?

The shape of the relationship between the wave parameters and the model kinematics is in general described by the same shape as was found in the relationship between the wave parameters and the hydrodynamic forces in the fixed model tests. Deviations from these trends are found when non-static features occur, such as snap forces and wave frequencies approaching the eigen frequency of a system.

The influence of the submergence depth on the magnitudes of the kinematics was studied and a larger submergence depth was found to result in smaller magnitudes of the kinematics. The influence of the tether angle was that a larger tether angles gives larger kinematic magnitudes.

Overall, the configuration with the deepest model submergence depth and the smallest tether angle, leads to the smallest displacements and accelerations, making it most preferable for real practise constructions.

The study on the kinematics has demonstrated that many different features can influence the behaviour of a tethered model. Features that were found to be of influence are: higher order wave frequency dependency, slack, snap forces, resonance frequency and wave breaking. To improve the prediction of the forces to expect in the tethers and to better understand the system in general, full structural dynamic analysis are needed that include the forces due to motions.

Recommendations

For future studies on the topic of this study it is recommended to apply several changes to the set-up, parameter scope and the data processing. This study is one of the few studies in which a combined wave-current environment is created by creating a current in a wave flume and adding a wave field with a wave generator. The methodology for computing the water particle velocities in this study has showed to be relatively good for the horizontal water particle velocity, but shows room for improvement for the vertical water particle velocities. In the present study the interaction between the added current and the wave parameters has only been analysed briefly. Studying a larger data set and trying different computations for the velocity, can give more insights on the interaction.

In general, the use of more data is recommended. Especially for the part where the force coefficients are determined and analysed, scatter is expected. With scattered data more data is desirable to be better able to see trends and draw conclusions.

As mentioned in the discussion the current inflow can be improved. In the experiments of the present study no measures were taken to smoothen the inflow of the current into the flume. As a result turbulence and other disturbances of increasing magnitudes were found for an increasing current. The smoothening of the current inflow can affect the influence of the current on the waves, and can therefore be of significance.

Furthermore, it is recommended to look for better ways for computing a velocity representative to the velocity at the model. This can improve the inaccuracies in the phase shift of the force and velocity signal resulting in the negative drag coefficients. Also, measuring the velocity at different depth simultaneously can give more accurate velocity amplitudes and possibly give more insight on the influence of an added current to a wave field at different heights in the water column.

Regarding the tether model, the best configuration, resulting the smallest displacements and accelerations was the configuration for a 30° tether angle and a the largest model submergence depth. For this configurations the kinematics were smallest for the horizontal direction. To further improve this configuration, measures can be taken to try and reduce the vertical motions. A possible solution could be to add vertical 90° tethers. An example is schematized in Figure 79.

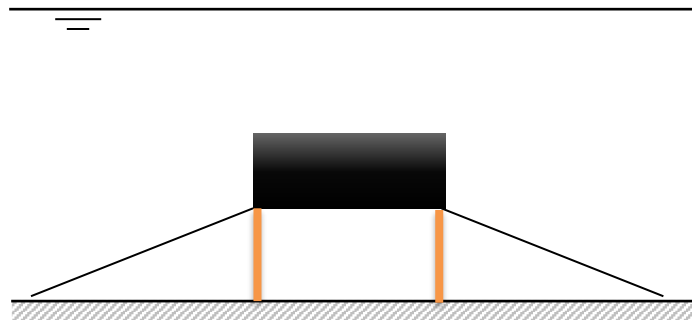


Figure 79: Concept drawing of 90° tethers (orange) to the 30° tether angle configuration.

Bibliography

- Arai, S. (1993). Forces and circulation of horizontal cylinders submerged in regular waves. *Proceedings of the Third International Offshore and Polar Engineering Conference vol. m*, 288-293.
- Arai, S. (1995). forces on and flows around a horizontal rectangular cylinder submerged in regular waves. *Proceedings of the Fifth Interntional Offshore and Polar engineering Conference vol. 3*, 348-355.
- Bearman, P., & Trueman, D. (1972). An Investigation of the flow around rectangular cylinders. *the Aeronautical Quarterly*, 229-237.
- Breuer, M. (2000). Accurate computations of the laminar flow past a square cylinder based on two different methods: lattice-Boltzmann and finite-volume. *Heat and Fluid Flow*, 186-196.
- Chaplin, J. R. (1985). Loading on a cylinder in uniform oscillatory flow. *Appl. Ocean Res.*, 188-196.
- Chaplin, J., & Subbiah, K. (1997). Large Scale horizontl cylinder forces in waves and currents. *Applied Ocean Research 19*, 211-223.
- Courchesne, J., & Laneville, A. (1979). A comparison of correction methods used in the evaluation of drag coeficient measurements of two-dimensional rectangular cylinders. *Journal of Fluids engineering 101*, 506-510.
- Fredsøe, J., & Sumer, M. (2006). *Hydrodynamics Around Cylindrical Structures*.
- Holthuijsen, L. H. (2007). *Waves in Oceanic and Coastal Waters*. Cambridge.
- Hudspeth, R. (1988). Wave/Phase Amplitude Effects on Force Coefficients. *Ocean Engineering*, 34-49.
- Ikeda, Y., Otsuka, K., & Tanaka, N. (1988b). Viscous forces acting on a semi sumersible. *The Seventh International Conference on Offshore Mechanics and Arctic Engineering*, 7-12.
- Mehaute, L. (1976). *An introduction to hydrodynamics and Water Waves*.
- Michelis, T. (2017). *Boundary Layer Sparation: Diagnostics and Control*.
- Morison, J., Johnson, J., & Schaaf, S. (1950). The Force Exerted by Surface Waves on Piles. *Journal of Petroleum Technology*.
- Nakaguchi, H. (1968). an experimental study on aerodynamic drag of rectangular cylinders. *Journal of the Japan society for Aero and Space Sciences*, 1-5.
- Robinson, A. (2015). The effet of inlet design on the flow within a combined waves and current flumes, test tank and basins. *Coastal Engineering 95*, 117-129.
- Sarpyaka, T. (1985). In-line force on a cylinder translating in oscillatory flow. *Applied Ocean Research Vol.7*.
- Venugopal, V. (2006). Wave Force Coefficients for Horizontlly submerged rectangular cylinders. *Ocean Engineering*.
- Venugopal, V. (2008). Drag and Inertia Coefficients for Horizontally Submerged Rectangular Cylinders in Waves and Currents.

Appendices

A. List of All Experiments Done

All wave in the table underneath are all wave height and wave periods: R12, R13, R14, R21, R22, R23, R24, R31, R32, R33, R34, R41, R42, R43, R44

Fixed Model

	d_s	Regular Waves	Waves + 0,1 m/s	Waves + 0,2 m/s	Waves + 0,3 m/s	Waves + 0,4 m/s
Old Model	-0.080					
	0.000					
	0.175					
	0.350					

	d_s	Repeat Regular Waves	Waves + 0,1 m/s	Waves + 0,2 m/s	Waves + 0,3 m/s	Waves + 0,4 m/s
Model no. 1	-0.080					
	0.000					
	0.175					
	0.350					

BWR 1.7

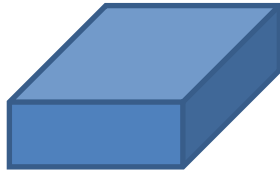
	Angle	d_s	Regular Waves	Waves + 0,1 m/s	Waves + 0,2 m/s	Waves + 0,3 m/s	Waves + 0,4 m/s
I	30	0.000					
II	30	0.175					
III	30	0.350					
IV	70	0					

BWR 1.5

	Angle	d_s	Regular Waves	Waves + 0,1 m/s	Waves + 0,2 m/s	Waves + 0,3 m/s	Waves + 0,4 m/s
I	30	0.000					
II	30	0.175					
III	30	0.350					
IV	70	0.000					
V	70	0.175					
VI	70	0.350					

B. Model Weight Distributions

BWR1.7



Model
15.34 kg
 $h_{\text{centre}}=0.08$ m



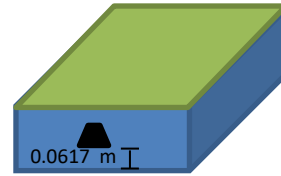
Lit/cover
4.9488 kg
 $h_{\text{centre}}=0$ m



Lead bar
8.632 kg
 $h_{\text{centre}}=0.0183$ m

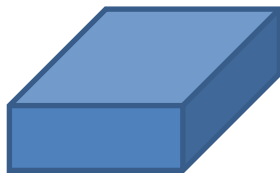


Foam + small wood + screws
1.0892 kg
 $h_{\text{centre}}=0.08$ m



Total:
30.01 kg
BWR=1.69
 $h_{\text{centre}}=0.08$ m

BWR1.5



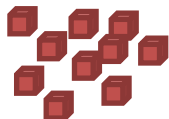
Model
15.34 kg
 $h_{\text{centre}}=0.08$ m



Lit/cover
4.9488 kg
 $h_{\text{centre}}=0$ m



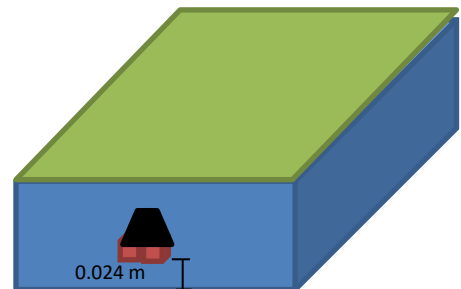
Lead bar
8.632 kg
 $h_{\text{centre}}=0.0183$ m



10x cubes
3.786 kg
 $h_{\text{centre}}=2.6$ m
 $h=5.2$ cm



Foam + small wood + screws
1.0892 kg
 $h_{\text{centre}}=0.08$ m



Total:
33.7378 kg
BWR=1.50
 $h_{\text{centre}}=0.08$ m

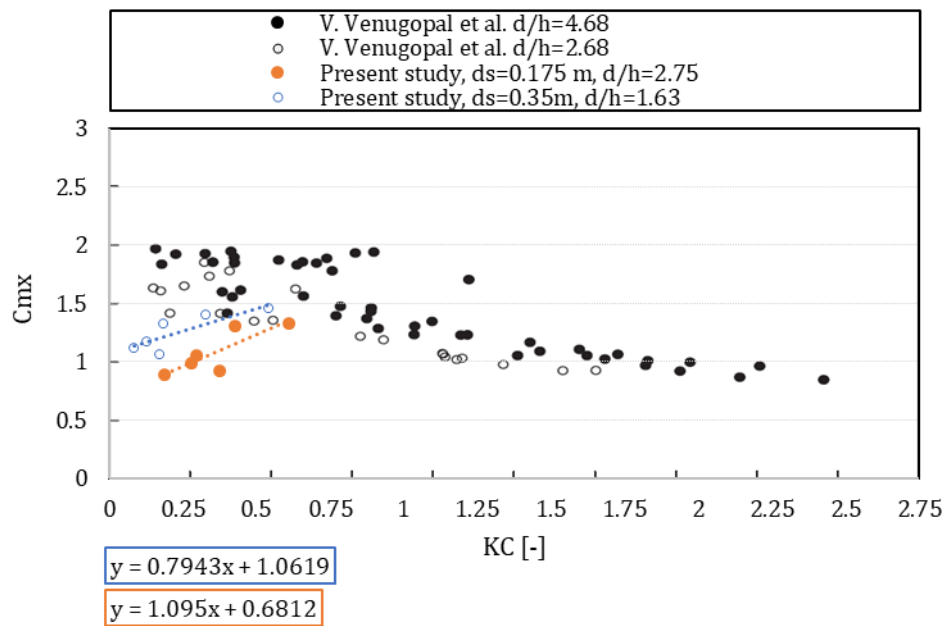
C. Prediction Coefficients for the Morison Equation

$C_{M,x}$

For the force prediction of *regular waves*, the applied $C_{M,x}$ coefficients come from the trendlines found in this study, per submergence depth:

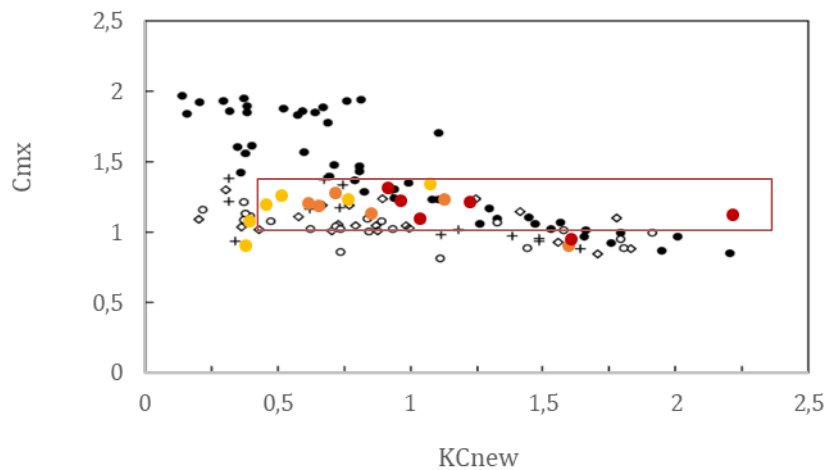
$$D_s = 0.175 \text{ m: } C_{M,x} = 0.7943 \cdot KC + 1.0619$$

$$D_s = 0.35 \text{ m: } C_{M,x} = 1.095 \cdot KC + 0.6812$$



For the ones including current, using a mean value (of the ones in orange box) would do well:

$$\text{Tests with current: } C_{M,x} = 1.21$$

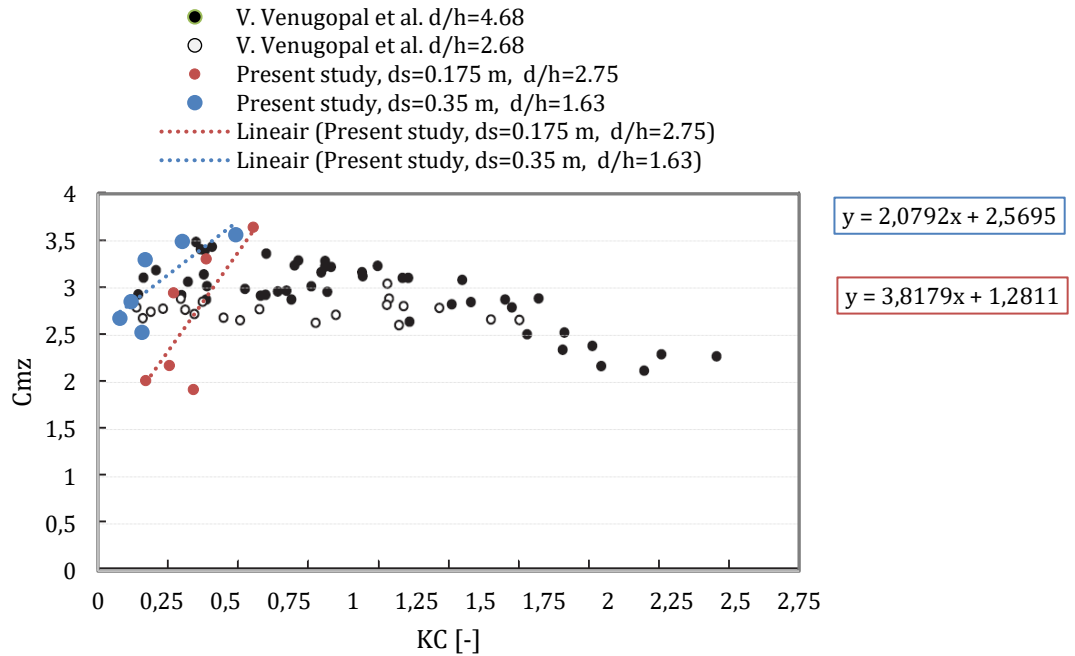


$C_{M,z}$

For the vertical inertia coefficients:

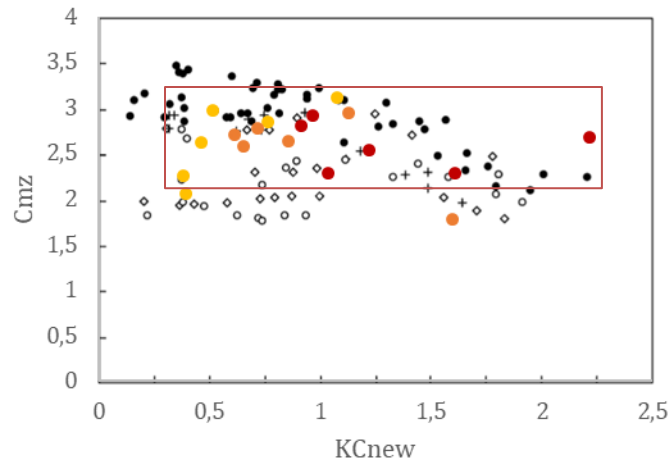
$$D_s = 0.175 \text{ m: } C_{m,z} = 3.8179 * KC + 1.2811$$

$$D_s = 0.35 \text{ m: } C_{m,z} = 2.079 * KC + 2.5695$$



For the ones including a current the mean of the ones in the box are used:

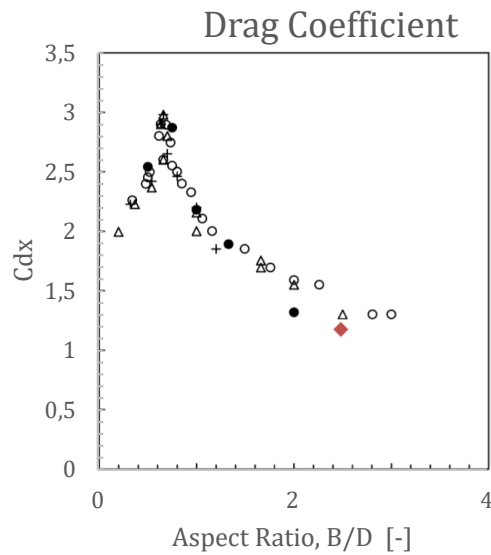
$$C_{m,z} = 2.68$$



C_{dx} and C_{dz}

For C_{dx} the drag found for current only is used, from the graph with an aspect ratio of 2.5. For regular waves and wave with a small current, this results in a smaller value than was found in the study. However, for small KC —numbers this has little effect on the prediction of the force magnitude, since the inertia is dominant.

$$C_{d,x} = 1.18$$



From the same graph the C_{dz} is chosen for an aspect ratio of 0.4:

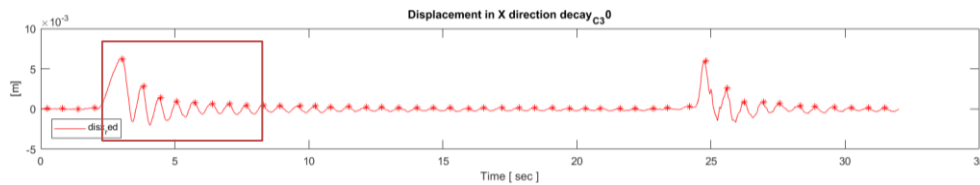
$$C_{d,z} = 2.30$$

D. Dynamic parameters

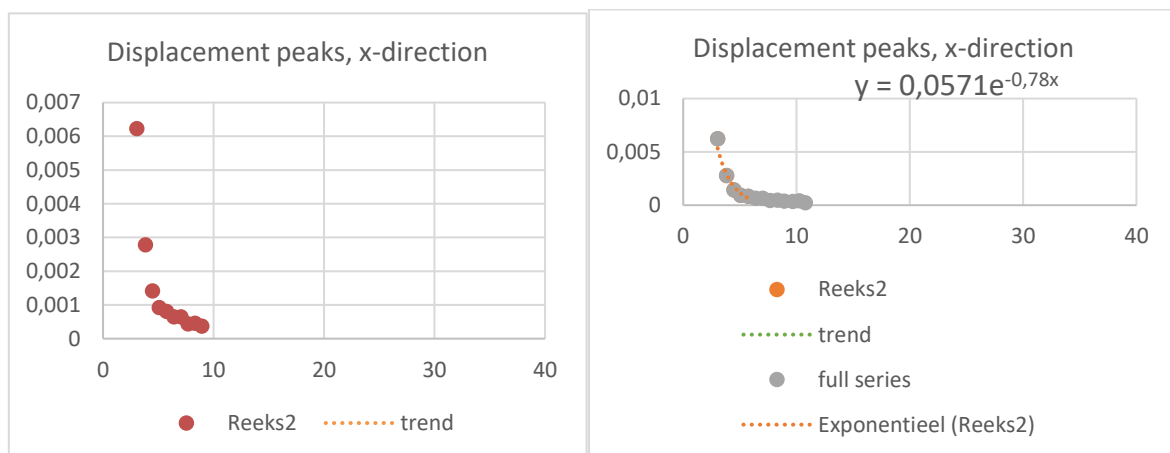
This appendix explains how the dynamic parameters like damping and natural period were found. For this 2 methods are used a manual method and a CWT method:

Method 1

The decay test below shows a decay test for the red tracker The red stars, depict the peaks.



In excel the peaks selected and put in a graph. Only the first part of the decay part is used.



Lecture notes from CIE4140- Structural dynamics (Lecture 3) give the following description of the exponential decay line:

$$A_0 \exp(-\zeta \omega_n t)$$

In the example above for C_30, $A_0 = 0.0571$ and the $\zeta \omega_n$ -term is $=0.78$.

Next the following method is used:

$$n\delta = \ln\left(\frac{X_i}{X_{i+n}}\right)$$

Where n is the number of cycles between X_i and X_{i+n} .

Now the damping factor ζ can be determined:

$$\zeta = \frac{\delta}{\sqrt{(2\pi)^2 + \delta^2}}$$

With ζ known, the natural frequency can be determined:

$$\omega_n = \frac{0.67}{\zeta} \quad \text{making} \quad T_n = \frac{2\pi}{\omega_n}$$

From there the spring constant and critical damping can be determined (with m known):

$$k = \omega_n^2 m$$

$$C_{crit} = 2\sqrt{km}$$

Now, the damping coefficient can be calculated:

$$c = \zeta C_{crit}$$

For the three studied configurations the following parameters have been determined by the above described method:

	C_30	C_70	B_30
δ	0.452	0.427	0.447
ζ	0.0716	0.068	0.07095
ω_n	10.9	5.83	10.18
T_n	0.58	1.08	0.62
k	3995	1146	3493
C_{crit}	734	393	686
c	52.62	26.6	48.71

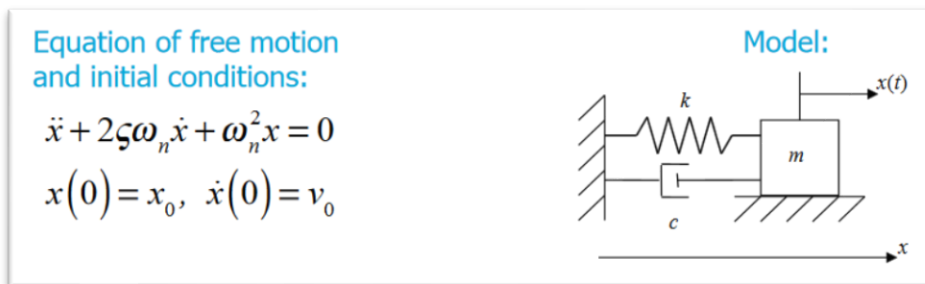
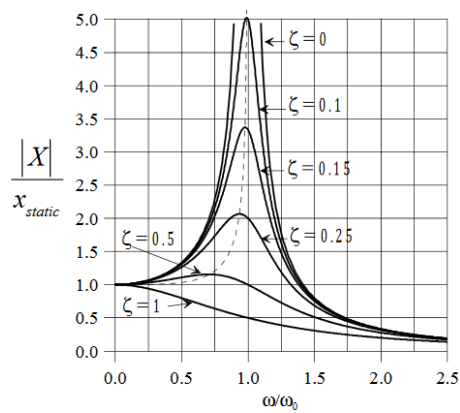


Figure: Model for 1 DoF viscous damping



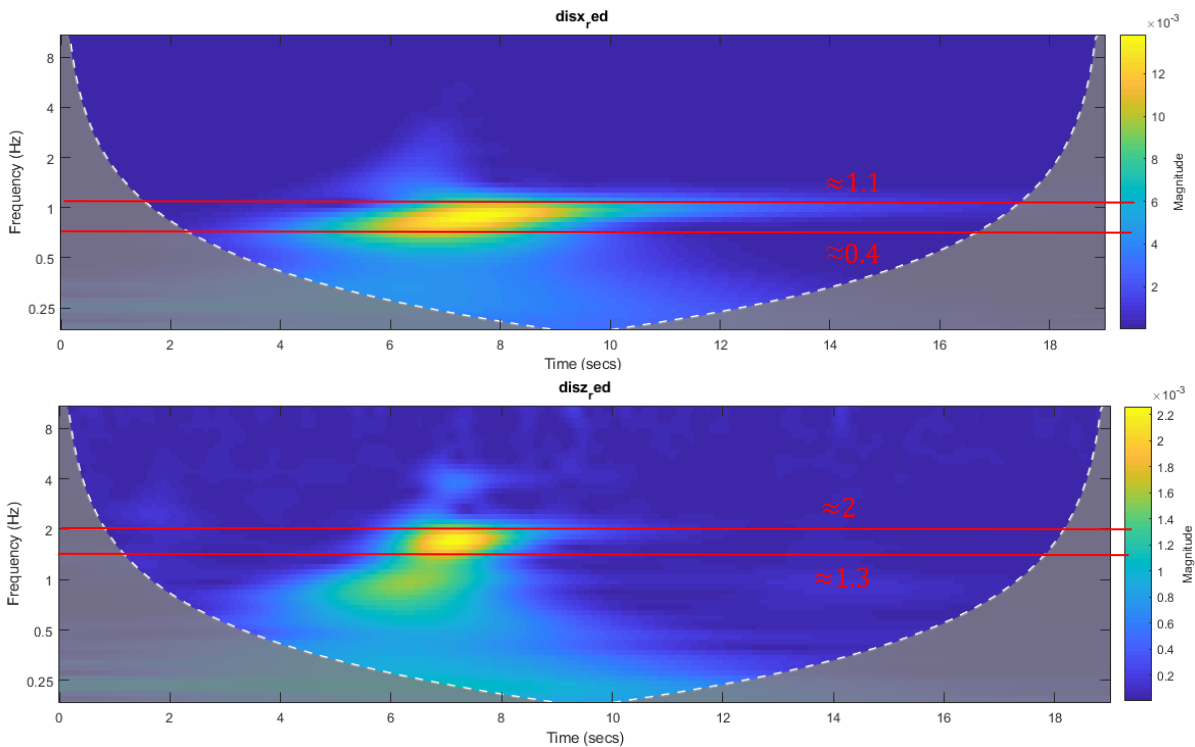
			B_30 $\alpha=30^\circ$ ds=0.175 m		C_30 $\alpha=30^\circ$ ds=0.35 m		C_70 $\alpha=70^\circ$ ds=0.175 m	
			X	Z	X	Z	X	Z
		Tn	0,62	-	0,58	0,61	1,08	0,91
T=	0,92	T/Tn	1,49	-	1,59	1,52	0,85	1,01
T=	1,13	T/Tn	1,83	-	1,96	1,87	1,05	1,24
T=	1,41	T/Tn	2,28	-	2,44	2,33	1,31	1,54
T=	1,84	T/Tn	2,98	-	3,19	3,04	1,71	2,01

Method 2:

The second method is with the use of CWT graphs. Studying CWT graphs from the decay displacement motions, the model eigen frequency, thus the eigen period, can be distinguished. Only for the configuration with the 70 degrees angle frequencies were found in the range of the wave frequencies of the present study, see the CWTs on this page.

X-direction: $F_{\text{eigen}} \approx 0.4-1.1$ Hz $T_{\text{eigen}} \approx 0.91-2.5$ s in range of wave periods

Z-direction: $F_{\text{eigen}} \approx 1.3-2$ Hz $T_{\text{eigen}} \approx 0.5-0.77$ s close to range of wave periods

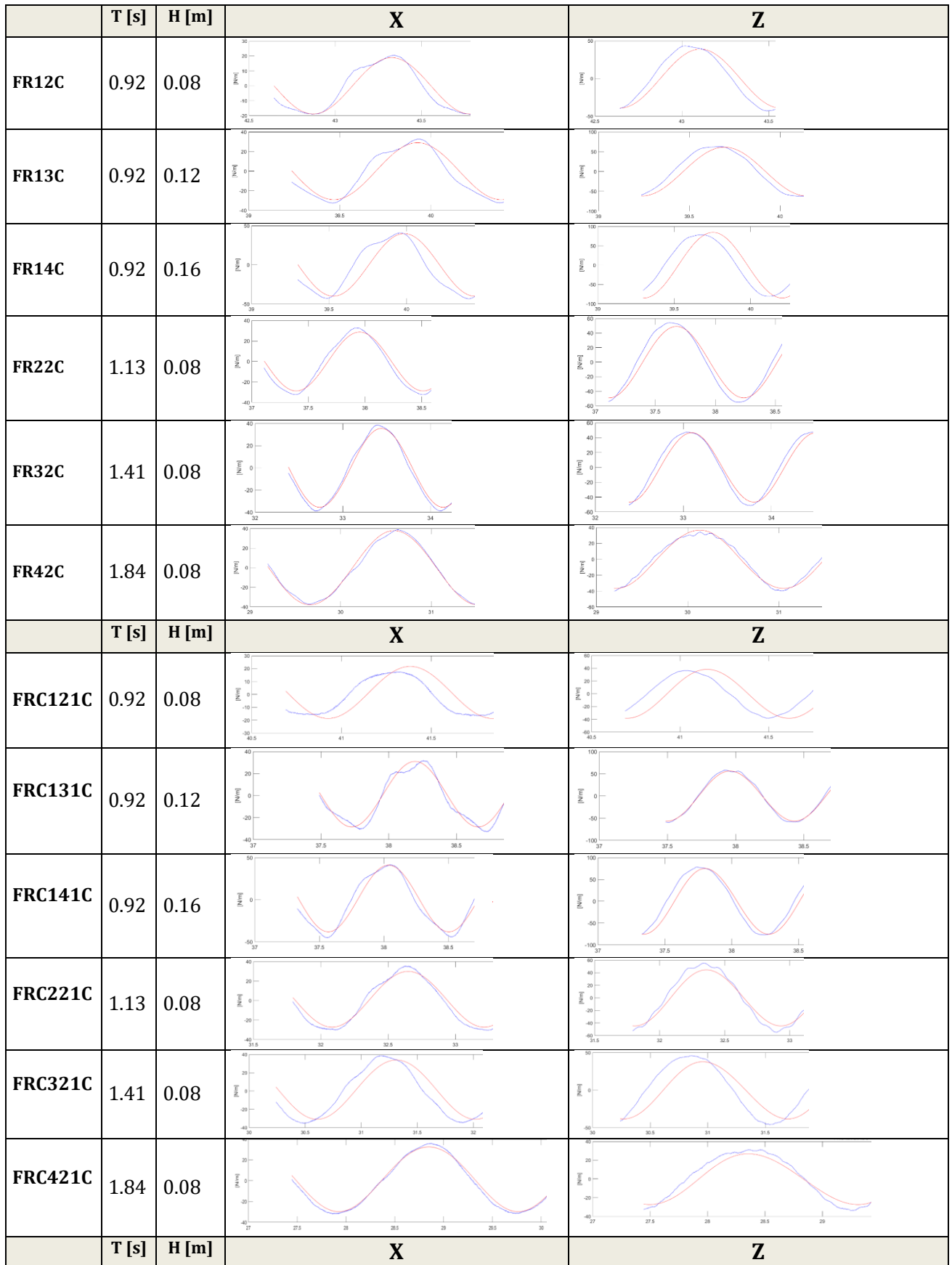


Conclusions:

The influence both methods, indicate that the wave periods of the present study are expect only to come close to the natural frequency of the configuration with the 70 degrees angle. This is confirmed by both methods mainly for the displacement in the horizontal direction. However, there is also a change for the smaller wave periods in the vertical displacement, that they come close to the natural frequency.

E. Fixed Model Force Signals

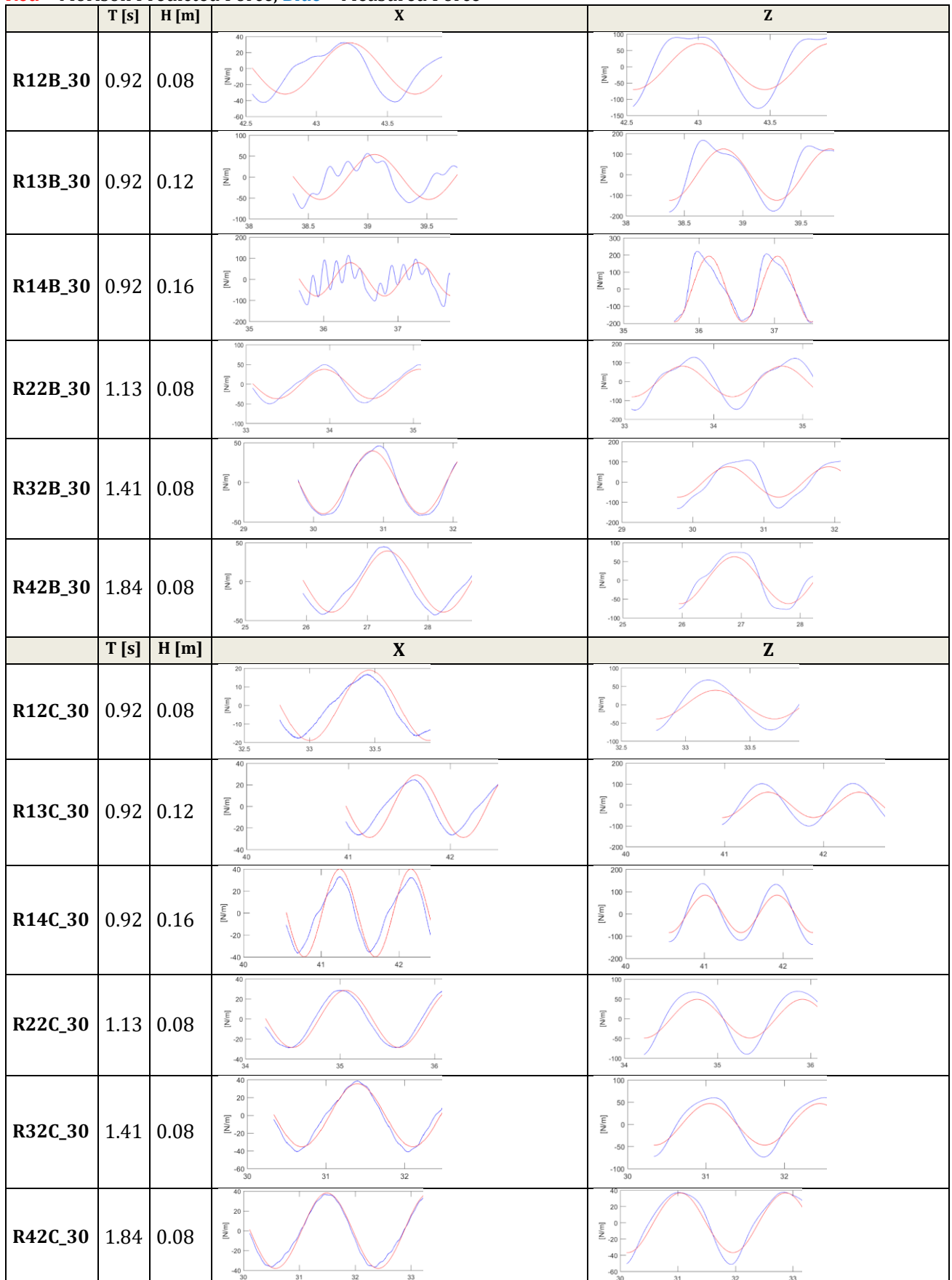
Red= Morison Predicted Force, Blue= Measured Force



FRC122C	0.92	0.08		
FRC132C	0.92	0.12		
FRC142C	0.92	0.16		
FRC222C	1.13	0.08		
FRC322C	1.41	0.08		
FRC422C	1.84	0.08		
	T [s]	H [m]	X	Z
FRC123C	0.92	0.08		
FRC133C	0.92	0.12		
FRC143C	0.92	0.16		
FRC223C	1.13	0.08		
FRC323C	1.41	0.08		
FRC423C	1.84	0.08		

F. Tether Model Force Signals

Red= Morison Predicted Force, Blue= Measured Force



	T [s]	H [m]	X	Z
R12C_70	0.92	0.08		
R13C_70	0.92	0.12		
R14C_70	0.92	0.16		
R22C_70	1.13	0.08		
R32C_70	1.41	0.08		
R42C_70	1.84	0.08		

G. Frequency Bands

Horizontal Displacement

Test ID	Multi. Sign. bands	Wave freq dominant	Other freq dominant	Comments
R12B_30M	X	X		
R13B_30M	X	X	X	
R14B_30M	X		X	
R22B_30M	X		X	
R32B_30M	X	X	X	
R42B_30M	X		X	
R12C_30M		X		
R13C_30M		X		
R14C_30M	X	X		
R22C_30M	X	X		
R32C_30M	X	X	X	
R42C_30M	X	X	X	A Third one develops
R12C_70M		X		
R13C_70M		X		
R14C_70M		X		
R22C_70M		X		
R32C_70M		X		
R42C_70M	X	X		

Vertical Displacement

Test ID	Sign. Multi. bands	Wave freq dominant	Other freq dominant	Comments
R12B_30M	X	X		
R13B_30M	X	X		
R14B_30M	X	X		
R22B_30M	X	X		
R32B_30M	X	X		
R42B_30M	X	X		
R12C_30M		X		
R13C_30M		X		
R14C_30M		X		
R22C_30M	X	X		
R32C_30M	X	X		
R42C_30M	X	X		
R12C_70M		X		
R13C_70M		X		
R14C_70M		X		
R22C_70M		X		
R32C_70M		X		
R42C_70M	X	X		

Horizontal Acceleration

Horizontal Acceleration (Video)

Test ID	Multi. Sign. bands	Wave freq dominant	Other freq dominant	Comments	Test ID	Sign. Multi. bands	Wave freq dominant	Other freq dominant	Comments
R12B_30M	X	X			R12B_30M	X			Noise, vague bands
R13B_30M	X	X			R13B_30M	X			Noise, vague bands
R14B_30M	X		X	dominant at peaks	R14B_30M	X		X	Noise, vague bands
R22B_30M	X	X	X		R22B_30M				Noise, vague bands
R32B_30M	X		X		R32B_30M	X		X	Noise, vague bands
R42B_30M	X		X		R42B_30M	X		X	Noise, vague bands
R12C_30M	X	X		other bands vaguely	R12C_30M	X			Noise, vague bands
R13C_30M	X	X		other bands vaguely	R13C_30M		X		Noise, vague bands
R14C_30M	X	X			R14C_30M				Noise, vague bands
R22C_30M	X		X		R22C_30M				Noise, vague bands
R32C_30M	X		X		R32C_30M				Noise, vague bands
R42C_30M	X	X	X		R42C_30M				Noise, vague bands
R12C_70M	X	X			R12C_70M	X	X		Wave very dom.
R13C_70M	X		X		R13C_70M	X	X		Wave very dom.
R14C_70M	X		X		R14C_70M	X	X		Wave very dom.
R22C_70M	X		X	peaky noise is dom.	R22C_70M	X	X		Wave very dom.
R32C_70M	X	X		Still sign. Peaky noise	R32C_70M	X	X		
R42C_70M	X	X		Noise almost gone	R42C_70M	X		X	

Vertical Acceleration

Vertical Acceleration (Video)

Test ID	Vertical Acceleration			Comments	Vertical Acceleration (Video)			Comments
	Multi. Sign. bands	Wave freq dominant	Other freq dominant		Sign. Multi. bands	Wave freq dominant	Other freq dominant	
R12B_30M	X	X		diff AC1 AC2	X	X		
R13B_30M	X	X	X	complete diff AC1 AC2	X	X		Further in signal, other freq dom.
R14B_30M	X	X	X	complete diff AC1 AC2	X	X	X	
R22B_30M	X	X	X	complete diff AC1 AC2	X	X		vague bands
R32B_30M	X		X		X			Vague bands equal
R42B_30M	X		X		X			even more vague bands
<hr/>								
R12C_30M		X				X		yellow high order noise stains
R13C_30M	X	X				X		yellow high order noise stains
R14C_30M	X	X				X		More dominant
R22C_30M	X	X	X	increase in sign.	X	X	X	
R32C_30M	X		X		X			very vague bands, high order noise
R42C_30M	X		X		X			very vague bands, high order noise
<hr/>								
R12C_70M	X		X				X	
R13C_70M	X		X				X	
R14C_70M	X		X		X		X	
R22C_70M	X		X		X		X	
R32C_70M	X		X				X	
R42C_70M	X		X		X			very vague bands

Horizontal Resultant Tether Force

Vertical Resultant Tether Force

Test ID	Horizontal Resultant Tether Force			Comments	Vertical Resultant Tether Force			Comments
	Multi. Sign. bands	Wave freq dominant	Other freq dominant		Sign. Multi. bands	Wave freq dominant	Other freq dominant	
R12B_30M	X	X			X	X		
R13B_30M	X	X			X	X		
R14B_30M	X	X	X	peaky higer freq increases in magnitude	X	X		
R22B_30M	X	X		Wave freq very dom.	X	X		
R32B_30M		X			X	X		
R42B_30M		X			X	X		
R12C_30M	X	X		Wave freq very dom		X		
R13C_30M	X	X		Wave freq very dom		X		
R14C_30M	X	X		Wave freq very dom		X		
R22C_30M		X		Only wave freq. Band	X	X		
R32C_30M	X	X		Wave freq very dom	X	X		
R42C_30M	X	X		Wave freq very dom	X	X		
R12C_70M	X	X			X		X	Wave freq. Also sign.
R13C_70M	X	X			X		X	Wave freq. Also sign.
R14C_70M	X	X	X	higher order peaky dom.	X		X	Wave freq. Also sign.
R22C_70M	X	X	X	higher order peaky dom.	X		X	Larger T, more wave dom.
R32C_70M	X	X			X		X	Larger T, more wave dom.
R42C_70M	X	X		very dom. wave.	X	X		Larger T, more wave dom.

H. Results from fixed model tests

Regular Waves:

Test ID	Input Parameters				T, h4		U _{m,x} , EMS, lin wave		C _{m,x}		U _{m,z} , EMS, lin wave		C _{m,z}	
	T, input [s]	H, input [m]	U _c , input [m/s]	d _s [m]	T, h4 [s]	H, h4 [m]	U _{m,x} , EMS, lin wave [m/s]	F _x [N/m]	C _{m,x} [-]	C _{d,x} [-]	U _{m,z} , EMS, lin wave [m/s]	F _z [N/m]	C _{m,z} [-]	C _{d,z} [-]
FR12B	0,92	0,08	0	0,18	0,93	0,08	0,11	20,6	0,89	-36,9	0,107	84,4	2,02	-32,2
FR13B	0,92	0,12	0	0,18	0,92	0,12	0,16	33,0	0,98	-8,6	0,158	119,3	2,18	-6,2
FR14B	0,92	0,16	0	0,18	0,92	0,15	0,21	42,8	0,92	-8,9	0,205	145,2	1,92	-6,2
FR22B	1,13	0,08	0	0,18	1,13	0,09	0,12	33,4	1,05	-26,6	0,119	99,7	2,95	-8,6
FR32B	1,41	0,08	0	0,18	1,41	0,08	0,13	39,7	1,30	7,2	0,102	92,4	3,30	17,4
FR42B	1,84	0,08	0	0,18	1,84	0,08	0,14	39,3	1,33	-8,4	0,084	65,8	3,64	-10,8
FR12C	0,92	0,08	0	0,35	0,93	0,08	0,11	20,6	1,11	-66,8	0,107	43,4	2,68	-89,7
FR13C	0,92	0,12	0	0,35	0,92	0,12	0,16	33,0	1,17	-29,6	0,157	63,1	2,85	-32,6
FR14C	0,92	0,16	0	0,35	0,92	0,15	0,21	42,8	1,06	-40,7	0,209	81,3	2,53	-42,3
FR22C	1,13	0,08	0	0,35	1,13	0,09	0,12	33,4	1,33	-9,8	0,114	54,7	3,30	-16,3
FR32C	1,41	0,08	0	0,35	1,41	0,08	0,13	39,7	1,40	4,4	0,107	48,2	3,49	-0,3
FR42C	1,84	0,08	0	0,35	1,84	0,08	0,14	39,3	1,45	2,4	0,082	34,1	3,57	1,9

Combined Wave-Current:

Test ID	Input Parameters				Wave Parameters				Wave Current Parameters		Wave Parameters		Wave Current Parameters	
	T, input [s]	H, input [m]	Uc, input [m/s]	d _s [m]	T,h4 [s]	H,h4 [m]	Um,x, EMS, lin wave [m/s]	Fx [N/m]	Cm,x [-]	Cd,x [-]	Um,z, EMS, lin wave [m/s]	Fz [N/m]	Cm,z [-]	Cd,z [-]
FRC121C	0,92	0,08	0,1	0,35	0,94	0,07	0,11	28,6	0,91	-2,1	0,105	53,0	2,26	-33,7
FRC131C	0,92	0,12	0,1	0,35	0,95	0,10	0,16	38,8	1,08	-3,5	0,157	62,6	2,06	-34,9
FRC141C	0,92	0,16	0,1	0,35	0,95	0,12	0,21	44,0	1,19	-3,1	0,209	81,7	2,62	-17,9
FRC221C	1,13	0,08	0,1	0,35	1,13	0,08	0,12	36,2	1,26	-2,4	0,113	55,7	2,97	-17,3
FRC321C	1,41	0,08	0,1	0,35	1,42	0,08	0,13	38,9	1,23	-2,4	0,107	46,5	2,84	-15,0
FRC421C	1,84	0,08	0,1	0,35	1,85	0,08	0,14	40,8	1,34	-0,3	0,090	33,2	3,11	-2,1
FRC122C	0,92	0,08	0,2	0,35	0,95	0,07	0,11	31,5	1,21	0,9	0,105	46,4	2,70	-15,5
FRC132C	0,92	0,12	0,2	0,35	0,95	0,09	0,16	43,2	1,19	0,4	0,157	68,1	2,58	-16,2
FRC142C	0,92	0,16	0,2	0,35	0,95	0,12	0,21	54,7	1,27	0,8	0,209	83,1	2,78	-3,4
FRC222C	1,13	0,08	0,2	0,35	1,14	0,07	0,12	42,5	1,13	0,5	0,113	53,2	2,62	-11,1
FRC322C	1,41	0,08	0,2	0,35	0,00	0,00	0,13	43,0	1,23	0,7	0,107	40,7	2,94	-4,0
FRC422C	1,84	0,08	0,2	0,35	1,84	0,07	0,14	41,8	0,90	2,3	0,090	27,9	1,78	9,5
FRC123C	0,92	0,08	0,3	0,35	0,93	0,06	0,11	39,7	1,31	1,4	0,105	44,4	2,80	4,2
FRC133C	0,92	0,12	0,3	0,35	0,96	0,07	0,16	57,1	1,22	1,1	0,157	71,2	2,91	-4,8
FRC143C	0,92	0,16	0,3	0,35	0,97	0,09	0,21	56,8	1,09	1,0	0,209	68,2	2,28	-5,2
FRC223C	1,13	0,08	0,3	0,35	1,11	0,07	0,12	48,8	1,22	1,1	0,113	47,6	2,53	1,1
FRC323C	1,41	0,08	0,3	0,35	1,46	0,07	0,13	48,6	0,95	0,9	0,107	41,2	2,27	-2,8
FRC423C	1,84	0,08	0,3	0,35	1,80	0,07	0,14	48,0	1,12	1,1	0,090	27,2	2,67	-0,7

I. Results Tether Model in Regular Waves

Test ID	T, input [s]	H, input [m]	Tether Angle [°]	d_s [m]	Um,x, EMS, lin wave [m/s]	AC1X [m/s ²]	displ. Amp Red [m]	Um,z, EMS, lin wave [m/s]	AC1z [m/s ²]	displ. Amp Red [m]	LC1', max [N]	LC2', max [N]	LC3', max [N]	LC4', max [N]
R12C_70M	0,92	0,08	70	0,35	0,106	0,4	0,016	0,105	0,5	0,003	26,4	27,0	31,1	32,7
R13C_70M	0,92	0,12	70	0,35	0,160	0,5	0,019	0,157	0,7	0,005	39,4	40,1	46,6	49,3
R14C_70M	0,92	0,16	70	0,35	0,213	1,1	0,021	0,209	1,4	0,006	72,4	73,9	87,2	90,0
R22C_70M	1,13	0,08	70	0,35	0,123	1,3	0,030	0,113	1,6	0,011	67,9	69,0	87,5	88,6
R32C_70M	1,41	0,08	70	0,35	0,133	0,5	0,031	0,107	0,6	0,008	41,0	41,9	35,5	36,5
R42C_70M	1,84	0,08	70	0,35	0,140	0,3	0,022	0,090	0,2	0,004	15,7	16,3	16,7	16,9

Test ID	T, input [s]	H, input [m]	Tether Angle [°]	d_s [m]	Um,x, EMS, lin wave [m/s]	AC1X [m/s ²]	displ. Amp Red [m]	Um,z, EMS, lin wave [m/s]	AC1z [m/s ²]	displ. Amp Red [m]	LC1', max [N]	LC2', max [N]	LC3', max [N]	LC4', max [N]
R12C_30M	0,92	0,08	30	0,35	0,106	0,2	1,7E-04	0,105	0,2	1,8E-03	29,7	28,7	28,9	28,8
R13C_30M	0,92	0,12	30	0,35	0,160	0,3	3,7E-04	0,157	0,3	2,5E-03	42,6	42,4	42,4	41,0
R14C_30M	0,92	0,16	30	0,35	0,213	0,4	4,7E-04	0,209	0,4	3,5E-03	55,8	54,5	55,2	54,9
R22C_30M	1,13	0,08	30	0,35	0,123	0,2	3,8E-04	0,113	0,1	2,6E-03	29,2	28,3	29,4	28,9
R32C_30M	1,41	0,08	30	0,35	0,133	0,2	6,6E-04	0,107	0,2	2,2E-03	27,6	27,0	22,8	22,5
R42C_30M	1,84	0,08	30	0,35	0,140	0,2	4,7E-04	0,090	0,1	1,6E-03	18,7	18,0	17,2	17,0

Test ID	T, input [s]	H, input [m]	Tether Angle [°]	d_s [m]	Um,x, EMS, lin wave [m/s]	AC1X [m/s ²]	displ. Amp Red [m]	Um,z, EMS, lin wave [m/s]	AC1z [m/s ²]	displ. Amp Red [m]	LC1', max [N]	LC2', max [N]	LC3', max [N]	LC4', max [N]
R12B_30M	0,92	0,08	30	0,175	0,106	0,8	6,4E-04	0,105	1,7	3,2E-03	43,9	44,3	36,2	37,6
R13B_30M	0,92	0,12	30	0,175	0,160	1,5	6,7E-04	0,157	1,8	6,0E-03	71,2	70,8	64,2	66,4
R14B_30M	0,92	0,16	30	0,175	0,213	2,0	2,1E-03	0,209	2,1	8,3E-03	118,9	115,1	104,1	108,5
R22B_30M	1,13	0,08	30	0,175	0,123	0,4	3,7E-04	0,113	0,5	5,1E-03	57,6	57,8	43,8	45,1
R32B_30M	1,41	0,08	30	0,175	0,133	0,6	6,5E-04	0,107	0,3	4,9E-03	51,7	51,1	37,0	36,3
R42B_30M	1,84	0,08	30	0,175	0,140	0,5	4,8E-04	0,090	0,2	2,6E-03	35,9	36,2	28,6	30,3